Correlating Microscopic Ferroelectric Properties and Macroscopic Thin Film Device Performance

Thesis by
Jennifer Lynn Ruglovsky

In Partial Fulfillment of the Requirements
for the Degree of
Doctor of Philosophy

California Institute of Technology
Pasadena, California

2007
(Defended 5 February 2007)

This thesis is dedicated to my Uncle George

Acknowledgements

As I now stand on the threshold of completing my Ph.D. dissertation, I would like to first acknowledge the support of my advisor, Harry Atwater. I would like to thank him for a project that not only interested me scientifically, but one that heavily relied on interpersonal communications and collaborations, thus allowing me to meet so many wonderful people across campus. I believe these interactions enhanced the development of my scientific skills, and most importantly, enriched my personal life.

I would like to thank my "second advisor" Kaushik Bhattacharya. I have never met someone so important who felt so genuinely sorry for being busy. Throughout the years he managed to coach me through some difficult topics and made time when it seemed impossible. Also I greatly appreciate collaborations with Guruswami Ravichandran and Sossina Haile, two key professors heading up different research areas of the Caltech Ferro MURI. I would like to mention my Cornell undergrad advisor George Malliaras who inspired me to pursue graduate studies and thank him for writing many a recommendation letter over the last several years. Finally, I'd like to acknowledge my other committee members-Kerry Vahala and Dave Goodwin-who have been exemplary in collaborations, attendance, and support.

Funding from an Army Research Office MURI award and the NSF Center for the Science and Engineering of Materials supported this work. Also I would like to acknowledge a generous fellowship from the Applied Materials.

My scientific endeavors would hardly have been as productive without the technical help of the following experts. I could not go without thanking my Atwater group "mentor," Rhett Brewer. Rhett and I were only together a few months, but I was lucky enough to be bequeathed his ultracoveted corner desk, and absorb a crash course in ferroelectricity, mostly (ironically) during his defense. Dr. Youngbae Park was a postdoc we were privileged to have join the ferro project, and he was a limitless source of new ideas, answers, and papers. Professor Jiangyu Li was a major supporter of the modeling efforts in Chapter 2 of this thesis, as he was responsible for the initial work on fiber texture and provided the Fortran code necessary to begin this new study. Dr.Henri Lezec is a true gentleman and an outstanding scientist. I would like to thank him for all of his efforts, energy and inspiration, and especially enabling all of the FIB work in Chapter 4. Carrie Ross helped with CL measurements. Ken Diest in the Atwater group deserves thanks for help with AFM/PFM and for being a master solderer. I would like to thank Dr. Alex Papavasiliou at Lawrence Livermore National Laboratory, who supported me during initial fabrication efforts. Chi Ma in the geology department has provided tremendous assistance with SEM, EDS, and EBSD techniques. I have had several interactions with Alireza Gaffari of the applied physics department, and he has been a great sounding board on several occasions. I would like to thank Deniz Armani and Sameer Walavakur for their assistance in the cleanroom. Finally, Eric Ostby of the Vahala group helped me with Xenon etching, and he deserves credit for being so darn helpful so close to the end, when all I needed was a smiling face and a cooperative spirit.

I would like to thank Eleonora Chetverikova, Irene Loera, April Neidholdt, and all the administrators in applied physics who have made my transfer from Harvard, paychecks, and daily routines more smooth and pleasant. April in particular has made our group a better place to be with her advice, friendship, and access to Harry's calendar.

A few Atwater "groupies" stand out particularly in my mind and deserve specific acknowledgement. In roughly chronological order:

Christine Richardson was the first person I met when I arrived at Harvard. Since that day, she has been a constant in my life. The cities have changed and the list of supporting actors has grown, but the bond initiated (haha) back in Shpaepey's class (hahaha) has endured. Christine is my forever friend, and I would be eternally thankful for my graduate experience even if our relationship was its only product.

Though his grandmother was BFF with my grandmother's neighbor in Pittsburgh and Luke and I lived in the same apartment complex at Cornell, it took a long lonely semester at the Cambridge House for us to realize how similar and compatible we were. Luke Sweatlock has the best sense of humor of anyone I have ever met, and that quality is only rivaled by his intellect and kindness. For Luke to think of me as his "best man" makes me feel like a winner.

Julie Biteen and Maribeth Mason were like big sisters to me. It was wonderful to have amazing role models who also enjoyed shopping trips and cheesy TV.

Back in the day, Robb Walters was the officemate no one wanted. Now he is the proverbial know-it-all in the group, and his advice is most sought after. I consider myself lucky to have been in shouting distance all these years...and shout I certainly did over his *unique* music selections.

Brendan Kayes, for years now, has been the Lennon to my McCartney. His character is literally quite opposite mine-he is adventurous, contemplative, and hip. So it seemed our friendship was destined to be a ying-yang balancing of differences. However as we grew together emotionally, I really saw that our relying on one another ("If you don't graduate then I'm never going to graduate!") guaranteed our individual successes, academically and personally. I could not have done this without you, B*.

I have shared time with Matthew Dicken from the very first day he arrived at Caltech, and we have been sidekicks ever since. Matt is responsible for all of the IBAD and PLD growth in this thesis, for which I am eternally grateful. And though his efforts in the lab are basically the reason I am writing a thesis, his friendship has meant even more. The worst part about starting my new job is not having Matt to share coffee with every morning. I wish him only the best in his final years at Caltech and I hope that he and Megan are not strangers once Joe and I are settled in DC.

I would like to thank the remaining members of the Atwater group, past and present: Julie Brewer, Rhett Brewer, Jen Dionne, Ken Diest, Tao Feng, Anna Fontcuberta i Morral, Domenico Pacifici, Melissa Griggs, Jason Holt, Ben Kaufmann, Michael Kelzenberg, Pieter Kik, Sungjee Kim, Beth Lachut, Krista Langeland, Stefan Maier, Youngbae Park, Morgan Putnam, Carrie Ross, Katsu Tanabe, Darci Taylor, Jimmy Zahler. I hope that my group meeting talks were brief and that you can all name at least one Steelers player.

My extended group, the ferro MURI, has offered me stimulating collaborations and wonderful friends. David Boyd's enthusiasm for all things trendy-whether plasmon-activated CVD or Brad Pitt's latest shoes-has always encouraged my curiosity. Ronjging Zhang is responsible for the award-winning, but inaptly named "poker" apparatus, and I wish to thank her for her professionalism and kindness. Sharlotte Bolyard became Rongjing's understudy and for a short time there were THREE women on a project in the basement of Guggenheim!! Sharlotte supported me as we continued to test my devices and planned for new apartments and married lives. Phanish Suryanarayana helped with beam calculations and did not laugh too much when I needed to be reminded about Poisson's ratio. Last but not least, what would the MURI (and really, my life) be without my dear friend Mohamed El-Naggar. Moh not only provided me with CVD films, but he also introduced me to my wonderful fiance, his roommate Joseph Klamo. Thank you Moh, for always seeing the best in me...and sorry about all the shoes lying around your apartment.

I would like to thank other friends from outside of lab (seriously?): the Ernie's SOPS lunch group, friends from Cornell, Pittsburgh, New Jersey, and D-town, and other groups who just always seemed to end up at Amigos... I have been fortunate to have had a wonderful friend, Jane Khudyakov, as my roommate for my final 2 years. Jane is an amazing woman-generous and strong-and she was always cheering for me in life, love, and science. I would also like to acknowledge the kindness of my friends Michael/Stephanie/Mowgli Wolf and Mary Laura Lind, for welcoming me into their homes when my life and heart (and car and bed and...) were in Maryland, but my experiments were stuck in Pasadena.

Most importantly, I would like to thank my family. Whenever anyone would call me with the latest on Steelers injury reports, parkway traffic, or anecdotes from Walmart, they would usually say "I hope we're not bothering you." I would now like to say, once and for all, you were all always quite the opposite of bothering me. It seems such an arduous task to thank you in this allotted space in an otherwise gigantic document, but the fact that I produced such a document-a Ph.D. thesis!-I hope speaks volumes to my upbringing, character, and spirit. In spite of the labels, lifetimes, and miles separating us, I hope that this thesis, a printed document of effort and hardships, honors you all.

My parents always stressed the importance of education and prioritized whatever I thought would be the best means to that end. Throughout my time in graduate school, they have supported me as only they could know how. My mother overcame her fear of flying just so she could visit me. My father and I were able to see Paul McCartney in concert and win big in Vegas. I was always prepared to push myself harder because I knew no matter what, you were both so, so proud. Thank you for your encouragement and love. If I was half the person my sister thought I was-intelligent, fashionable, wise, savvy, responsible, and determined-I would probably be the most famous person in the world. Seeing myself through her eyes reminds me how far she has come in her life and how inspiring her outlook can be.

One of my fondest memories of my Uncle George has to be the literal distance he traveled to procure roses for my Masters graduation ceremony, when the limits of his physical heart paled in comparison to his boundless love and pride. My Aunt Barbara, my godmother, has nurtured my needs through phone calls, prayers, spending money, and jokes. Knowing that her generosity is motivated by how much she feels I deserve reminds me of what family is all about. My cousin David, the original materials scientist in the family, has shown me what it means to work hard and responsibly, knowing what and who really matters most. My Uncle Buddy's life alluded to the strength necessary being far from home but reminded me that as a family, we are always close in each other's thoughts and hearts. Finally, as the first granddaughter to both grandparents Brennan and Ruglovsky, I hope that my success will pay tribute to their hopes and dreams initiated the day I entered the world.

Finally, my life would truly not be what it is today had I never met the man of my dreams, Joseph Klamo. Just as this moment in my life honors the family I began in, it also commemorates our new beginning as a family. Thank you for your patience, love, and support during this entire process. I look forward to the rest of my life with you, knowing that our Saturdays and Sundays each and every fall are already planned. "You lift up my spirits, you shine on my soul... Whenever I'm empty, you make me feel whole. I can rely on you, to guide me through, any situation... You give me direction, you show me the way, You give me a reason, to face every day. I can depend on you, to send me to, any destination... You hold up a sign that reads, follow me, follow me."

So here I go...

Abstract

The relationship between thin film device performance and crystallographic microstructure is one of fundamental importance in materials science. Ferroelectric materials that show an electromechanical response via domain switching, such as the perovskites $BaTiO_3$ and $PbTiO_3$, are discussed. In this work, we focus on thin film MEMS actuators fabricated from four different ferroelectric thin film microstructures: poorly oriented, fiber textured, biaxially textured, and single crystal. The microscale properties of these thin film materials are characterized and correlated to macroscale mechanical device behavior.

We have modeled each of these four microstructures to determine the effect of grain-scale crystallographic texture on device-scale electromechanical constants. The method enables the effective electromechanical properties to be obtained for a polycrystalline film via a self-consistent approach. The essence of the model is to use the electromechanical field for a single grain embedded in a matrix-with yet-to-be determined uniform effective moduli-to simulate the electromechanical field in a grain at a particular orientation in the film. The total effective properties are found via numerical iteration over all grain orientations. Using this model, we show that most electromechanical constants depend primarily on the out-of-plane texture of the ferroelectric thin film.

We have used surface micromachining to create free-standing bridge geometries in ferroelectric thin films of polycrystalline and biaxially textured $PbTiO_3$. The material properties of these thin films are characterized with various techniques to confirm the texture at the grain scale. We have utilized a custom experimental apparatus that can apply a loading force to a single microdevice via magnetostatic interaction while measuring the resulting displacement. The force-displacement curves that we measure provide insight into the initial stress and modulus of our composite beam devices and the role of the underlying crystalline microstructure.

In order to study cantilever actuators, $BaTiO_3$ active layers are grown monolithically on

$SrRuO_3$ electrodes and devices are patterned via focused ion beam (FIB) milling exclusively or with a subsequent XeF_2 etch. Using this fabrication method, we study cantilevers consisting of fiber, biaxial, and single crystalline microtextures. The cantilevers are actuated by applying a voltage across the active layer and the resulting displacement is measured via inspection with optical microscopy. We are able to relate the macroscopic device performance to the microscopic piezoelectric constants via multimorph calculations.

Our experiments show that ferroelectric thin film device performance may be enhanced by improving the underlying grain scale crystalline microstructure - from fiber to biaxial to single crystal texture.

Table of Contents

List of Figures

List of Tables

Chapter 1

Introduction

1.1 Background

The seven Bravais lattices may be classified into 32 point groups based on atomic arrangement and symmetry. Of these groups, 20 are noncentrosymmetric. These materials are known as piezoelectric (Nye, 1957). Within the noncentrosymmetric crystals, 10 have a dipole present in the unit cell and these are known as ferroelectric. Ferroelectric materials are polar and switchable. A variety of materials exhibit this phenomenon (Jona and Shirane, 1962; Fatuzzo and Merz, 1967; Lines and Glass, 1979). Piezoelectric and ferroelectric will be used interchangeably in this dissertation as the materials considered, type ABO_3 perovskites (such as $PbTiO_3$ and $BaTiO_3$), are ferroelectric materials.

Figure 1.1 shows the classic ferroelectric material $BaTiO_3$. It is centrosymmetric and cubic above its Curie temperature, 120 °C. When cooled below the Curie temperature, the material becomes tetragonally distorted and a spontaneous electrical polarization results along the now *c*-axis.

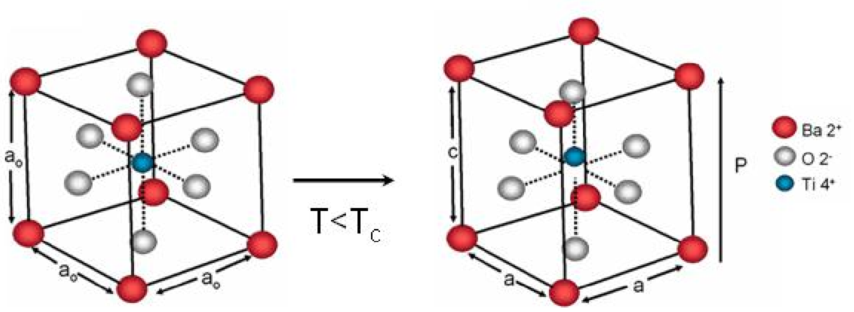

Figure 1.1: Crystal structures of $BaTiO_3$ in their cubic and tetragonal phase.

The direct piezoelectric effect is the linear relationship between stress σ_{jk} applied to a piezoelectric material and resulting charge density D_i:

$$D_i = d_{ijk}\sigma_{jk} \ , \tag{1.1}$$

where d_{ijk} is a third-rank tensor of piezoelectric coefficients. The reverse effect is true as well, as piezoelectric materials change dimensions when an electric field is applied to them. The converse piezoelectric effect is defined as the resulting strain ϵ_{ij} due to the applied electric field E_k on the piezoelectric material:

$$\epsilon_{ij} = d_{kij}E_k = d^t_{ijk}E_k \ . \tag{1.2}$$

where t denotes the transposed matrix. The piezoelectric coefficients d for the direct and converse piezoelectric effects are identical. Also, because the strain and stress are symmetrical fourth-rank tensors, the piezoelectric coefficient tensor is a third-rank and symmetrical tensor and thus, $d_{ijk} = d_{ikj}$. The number of independent piezoelectric coefficients is thus reduced from 27 to 18. The number of independent elements of d_{ijk} may be further reduced by the symmetry of the material (Damjanovic, 1998). For the 4MM materials $BaTiO_3$ and $PbTiO_3$, for instance, there are only three independent piezoelectric coefficients. The 4MM d tensor, rewritten in Voight notation, is:

$$\begin{bmatrix} 0 & 0 & 0 & 0 & d_{15} & 0 \\ 0 & 0 & 0 & d_{15} & 0 & 0 \\ d_{31} & d_{31} & d_{33} & 0 & 0 & 0 \end{bmatrix} . \tag{1.3}$$

When an electric field is applied, the mechanical response has two contributions: intrinsic due to the changes in polarization at the atomistic scales and extrinsic due to switching of domains (Bhattacharya and Ravichandran, 2003). Considering the former contribution, when a field is applied to a randomly oriented polycrystalline material, domains (regions of uniform polarization) align with respect to the applied field to give a net polarization that saturates at value P_{sat}. When the field is removed, a remanent polarization (P_r) persists. Once an opposite field is applied, the polarization reduces back to zero at the characteristic coercive field (E_c) and then with the continued application of such a field, the polarization

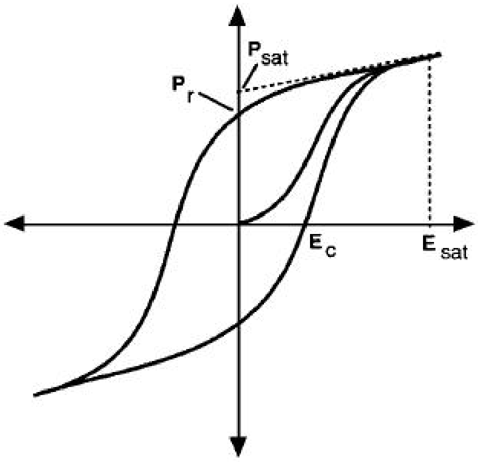

Figure 1.2: A polarization vs. electric field hysteresis loop.

switches directions and saturates once again. This characteristic piezoelectric hysteresis loop is depicted in Figure 1.2 (Polla and Francis, 1998).

To understand the extrinsic mechanical response contribution under applied electric field, we notice that the transformation from cubic to tetragonal at the Curie temperature may result in any of six symmetry-related variants as shown in Figure 1.3 (Bhattacharya and Ravichandran, 2003). Thus, the ferroelectric crystal at room temperature can exist in six equivalent forms. These variants are collected in the crystal as domains of a single variant and are separated by domain walls. Since the variants have equal energy, it is possible to switch one to the other, with applied electric field or mechanical load. The phase diagram for this switching is shown in Figure 1.4 (Bhattacharya and Ravichandran, 2003). If the domains are switched by 90° under some non-zero applied stress, the strain generated may be equal to the tetragonal distortion $(c/a-1)$ where a and c are the lattice parameters. The a lattice parameter of $BaTiO_3$ is 3.994 Å and c is 4.038 Å. $PbTiO_3$ has a equal to 3.905 Å and c as 4.151 Å (Shirane et al., 1950). Thus we can expect strains of around 1% for $BaTiO_3$ and 6% for $PbTiO_3$. Burcsu et al., following the analysis in (Shu and Bhattacharya, 2001), have demonstrated 1% strains via 90° domain switching under moderate electric fields in $BaTiO_3$ single crystals using the flat plate configuration shown in Figure 1.4 (Burcsu et al., 2000). Details of the switching experiment, with domain images and polarization and strain hysteresis curves, are shown in Figure 1.5 (Bhattacharya and Ravichandran, 2003).

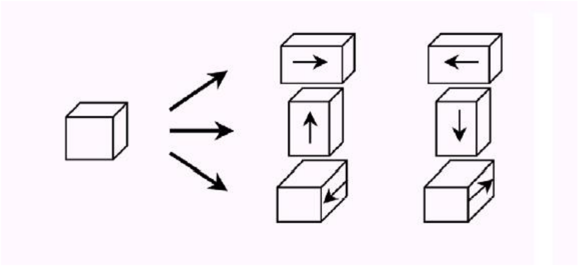

Figure 1.3: Six tetragonal variants of ABO_3 perovskites such as $BaTiO_3$ and $PbTiO_3$.

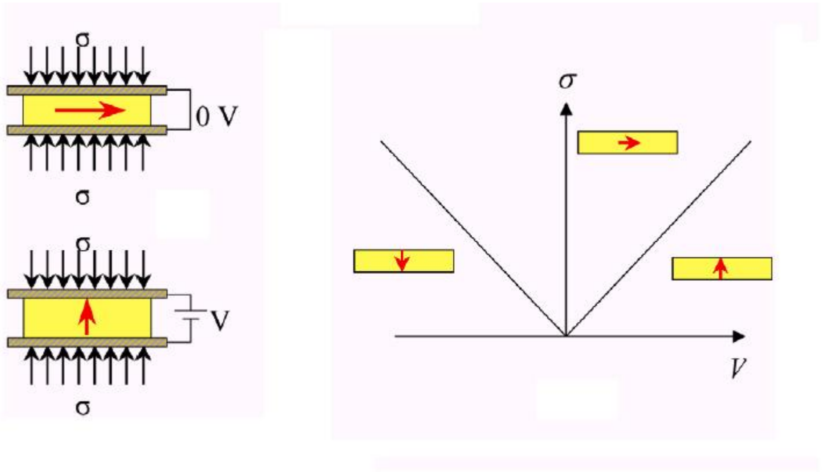

Figure 1.4: Left: flat plate configuration subjected to constant load and cyclic electric field. Right: phase diagram (applied stress vs. electric field) for single domain switching.

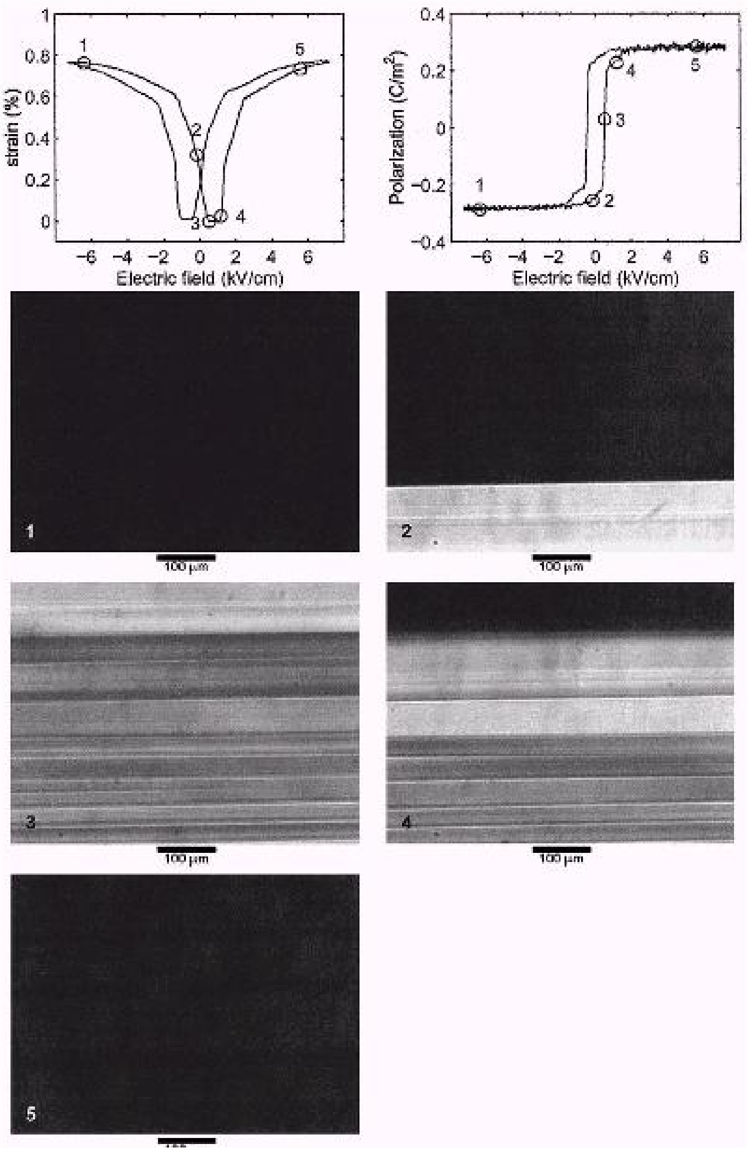

Figure 1.5: In-situ visualization of domain patterns through birefringence using transmission polarized light microscopy in single crystal $BaTiO_3$ at various values of electric field at a constant applied compressive stress of 1.07 MPa. Dark and light intensity indicate domains oriented along out-of-plane (001) and in-plane (100) directions, respectively.

1.2 MEMS

Microelectromechanical systems (MEMS) continues to be an exciting multidisciplinary field with tremendous progress taking place in research and commercialization. MEMS takes advantage of well-established manufacturing methods routinely used in the integrated circuit industry to make intelligent devices and systems capable of sensing, actuating, and processing information (Polla and Francis, 1998). MEMS pattern definition methods, commonly referred to as micromachining (Madou, 1997; Rai-Choudhury, 1997), are utilized to fabricate mechanical structures that are often realized using CMOS (complementary symmetry metal oxide semiconductor) processing. MEMS technology has been applied in the fields of defense, controls, communications, automobiles, and medicine.

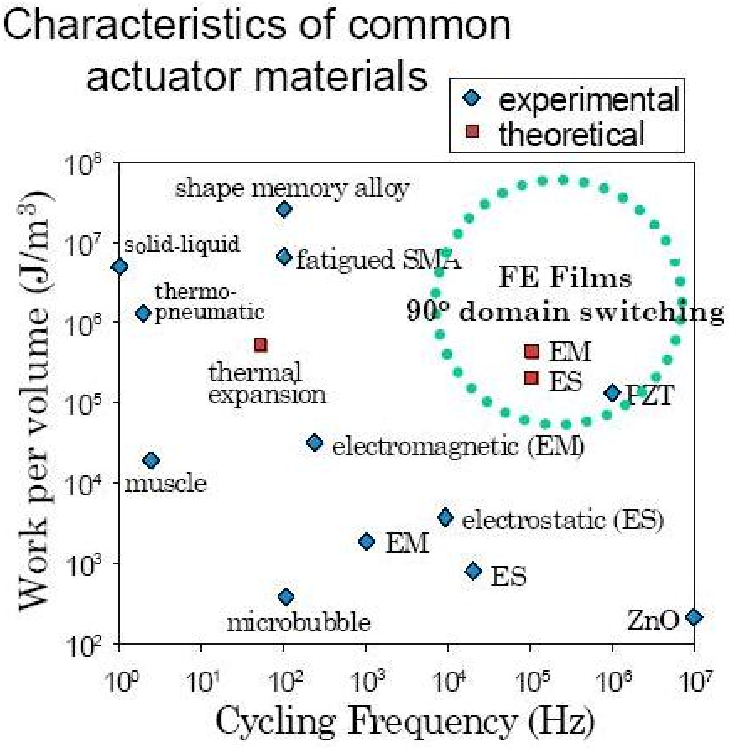

Figure 1.6: Work vs. frequency response characteristics of common actuator materials.

MEMS are classified into two major categories: sensors and actuators. MEMS sensors predictably deform or respond to a specific physical or chemical variable, and their response may be detected via electronic and optical effects. Examples of microsensors include accelerometers, pressure sensors, strain gauges, flow sensors, thermal sensors, chemical sensors, and biosensors. MEMS actuators' responses are usually the result of electrostatic, piezoelectric, magnetic, thermal, or pneumatic forces. Examples of microactuators include positioners, valves, pumps, deformable mirrors, switches, shutters, and resonators (Polla and Francis, 1998). This thesis will only discuss MEMS actuator devices. Ferroelectric-based MEMS, especially those that may exploit 90° domain switching, are generally attractive due to their high-force output in actuation applications, as seen in Figure 1.6 (Krulevitch et al., 1996).

Miniaturized ferroelectric actuators for MEMS applications will typically involve thin films, and thus the research and development must involve consideration of distinct deposition textures and constraints due to the substrate. Also, to achieve sophisticated MEMS that fully employ the intrinsic and extrinsic mechanical responses, the control of texture and micromachining is a necessary engineering challenge. It is clear that improving electromechanical actuation in perovskites requires an understanding at many different levels starting from the atomistic all the way to the level of the device.

1.3 Thesis Theme

This work aims to answer a fundamental question in the field of materials science: how do microscopic material properties affect the macroscopic device performance? This thesis realizes microstates along continuum shown in Figure 1.7 and attempts to correlate the ferroelectric properties of the thin films to devices. The study will utilize basic materials calculations and the testing of simple MEMS actuator devices.

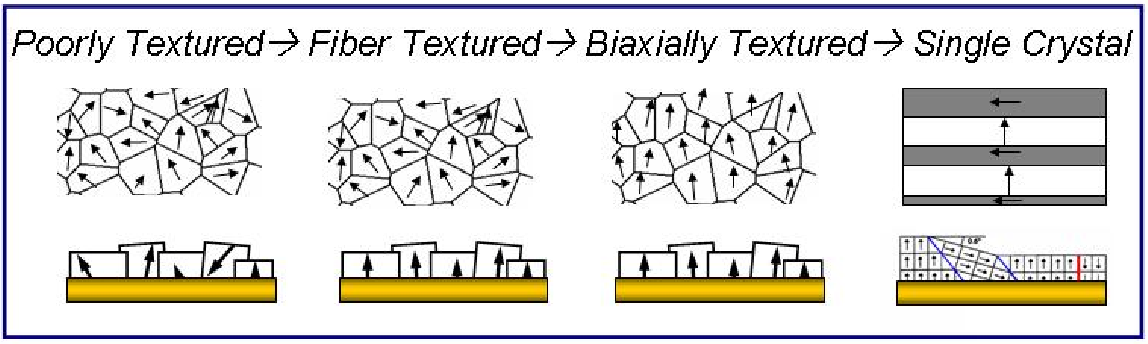

Figure 1.7: Thesis research theme: how microstructure along continuum affects devices of each texture type.

Thin films of each type are realized with polycrystalline deposition techniques and microstructures are controlled via templates and growth methods described in the following section.

1.4 Thin Film Growth

1.4.1 Pulsed laser deposition

Pulsed laser deposition (PLD), shown schematically in Figure 1.8 (El-Naggar, 2006), has a relatively simple setup yet is a highly efficient method of thin film deposition. A high power laser is focused inside a vacuum chamber and is pulsed to strike a ceramic target of the desired stoichiometry. Material is vaporized from the target and condenses on a heated substrate that is exposed to the ejected plume. Oxygen is used as a background gas to oxygenate the deposited thin films. An often-considered drawback of PLD is the presence of micron-sized particles in the deposited films, but these particulates may be controlled by increasing the working distance. The KNI facility at Caltech maintains a PLD system with an eximer laser with KrF gas and capabilities for several targets, such that materials may be deposited in succession without breaking vacuum.

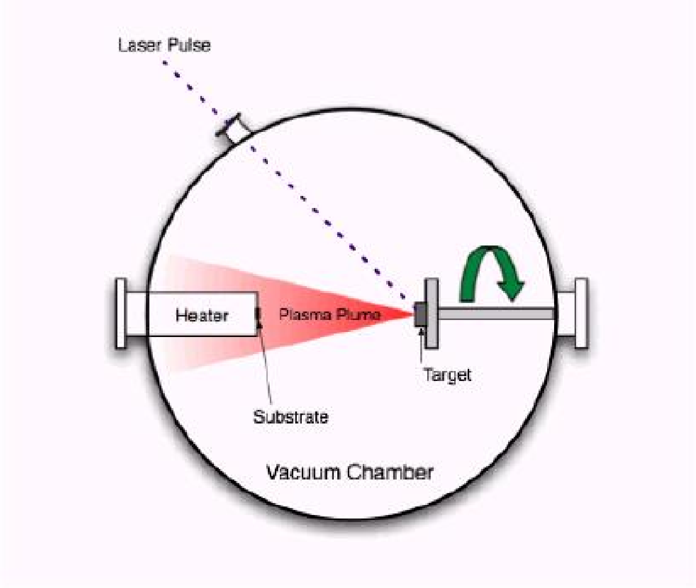

Figure 1.8: Schematic of PLD technique for thin film deposition.

1.4.2 Chemical vapor deposition

Chemical vapor deposition (CVD) is a film growth technique where a heated substrate is exposed to volatile precursors that react or decompose on the substrate surface, resulting in the desired thin film stoichiometry. CVD is regarded as one of the most cost-effective means of high-throughput, high-quality thin film deposition of semiconductor and oxide layers in device production (El-Naggar, 2006). The Goodwin group at Caltech maintains a reactor for metalorganic chemical vapor deposition (MOCVD); a variant of CVD that uses organometallic compounds as source materials. The reactor schematic is shown in Figure 1.9 and highlights the capability to grow $Pb_xBa_{1-x}TiO_3$ thin films (El-Naggar, 2006). Solid precursors sublimate in thermally controlled "bubblers" and are passed through optical cells. The gas phase stoichiometry of Pb, Ba, and Ti are controlled by monitoring the UV absorption spectra. Finally, the precursors are mixed with O_2 and passed through a showerhead onto the heated substrate. The barium, lead and titanium precursors used are $Ba(tmhd)_2$, $Pb(tmhd)_2$ and $Ti(OPri)_2(tmhd)_2$, where OPri is di-isopropoxy and tmhd is 2,2,6,6-tetramethyl-3,5-heptanedione or $[(CH_3)_3CC(O)CHC(O)C(CH_3)_3]$.

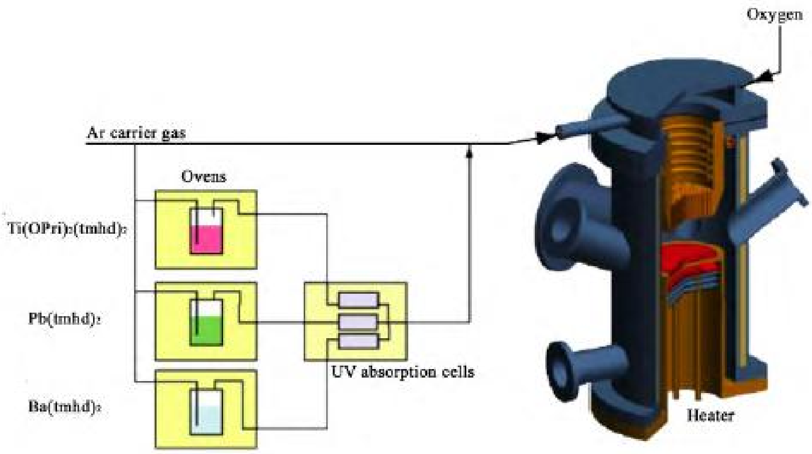

Figure 1.9: Schematic for MOCVD deposition process of $Pb_xBa_{1-x}TiO_3$ thin films featuring an ultraviolet-based control system for gas phase stoichiometry.

1.4.3 Ion beam-assisted deposition and MgO templates

Ion beam-assisted deposition (IBAD) is a process wherein physical vapor deposition on an amorphous substrate with simultaneous ion bombardment of the substrate results in a biaxially textured thin film. Given the lattice parameter of cubic MgO as 4.213 Å, it is expected and confirmed (Brewer, 2003; Brewer et al., 2005) that epitaxy of ferroelectrics like $BaTiO_3$ and $PbTiO_3$ will result in biaxial texture inheritance. Therefore, by using an intermediate MgO layer as a growth template, textured ferroelectrics may be realized on ultimately amorphous substrates.

MgO is evaporated with simultaneous 750-1200 eV Ar^+ ion bombardment at 45^o from normal incidence and ion/MgO flux ratios ranging from 0.3 to 0.6 in an ultra high vacuum

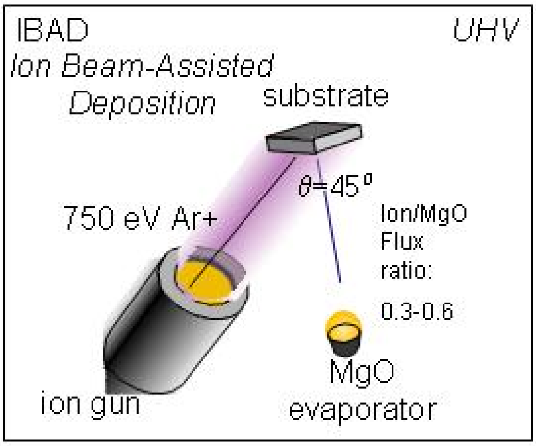

Figure 1.10: IBAD technique schematic for deposition of biaxially textured MgO.

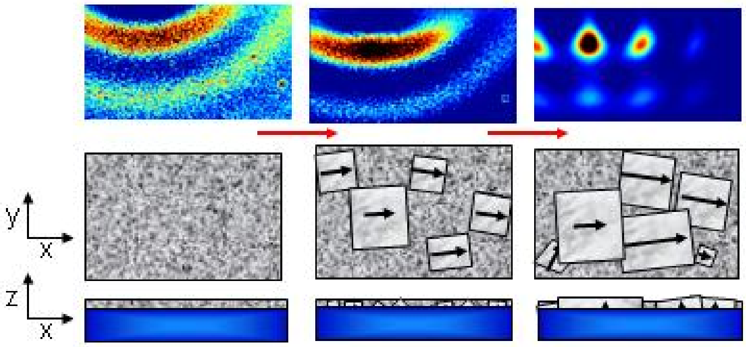

Figure 1.11: In situ RHEED images (top) suggest solid phase crystallization of MgO (schematically depicted on bottom). Biaxially aligned grains grow and overcome amorphous matrix.

system, shown schematically in Figure 1.10 (Brewer, 2003). During evaporation, the MgO film is first deposited as an amorphous matrix, but biaxial texture develops from solid phase crystallization, wherein misaligned grains are damaged by the ions and well-aligned grains continue to grow. This development is monitored by in-situ reflection high energy electron diffraction (RHEED), and the chronology is shown in Figure 1.11 (Brewer, 2003). By comparing final RHEED images to calculated RHEED images, the in- and out-of-plane texture may be determined, as the spot intensity and dimensions are proportional to the full width at half maximums (FWHM) of Euler angles, as depicted in Figure 1.12 (Brewer, 2003).

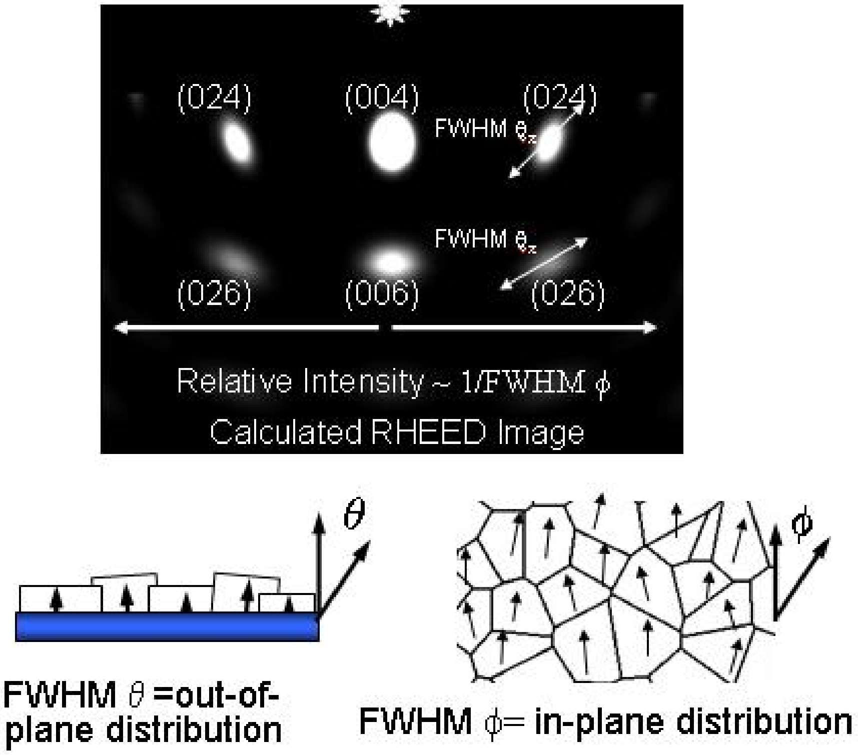

Figure 1.12: Calculated image compared to real image, FWHM of angles as described here.

By growing perovskite ferroelectrics on biaxially textured MgO (and a cap of additional homoepitaxial MgO) templates, we achieve biaxially textured materials (Brewer et al., 2005). The RHEED images of these materials may also be compared to calculated images to obtain quantitative values for texture, as seen in Figure 1.13. $Pb_xBa_{1-x}TiO_3$ inherits out-of-plane texture less than 5° FWHM and even narrows FWHM with respect to the in-plane orientation. Evidence from cross-sectional transmission electron microscopy (TEM)

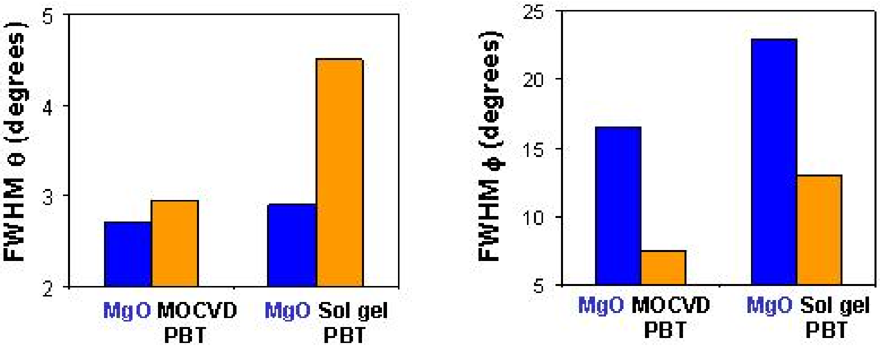

Figure 1.13: RHEED software gives quantitative evidence of texture inheritance. Sol gel and MOCVD were used to grow $Ba_xPb_{1-x}TiO_3$ (PBT) on MgO on amorphous Si_3N_4/Si.

(Figure 1.14 (Brewer, 2003)) shows crystalline perovskite and MgO films with a clear, sharp interface. Also, TEM clearly indicates that grain orientation and size propagates through the interface, and thus texture is realized in the ferroelectric layer.

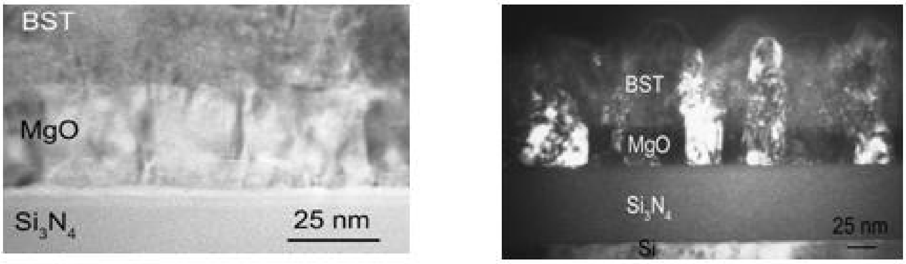

Figure 1.14: Light and dark field cross-sectional TEM of molecular beam epitaxy (MBE)-grown $Ba_{0.67}Sr_{0.03}Ti_{1.3}O_3$ (BST).

1.4.4 Oxide electrodes

Brewer et al. have demonstrated texture inheritance of perovskite materials on MgO templates, but from a device standpoint, active layers need to be incorporated with electrodes to access the switching mechanisms of these materials. Therefore, oxide electrodes become an interesting possibility for integrating ferroelectric materials into meaningful devices.

Over the past several years, considerable attention has been dedicated to $SrRuO_3$ thin films for use as oxide electrodes. $SrRuO_3$ in the pseudocubic configuration has a lattice parameter of 3.93 Å and therefore is well matched to $BaTiO_3$ and $PbTiO_3$ active layers

(Eom et al., 1993). El-Naggar (2006) has demonstrated that $SrRuO_3$ thin films inherit biaxial texture from MgO templates, which is novel considering previous characterization work has usually focused on $SrTiO_3$ and $LaAlO_3$ substrates (Jiang et al., 1998; Jia et al., 1997). $SrRuO_3$ is therefore utilized both as a template and device electrode throughout this thesis work.

1.5 Thesis Outline

Chapter 2 presents a model for determining the effect of texture on electromechanical properties of 4MM symmetry perovskite $BaTiO_3$ and $PbTiO_3$. This work is novel for considering biaxial texture, as previous work had only considered single angle fiber texture. Materials constants of piezoelectric displacement, stiffness, and dielectric are considered, as an understanding of these values will aid in device engineering and performance.

Chapter 3 discusses $PbTiO_3$ bridge devices that are actuated via applied loads. $PbTiO_3$ was chosen as the active material for these initial devices in the hopes of accessing the large 6% strain. Bridges were chosen as the geometry allows for clamping on both ends and therefore results in an elevated stress state. Thus the testing aim was to produce 90° domain switching in the ferroelectric layer with applied load. However, despite testing being repeatable and robust, the films experienced cracking. Nevertheless, this cracking was studied and correlated to the device response. Force-displacement data allowed moduli and initial stresses of the bridges to be fit using beam stretch theory.

In Chapter 4, microstructures of fiber, biaxial, and single crystal texture are realized in $BaTiO_3$ on $SrRuO_3$ electrodes on MgO templates and substrates. Cantilever devices are micromachined from the monolithic samples using focused ion beam (FIB) milling and voltage-induced bending is studied using a multimorph beam bending model. Thus a perspective of how microstructure affects device performance is established.

Chapter 5 is summary of major topics presented in this thesis and suggests possibilities for future work, including an introduction to single crystal films via wafer bonding and layer transfer method. Similarly to how the present chapter has begun to motivate the field of ferroelectricity and relevant devices, so has this thesis work only begun to investigate the fundamental relationships across length scales in these materials.

Chapter 2

The Effect of Biaxial Texture on the Effective Electromechanical Constants of Polycrystalline Barium Titanate and Lead Titanate Thin Films

2.1 Abstract

Effective electromechanical constants as a function of biaxial crystallographic texture in polycrystalline films are modeled using a self-consistent approach. The film is modeled by assuming Gaussian distributions of two Euler angle textures about perfect orientation with varying spread, or full width at half maximum. We see that independent in-plane texturing has little effect on the piezoelectric displacement tensor. Increased out-of-plane texturing gives rise to an enhanced piezoelectric effect for barium titanate films, but not for lead titanate. Twist texturing about these out-of-plane angles shows a further enhancement in the non-shear components of the piezoelectric displacement tensor for both materials. Single crystal stiffness and dielectric constants for barium and lead titanate are similar, and, as such, the trends in effective constants with texture are similar. Finally, we use the effective piezoelectric coupling factor as the primary figure of merit for the effective piezoelectric properties of polycrystalline devices, thus utilizing all electromechanical constants of this simulation. The effective piezoelectric coupling factor shows a primary dependence on the out-of-plane texture.

2.2 Introduction

Piezoelectric materials have long been studied for their interesting electromechanical properties. The fact that piezoelectric, elastic, and dielectric properties are coupled and switchable offers many engineering freedoms, particularly in thin films. The realization of these materials in thin film form allows for the miniaturization and integration of piezoelectric and electro-optic devices for applications in MEMS, integrated photonics, and other device technologies that can be integrated with silicon electronics.

Piezoelectric displacements and other electromechanical constants are easily quantified for single crystal materials (Berlincourt and Jaffe, 1958; Li et al., 1996), and the effects of rotation on these constants are also confirmed experimentally via slicing along varying orientations (Du et al., 1999; Harnagea et al., 2002). However, most traditional thin film growth methods (CVD, sol gel, PLD, etc.) result in polycrystalline films. In some cases, polycrystalline films can be fabricated with crystallographic microstructures that approach those of ideal single crystal materials, achieving grain orientation through epitaxial growth on lattice-matched substrates or a template layer (Brewer et al., 2003). More generally, polycrystalline films exhibit a distribution of grain orientations around a direction normal to the film plane or around a specific in-plane azimuthal orientation. Piezoelectric and electro-optic thin film devices typically have active regions whose dimensions are considerably larger than a single grain, and thus would be anticipated to exhibit effective properties that are characteristic of an appropriately determined ensemble response of many grains. Therefore, we consider the effect of the grain-scale mosaic spread in the crystallographic texture and orientation on the device-scale piezoelectric coupling factor achievable in thin film devices. Our method enables the effective electromechanical properties to be obtained for a polycrystalline film. We explore tetragonal 4MM symmetry group materials, and give specific results for barium titanate and lead titanate. We report here the results of self-consistent simulations of the properties of biaxially textured films (Ruglovsky et al., 2006), which elaborates upon work reported to date that has been only on the properties of fiber-textured films (Li et al., 1999; Zhou et al., 2005; Li, 2000).

2.3 Model

The method utilized in this paper is adapted from Li's consideration of effective electromechanical moduli of piezoelectric polycrystals, textured about one Euler angle (θ)(Li, 2000), with suitable modifications for incorporating a second Euler angle (ϕ or ψ) for biaxially textured films. A brief summary of Li's method and our modifications is described below.

Consider a polycrystalline thin film of a ferroelectric material, and assume that the grain size is small compared to the film thickness. It is then appropriate to calculate the effective properties of bulk ceramics and then apply them to the thin film setting (Shu, 2000). Each grain in the polycrystal has its own underlying domain pattern. At small and moderate applied stress and field, the domain patterns do not change, and each domain responds like a piezoelectric material with its own preferred orientation. This is the medium that is considered below. Thus, texture refers to information about both the grains and domains.

The response of a piezoelectric material is described by two constitutive equations, written in Voight tensor notation (Nye, 1957), wherein the electric and elastic fields are fully coupled:

$$\sigma_i = C_{ij}\epsilon_j - e_{ik}E_k \; , \tag{2.1}$$

$$D_l = e_{lm}\epsilon_m + \kappa_{ln}E_n \; . \tag{2.2}$$

The applied elastic stress is given by σ and the electric displacement is D. Elastic strain, ϵ, and electric field, E, are the field variables in the equations. The proportionality constants relating these values are C, e, and κ, which are elastic stiffness, piezoelectric stress constant, and dielectric constant, respectively. These constitutive equations may be combined in matrix representation with the following variables:

$$\Sigma = \begin{bmatrix} \sigma \\ D \end{bmatrix} , \; Z = \begin{bmatrix} \epsilon \\ -E \end{bmatrix} , \; G = \begin{bmatrix} C & e^t \\ e & -\kappa \end{bmatrix} \; . \tag{2.3}$$

Thus we may consider a single constitutive equation,

$$\Sigma = GZ \; . \tag{2.4}$$

The effective electromechanical constants of matrix G^* may be defined as

$$\langle \Sigma \rangle = G^* \langle Z \rangle \ , \tag{2.5}$$

where $\langle x \rangle$ refers to a volume average of variable x,

$$\langle x \rangle = \int (x) d\Omega(\theta, \psi, \phi) \ . \tag{2.6}$$

Li finds the G^* matrix as

$$G^* = \langle G(\theta, \psi, \phi) A(\theta, \psi, \phi) \rangle \ , \tag{2.7}$$

where $G(\theta, \psi, \phi)$ are the electromechanical moduli of a particular grain with orientation at Euler angles θ, ψ, ϕ with respect to the reference frame of sample. $A(\theta, \psi, \phi)$ is the concentration factor for a single grain with orientation at the same Euler angles θ, ψ, ϕ (angle definitions reviewed in Figure 2.1). This factor is a function of grain shape, orientation, and interaction of neighboring grains. A proper estimation of this factor is needed to determine the effective electromechanical constants.

In the self-consistent method, the concentration factor A is determined by assuming that individual grains are embedded in an infinite matrix with yet to be determined effective moduli G^*, subjected to yet to be determined external loading Z_1 at the boundary. Consider a single grain in the infinite matrix. Its response, Z, is related to the far field loading, Z_1, by:

$$Z(\theta, \psi, \phi) = A^{dil}(\theta, \psi, \phi) Z_1 \ , \tag{2.8}$$

$$A^{dil}(\theta, \psi, \phi) = \left\{ I + S(\theta, \psi, \phi) G^{-1}(\theta, \psi, \phi) [G(\theta, \psi, \phi) - G^*] \right\}^{-1} \ . \tag{2.9}$$

$A^{dil}(\theta, \psi, \phi)$ is the solution from the problem of a single spherical inhomogeneity embedded in an infinite matrix (Dunn and Taya, 1993). $S(\theta, \psi, \phi)$ is the piezoelectric Eshelby tensor for a spherical inhomogeneity at specified orientation expressed in the coordinate system of the sample. The assumption of a spherical inhomogeneity is a significant assumption since domains have a lamellar shape: however, it is reasonable for our limited purposes and easily modified. Domain configurations and their evolution are not considered, nor is phase transformation. When the applied electric field is small, this treatment is appropriate since the contribution from domain wall movement is small.

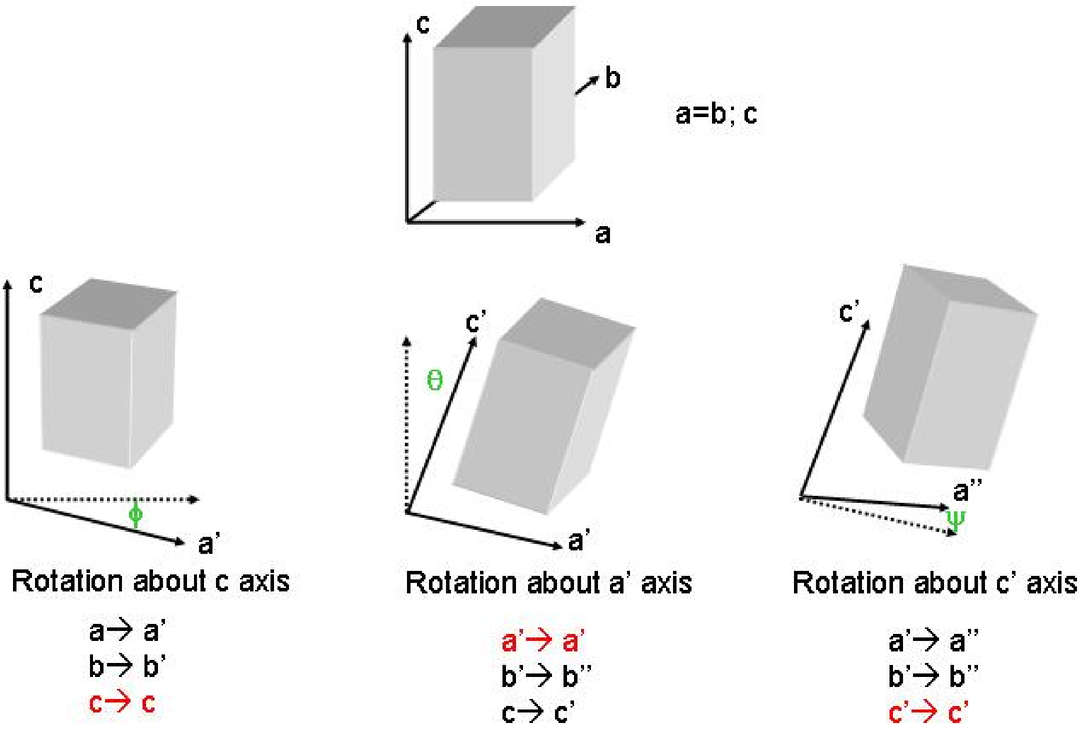

Figure 2.1: Euler rotations of tetragonal crystal. Angles θ, ψ, ϕ are shown.

Averaging all of these individual grains' responses and insisting that this average be consistent with the applied load Z^0, we obtain (Li, 2000):

$$Z_1 = \left\langle A^{dil}(\theta, \psi, \phi) \right\rangle^{-1} Z^0 \, , \tag{2.10}$$

where Z^0 is the uniform field.

Now,

$$A(\theta, \psi, \phi) = A^{dil}(\theta, \psi, \phi) \left\langle A^{dil}(\theta, \psi, \phi) \right\rangle^{-1} \, , \tag{2.11}$$

and therefore the effective constants are given by:

$$G^* = \left\langle G(\theta, \psi, \phi) A^{dil}(\theta, \psi, \phi) \right\rangle \left\langle A^{dil}(\theta, \psi, \phi) \right\rangle^{-1} \, . \tag{2.12}$$

This self-consistent approach has G^* on both sides of the equation, so the solution must be found numerically by iteration.

Clearly, the numerical solution requires volume averages. The distribution of grains is introduced as an Orientation Distribution Function (ODF), W, which is the orientational probability density function for each grain. Volume averages for an aggregate collection of such grains are then determined as follows:

$$\langle H \rangle = \int_0^{2\pi} \int_0^{2\pi} \int_{-1}^{1} H(\cos\theta, \psi, \phi) W(\cos\theta, \psi, \phi) d\cos\theta d\psi d\phi \, , \tag{2.13}$$

where $H(\cos\theta, \psi, \phi)$ is the single crystal value with reference to the grain's location in the sample. Our determination of G^* above has such a volume average for both $G(\theta, \psi, \phi)A^{dil}$ and A^{dil}. The integrals for each are solved by Gaussian quadratures, wherein the integral of a function is approximated by the sum of its function values at abscissas, multiplied by weighting coefficients.

The aggregate grains are assumed to have a Gaussian distribution. For biaxial texture, we use two combinations of angles for two separate ODFs, W_1 and W_2:

$$W_1(\theta, \psi, \phi) = \frac{1}{\alpha\sqrt{2\pi}} \frac{1}{\beta\sqrt{2\pi}} \mathrm{e}^{\left(-\frac{\theta^2}{2\alpha^2}\right)} \mathrm{e}^{\left(-\frac{\phi^2}{2\beta^2}\right)} \, , \tag{2.14}$$

$$W_2(\theta, \psi, \phi) = \frac{1}{\alpha\sqrt{2\pi}} \frac{1}{\gamma\sqrt{2\pi}} \mathrm{e}^{\left(-\frac{\theta^2}{2\alpha^2}\right)} \mathrm{e}^{\left(-\frac{\psi^2}{2\gamma^2}\right)} \, . \tag{2.15}$$

The parameters α, β, and γ are increasing figures of merit to describe worsening texture for Euler angles θ, ϕ, and ψ, respectively. As α, β, $\gamma \to 0$, we approach perfectly aligned grains which are thus indistinguishable from single crystals, and as α, β, $\gamma \to \infty$ we approach a randomly oriented, non-piezoelectric film. In both ODFs, the angle that does not appear (ψ for W_1 and ϕ for W_2) is assumed to be randomly distributed within the film.

Recently Brewer et al. (2005) devised a RHEED-based analysis technique to determine quantitative full width at half maximums (FWHMs) of in- and out-of-plane texture angles for the piezoelectric films. The parameters α and β in the above ODF W_1 can be directly compared to the FWHM of θ and ϕ given from the RHEED experiment. Thus the effective properties of a collection of grains in a device may be correlated with experimental observations of biaxial texture. Narrow distributions approaching single crystal texture have been realized with measured FWHM θ around 3° and FWHM ϕ around 7°. The second case of biaxial texture, depending on parameters α and γ, would be more difficult to measure experimentally, as the Euler angle ψ is only measured once the grain has been displaced by Euler angle θ. Nevertheless, one could imagine a rocking curve scheme where the out-of-plane angle θ was situated, and an entire rocking curve for an in-plane angle about that θ was obtained, giving the texture about ψ, with respect to the original sample reference frame.

The results of this simulation are three-dimensional surfaces of effective constants (e, C, and κ) with input α and β or γ, herein referred to as FWHM θ, FWHM ϕ and FWHM ψ.

2.4 Results and Discussion

The theory described above is applied to barium titanate and lead titanate polycrystals. Both of these perovskite materials exhibit 4MM symmetry, but the single crystal piezoelectric constants of each may differ significantly, as seen in Table 2.1 (Zgonik et al., 1994; Li et al., 1996). These differences contribute to the extent of the effect of texture on each material's electromechanical properties.

2.4.1 Piezoelectric strain constant

As piezoelectric devices are often characterized by piezoelectric strain coefficient d, defined as $d_{ij} = \epsilon_i / E_j$, we begin the analysis with this electromechanical constant. The constitutive

	C_{11} (GPa)	C_{12} (GPa)	C_{13} (GPa)	C_{33} (GPa)	C_{44} (GPa)	C_{66} (GPa)
BTO	222	108	111	151	61	134
PTO	235	101	98.8	105	65.1	104
	e_{31}(C/m^2)	e_{33}(C/m^2)	e_{15}(C/m^2)	κ_{11}/κ_0	κ_{33}/κ_0	
BTO	-0.7	6.7	34.2	2200	56	
PTO	-0.98	3.35	3.92	80	34	

Table 2.1: Material constants for barium titanate (BTO) and lead titanate (PTO) single crystals, where C is elastic stiffness, e is piezoelectric stress constant, and κ is the dielectric constant.

equations given above rely on the e value, or piezoelectric stress constant. This tensor is easily converted to d by normalizing with C, the stiffness tensor.

2.4.1.1 Biaxial texture with mosaic spread about ϕ and θ

Biaxial texture with mosaic spread about the ϕ and θ Euler angles is analogous to a thin film polycrystal with in- and out-of-plane texturing, rotating the z- (out-of-plane) and x- and y-axes (in-plane) independently. Only d_{31}, d_{33}, and d_{15} piezoelectric constants are non-zero in 4MM symmetry. It should be noted at this time that the subscripts of these constants are meaningful for device applications. The d_{31} constant relates the induced strain in direction 1 per unit electric field in direction 3, and likewise d_{33} relates the induced strain in direction 3 per unit electric field applied in direction 3. Finally, d_{15} is the shear strain induced about axis 2 (in 1-3 plane) per unit electric field applied in direction 1. Results for d tensor components for both barium titanate and lead titanate (at FWHM ϕ=0 cross-section) are shown in Figure 2.2. Consistent with Li's results (Li, 2000) for a fiber-textured polycrystal, we see that for barium titanate, values d_{31} and d_{33} show an increase from single crystal values with some critical texturing about Euler angle θ. However, this enhancement is not seen in lead titanate.

The difference between barium titanate and lead titanate can be attributed to the single crystal piezoelectric displacement tensor values for each tetragonal material. Consider the effect of rotation on the single crystal value d_{zz} measured at an angle θ with respect to the [001] direction:

$$d_{zz} = d_{33}\cos^3\theta + (d_{15} + d_{31})\cos\theta\sin^2\theta\ . \tag{2.16}$$

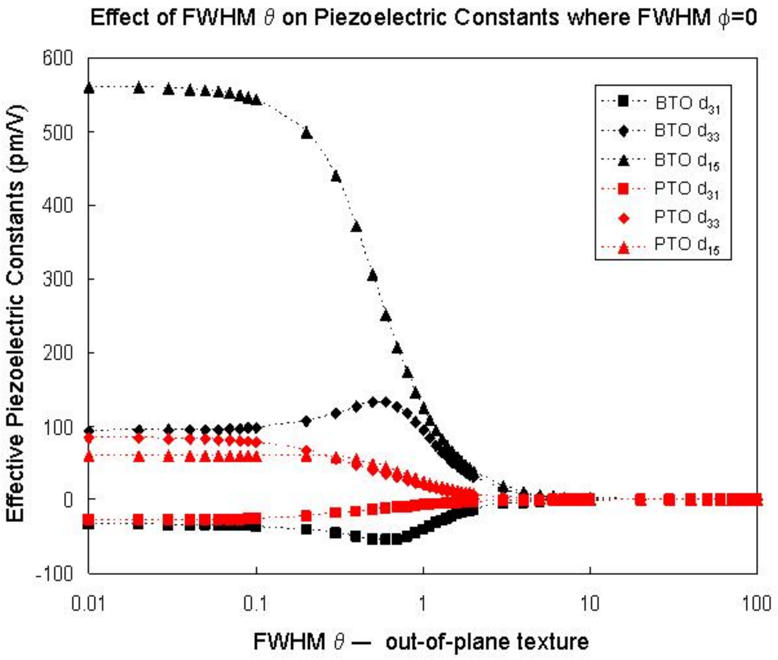

Figure 2.2: Variation of effective piezoelectric displacements d_{31}, d_{33}, and d_{15} with the FWHM of the out-of-plane texture distribution for textured barium titanate (BTO) and lead titanate (PTO) polycrystalline films (FWHM ϕ=0).

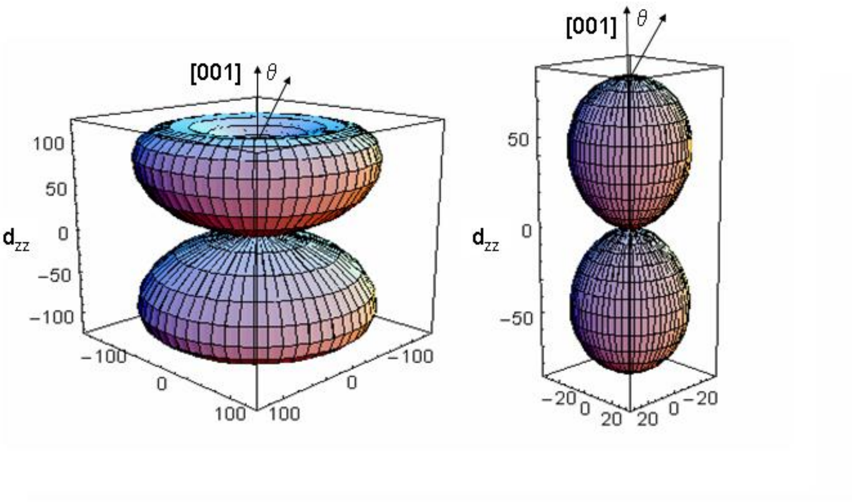

Figure 2.3: Variation of perpendicular piezoelectric displacement d_{zz}, for barium titanate (left) and lead titanate (right), with polar angle θ, under applied perpendicular E-field.

This is displayed in Figure 2.3. We see that barium titanate actually has a higher d_{zz} at some angular rotation θ away from the [001]. The maximum d_{zz} is at θ=52°, close to the [111] orientation. The highest value for lead titanate, on the other hand, exactly coincides with the [001] direction. Thus the effect of rotating barium titanate grains with respect to the applied field will increase its effective piezoelectric constants, whereas those of lead titanate will decrease monotonically. We also therefore remark that a polycrystalline barium titanate film with [111] texture would have a higher effective piezoelectric displacement d_{zz} than a [001] textured polycrystal.

The single crystal plots of the piezoelectric constant for each material in Figure 2.3 also give us insight into the effects on piezoelectric displacement from texturing about Euler angle ϕ, or in-plane texturing. For both barium and lead titanate, the single crystal plots above have azimuthal symmetry. Thus we expect very little effect on the effective piezoelectric constant via variation of in-plane texture. We have found that this is indeed the case. The FWHM ϕ=0 curve is shown in Figure 2.2. However, there is a slight effect of in-plane spread in barium titanate's effective d_{33} constant, depicted in Figure 2.4, and a mirrored enhancement in the effective d_{31} value (not shown). Since the piezoelectric tensor transformations are independent of ϕ, (Appendix A) we conclude that the slight enhancement must

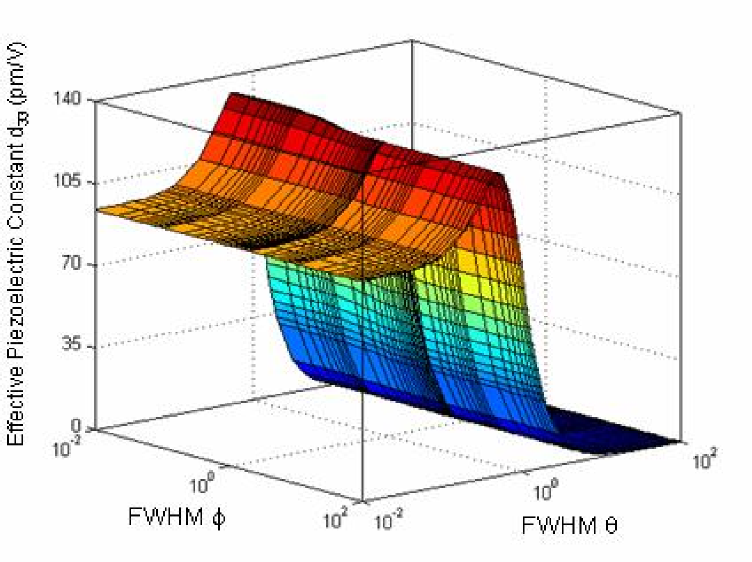

Figure 2.4: Variation of effective piezoelectric displacements d33 with the FWHM of the in- and out-of-plane texture distribution for a textured barium titanate polycrystalline film.

be due to the intergranular constraints, brought out from the self-consistent simulation.

Finally, the results for d_{31}, d_{33}, and d_{15} for both materials show that with increasing FWHM θ (indicating a degradation of fiber texture to a completely random polycrystal), all the effective piezoelectric constants asymptotically approach 0, indicating the polycrystal has become non-piezoelectric, as expected.

2.4.1.2 Biaxial texture with mosaic spread about ψ and θ

The second case of biaxial texture considered is one which allows each grain to rotate about the Euler angles θ and ψ. This corresponds to a film with grains possessing some out-of-plane rotation from a z-axis, perpendicular to the plane of the film, and some in-plane rotation about the newly rotated axis.

In Figure 2.5, at low FWHM ψ there is a pronounced variation in d_{33} and d_{31} in barium titanate and a slighter variation for the same components of lead titanate. There is very little effect of spread in ψ for the d_{15} component (data not shown). It does seem reasonable that a lower "twist" ψ about each out-of-plane angle θ would give rise to higher values of

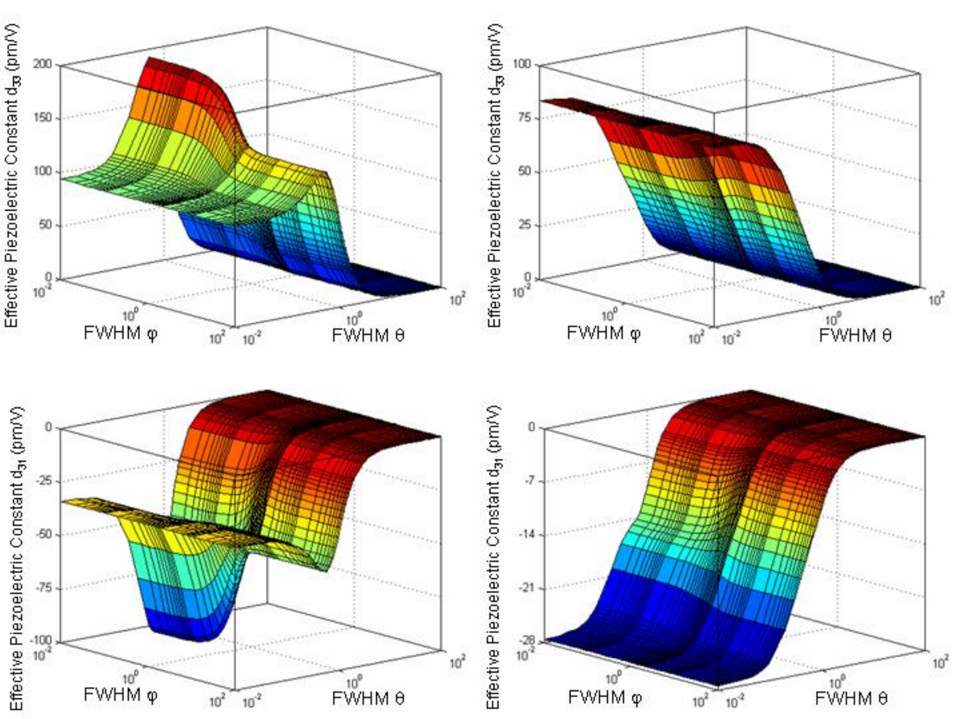

Figure 2.5: Variation of effective piezoelectric displacements d_{33} and d_{31} with the FWHM of the out-of-plane and twisted texture distribution for textured barium titanate (left column) and lead titanate (right column) polycrystalline films.

piezoelectric displacement, as tetragonal grains would be well oriented in the normal plane to the new out-of-plane axis, and that the shear component d_{15} would not be as sensitive to this twist. Shown also is the dependence on both angles from the single crystal rotation matrices with transformations depending on θ and ψ. The piezoelectric tensor depends on both angles, unlike the rotation about θ and ϕ, which only depends on θ (Appendix B). Finally we remark about the asymptotes. As FWHM θ increases, the piezoelectric constants asymptote to those of a random and non-piezoelectric polycrystal, with piezoelectric constants equal to 0, and as FWHM ψ increases, we generate an identical curve to the d values of the previous section, as ψ becomes randomly distributed.

2.4.2 Stiffness constant

The stiffness tensor is a fourth-rank tensor with six non-zero components for materials with 4MM symmetry. The stiffness values are analogous to the Young's modulus, a value commonly quoted to describe the elasticity of the material, via Hooke's law. A polycrystal's behavior under an applied load will greatly depend on the effect of texture, as described below. Non-shear constants C_{13} and C_{33} (stiffness with stress applied in principal stress directions 1 and 3, respectively, causing a tensile strain in 3 direction) are discussed.

2.4.2.1 Biaxial texture with mosaic spread about ϕ and θ

The effective stiffness constant C_{13} decreases with increasing texture about θ, as seen in Figure 2.6. However, it decreases less severely with low FWHM ϕ. Thus more alignment in-plane will generate a higher effective stiffness in the 3-direction when the stress is applied in the 1-direction. The same trends are evident for lead titanate, but less percentage recovered as single crystal value is smaller. Appendix C shows the dependence of each constant on θ and ϕ when the single crystal tensor is rotated by both angles.

The effective C_{33} stiffness constant increases with FWHM θ (Figure 2.7). Furthermore, at high FWHM θ and FWHM ϕ, the C_{33} value is at a maximum. The same effect is also seen in lead titanate but to smaller extent, once again because the single crystal C_{33} value is smaller. It should be noted that this is the first indication that not only can slight texturing improve an electromechanical constant, but purely 'random' texture can actually maximize it. Random in- and out-of-plane texture allow a crystal stressed in the 3-direction to strain

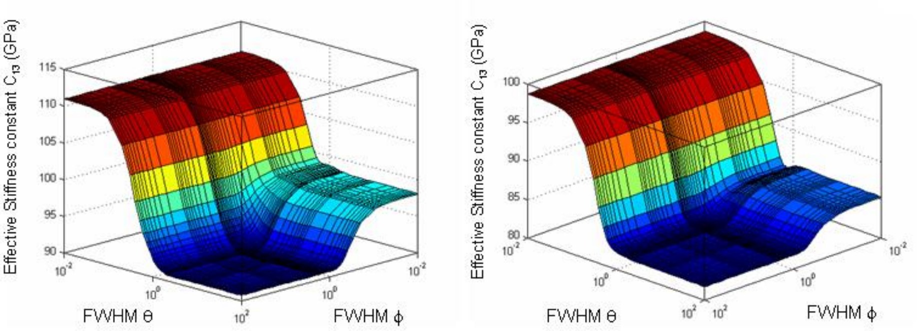

Figure 2.6: Variation of effective stiffness constant C_{13} with the FWHM of the in- and out-of-plane texture distribution for textured barium titanate (left) and lead titanate (right) polycrystalline films.

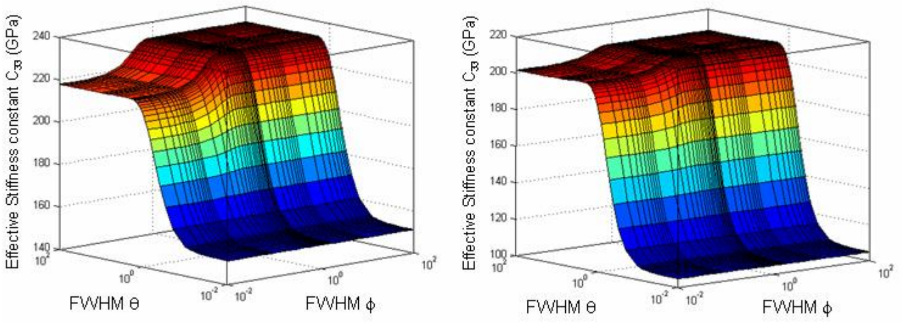

Figure 2.7: Variation of effective stiffness constant C_{33} with the FWHM of the in- and out-of-plane texture distribution for a textured barium titanate (left) and lead titanate (right) polycrystalline films.

significantly less in the same 3-direction. Thus a randomly oriented polycrystal has the potential to be useful in high stiffness applications.

2.4.2.2 Biaxial texture with mosaic spread about ψ and θ

The effective C_{13} constant with biaxial texture about ψ and θ is very similar to the case of biaxial texture about ϕ and θ. As seen in Appendix D, the rotated single crystal tensor components are somewhat similar.

There is little effect from texturing about ψ on the effective C_{33} constant (Figure 2.9). There is an increase in the constant with worsening texture about θ, indicating some material hardening. The single-angle dependence is easily explained by considering the single

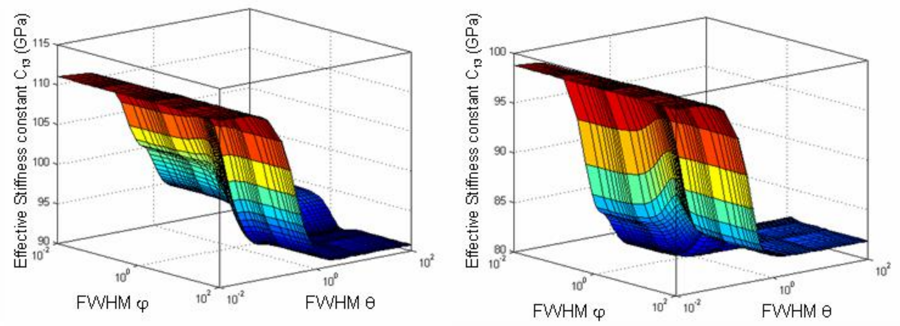

Figure 2.8: Variation of effective stiffness constant C_{13} with the FWHM of the out-of-plane and twisted texture distribution for textured barium titanate (left) and lead titanate (right) polycrystalline films.

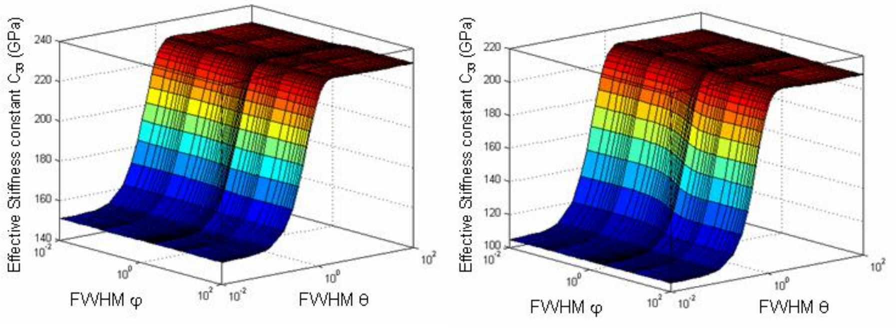

Figure 2.9: Variation of effective stiffness constant C_{33} with the FWHM of the out-of-plane and twisted texture distribution for textured barium titanate (left) and lead titanate (right) polycrystalline films.

crystal rotation in Appendix D. The rotated C_{33} constant shows only dependence on θ. Thus any texture about angle ψ will not harden the material any further.

2.4.3 Dielectric constant

The dielectric constant is of fundamental importance in insulating materials and particularly in polarizable materials such as ferroelectrics. The dielectric matrix for 4MM materials has only two nonzero components, the κ_{11} and κ_{33}. By controlling the grain orientation, one may engineer various capacitive devices.

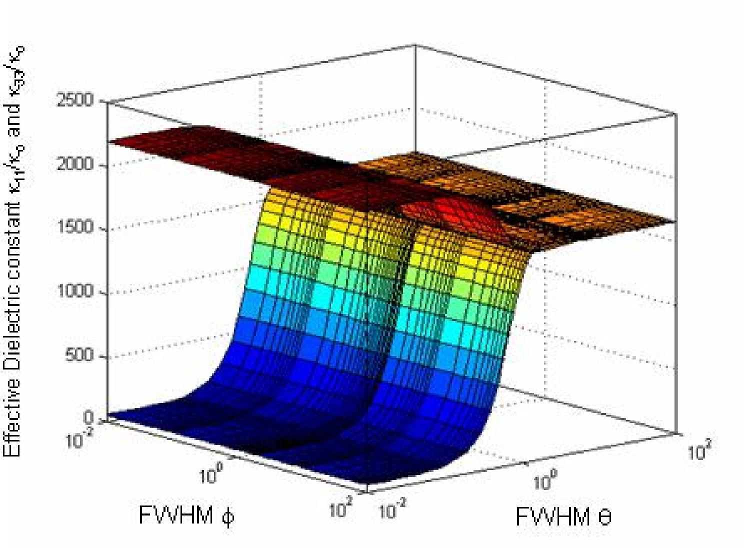

Figure 2.10: Variation of effective dielectric constants κ_{11} (top surface) and κ_{33} (bottom surface) with the FWHM of the in- and out-of-plane texture distribution for a textured barium titanate polycrystalline film.

2.4.3.1 Biaxial texture with mosaic spread about ϕ and θ

Figure 2.10 shows the effective dielectric constants of barium titanate as a function of spread in in- and out-of plane angle. The κ_{11} value monotonically decreases with increasing FWHM θ as the κ_{33} shows a monotonic increase. The two values ultimately converge to a single value or the limit of a purely isotropic material. There is no dependence on the texture of the in-plane angle ϕ. This is obvious from Appendix E, as the single crystal dielectric tensor rotated by two angles θ and ϕ exhibits no dependence on ϕ. The results for lead titanate are quite similar, as lead and barium titanate have similar dielectric constants.

2.4.3.2 Biaxial texture with mosaic spread about ψ and θ

The effective κ_{33} constant is only slightly decreased at low FWHM ψ, as seen in Figure 2.11 for barium titanate. In Appendix F we see that the rotated 33 value has no ψ dependence and thus the slight enhancement is due to other aspects of the simulation. On the other hand, the 11 and 22 terms in the rotated single crystal matrix depend on both θ and ψ. Thus the enhancement in κ_{11} seen in Figure 2.11 with small ψ is expected. Interestingly, the

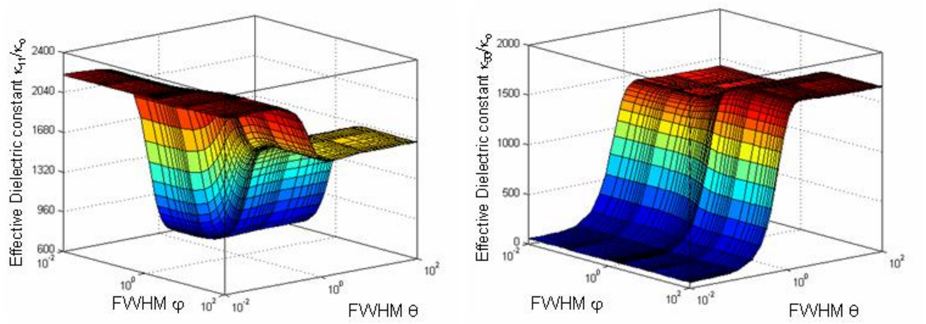

Figure 2.11: Variation of effective dielectric constants κ_{11} (left) and κ_{33} (right) with the FWHM of the out-of-plane and twisted texture distribution for textured barium titanate polycrystalline films.

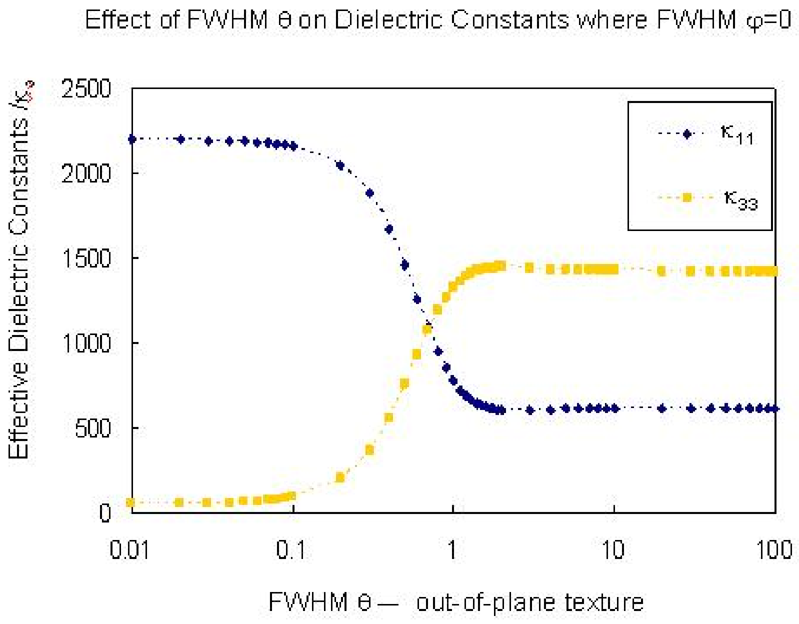

Figure 2.12: Variation of effective dielectric constants κ_{11} and κ_{33} with the FWHM of the out-of-plane texture distribution and the FWHM of the twist texture at zero for textured barium titanate polycrystalline films.

enhancement at low FWHM ψ is such that the decrease of ψ with increasing FWHM θ is much more rapid, and the κ_{11} surface intersects the κ_{33} surface at a single value (indicating an isotropic material for that set of textures) and then is in fact lower than the κ_{33} surface! This is seen in Figure 2.12 for a FWHM ψ=0. Once again, these results are all comparable to lead titanate because of the similarities in single crystal dielectric constants between the two materials.

2.4.4 Piezoelectric coupling factor

As a final component of our analysis and discussion, we perform analysis in terms of a meaningful figure of merit for piezoelectric performance in polycrystalline film-based devices. Traditionally, piezoelectric displacement has been used as a figure of merit, hence the detailed analysis above. However if the application required a more detailed prediction of device performance, incorporating robustness of the film and support of fields, we would instead chose the primary figure of merit for performance of polycrystalline thin film devices, the piezoelectric coupling factor, k, defined as the stored mechanical energy per unit input electrical energy (Uchino, 2000):

$$k = \frac{d^2 C}{\kappa^o \kappa} . \tag{2.17}$$

From our model, the effective piezoelectric displacement, elastic stiffness, and the dielectric constant tensors may be combined in a meaningful way to yield this single, dimensionless value.

2.4.4.1 Biaxial texture with mosaic spread about ϕ and θ

Below are the results k_{31}, k_{33}, and k_{15} for biaxially textured films about θ and ϕ of both barium and lead titanate. We find that the results are independent of ϕ. The variation with FWHM θ is shown in Figure 2.13. The constants decrease monotonically and asymptote to zero. We see that once again the azimuthal symmetry of the piezoelectric displacement components results in no effect of in-plane texture. We recall that barium titanate showed an increase in d_{33} and d_{31} with texture about θ, but incorporating stiffness and the dielectric constant with texture for the k values, we do not see an enhancement in coupling factor for barium titanate, only a decrease.

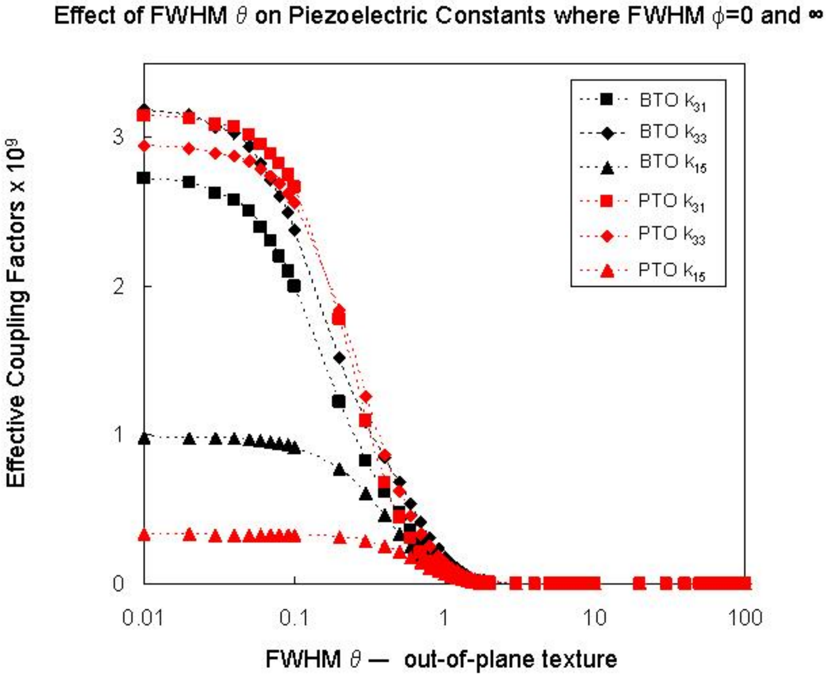

Figure 2.13: Variation of effective piezoelectric coupling factors k_{31}, k_{33}, and k_{15} with the FWHM of the out-of-plane texture distribution for textured barium titanate (BTO) and lead titanate (PTO) polycrystalline films (FWHM = 0 and ∞).

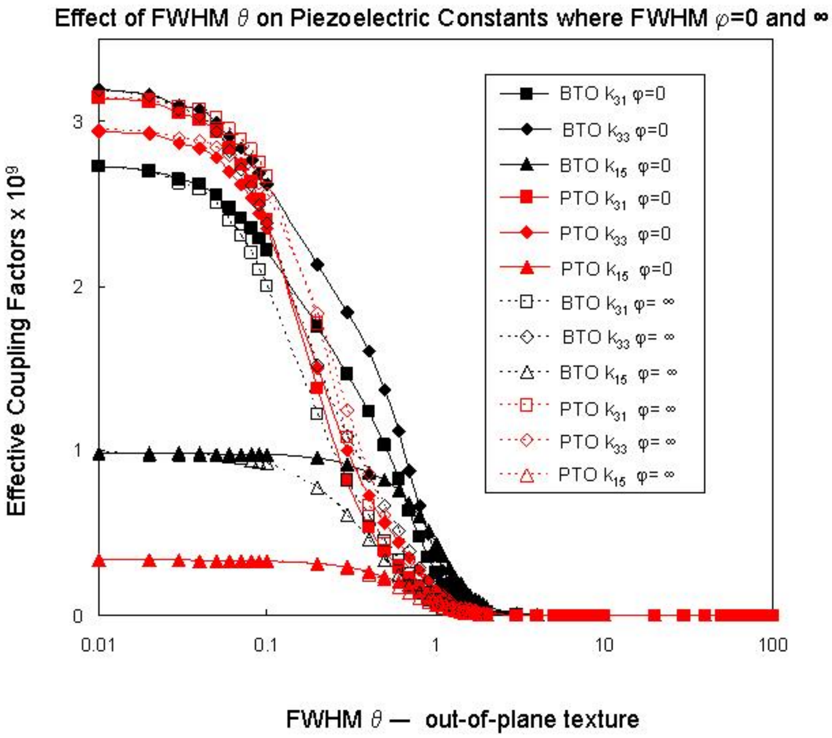

Figure 2.14: Variation of effective piezoelectric coupling factors k_{31}, k_{33}, and k_{15} with the FWHM of the out-of-plane texture distribution at FWHM of the twist distribution at 0 and ∞ for textured barium titanate (BTO) and lead titanate (PTO) polycrystalline films.

2.4.4.2 Biaxial texture with mosaic spread about ψ and θ

For biaxially textured film rotated about θ and ψ, we see slight dependence on FWHM ψ. Figure 2.14 shows envelopes of data at FWHM ψ=0 and FWHM $\psi = \infty$. A narrow distribution about perfect alignment does enhance the coupling factors for both materials in all 3 tensor values around FWHM θ in the range of 0.1 to 1. With a larger distribution, indicating a random texture of Euler angle ψ, we see the identical curves as in Figure 2.13, as expected. Even with the profound enhancement in d_{33} and d_{31} with an effective collection of grains with low twist angle ψ about each θ (Figure 2.5), the coupling factor follows a gradual decreasing trend.

2.5 Conclusion

A self-consistent approach was used to model effective electromechanical constants as a function of biaxial texture in polycrystalline films of barium and lead titanate. In-plane texturing has little effect on any of the electromechanical constants. Out-of-plane texturing increases the effective piezoelectric strain constants d_{31} and d_{33} for barium titanate, but not for lead titanate. With biaxial texturing out-of-plane and twisting about each angle, we see large enhancements in piezoelectric constants. The effective stiffness and dielectric constants for barium and lead titanate follow similar trends as the single crystal values of each material are similar. The effective stiffness constant C_{33} is the first noted electromechanical constant that shows a monotonic increase with increasing out-of-plane texturing for both materials. Finally, considering the effective piezoelectric coupling factor for these materials, we see a primary dependence on the out-of-plane texture.

Given the ultimate goal in researching thin film ferroelectric materials is the fabrication and optimization of devices, we must pay attention to the coupling factor results of this model, which incorporate all of the film's effective electromechanical constants. For a given sample geometry and electrode configuration, we would choose a given k component to give information about the device performance. For instance, k_{15} would be used to analyze a sample with interdigitated electrodes, and k_{33} or k_{31} for blanket electrodes, given a tent or cantilever geometry, respectively.

As seen above, biaxially textured films (about either set of angles) present no great advantage to fiber textured films when the coupling factor is used as a figure of merit. Thus devices fabricated with traditional growth methods for observation of the direct piezoelectric effect may be optimized by minimizing the texture about Euler angle θ, or out-of-plane distribution.

Chapter 3

Force-Displacement Testing of Thin Film Lead Titanate MEMS Bridges

3.1 Abstract

Surface micromachining is utilized to create MEMS bridges with $PbTiO_3$ as the active layer. Testing is performed with a custom apparatus wherein an individual device experiences an applied load via magnetostatic interaction and its displacement is recorded by a laser-beam bounce and a position-sensitive detector. Two major ferroelectric microstructures, polycrystalline and biaxially textured, are investigated. The textures are realized with templating and microstructurally characterized with various techniques. Normal and lateral cracking becomes a major problem in device testing. Force-displacement fitting allows some insight into initial stress and modulus of the composite beam device.

3.2 Introduction

The realization of free-standing ferroelectric thin film devices compatible with CMOS processing is a priority in achieving sophisticated microelectromechanical systems (MEMS). To release an active film from a silicon substrate with a back-etch technique requires the removal of hundreds of microns of the substrate as well as a suitable and robust mask for the device layer. A more flexible and process compatible technique is surface micromachining (Baborowski, 2004). Lithographic patterning allows several devices on a single chip. Another advantage is that devices could be separated on different regions of the chip or incorporated with additional technologies.

To advance the application of MEMS, it becomes necessary to increase the reliability of the component devices via an understanding of the mechanical behavior of the component materials (Spearing, 2000; Sharpe, 2001; Senturia, 2001). Standard methods for characterization have yet to be established. Work utilizing a XeF_2 vapor phase etch process to create free-standing ferroelectric MEMS structures has been shown for piezoelectric cantilevers (Zhang et al., 2003; Park et al., 2005), but work on bridges has lacked a suitable testing apparatus. This study presents a new technique for measuring the mechanical response of free-standing MEMS structures under load control.

3.3 Experimental

3.3.1 Fabrication

Surface micromachining of free-standing SiO_2 bridges is demonstrated. This is achieved by photolithographic patterning, an HF etch to remove the oxide in defined regions, and a chemical etch to remove the exposed Si. The electrode evaporations and ferroelectric film depositions occur after these structures have been defined.

3.3.1.1 Surface micromachining

SiO_2 PECVD films, 2 μm in thickness, on Si wafers were purchased. The SiO_2/Si samples are cleaned with acetone and methanol and exposed to vapors of HMDS for 25 seconds. PR 1813 is dropped onto the surface of the chip, that is spinning at 2000 RPM. The solution is spun for 25 seconds. The chip is soft baked at 90 °C for 1 minute. A transparency film, dark field and clear pattern, is affixed to a glass slide for use as a mask. In the mask aligner, the sample is exposed to UV light for 40 seconds. The pattern is developed by submerging the chip in MF 319 developer for 45 seconds, with agitation. It is then rinsed with DI water and dried and hard baked at 115 °C for 1 minute. A buffered HF etch is then used to remove the exposed oxide at a rate of 1 μm/11 minutes. Then the photoresist is removed with acetone and dried.

Xenon difluoride (XeF_2) etching was performed in collaboration with the Vahala group at Caltech. Because the etch is isotropic, the depth etched down into the Si is also etched laterally, and thus the a free-standing SiO_2 bridge may be released so long as the etch depth

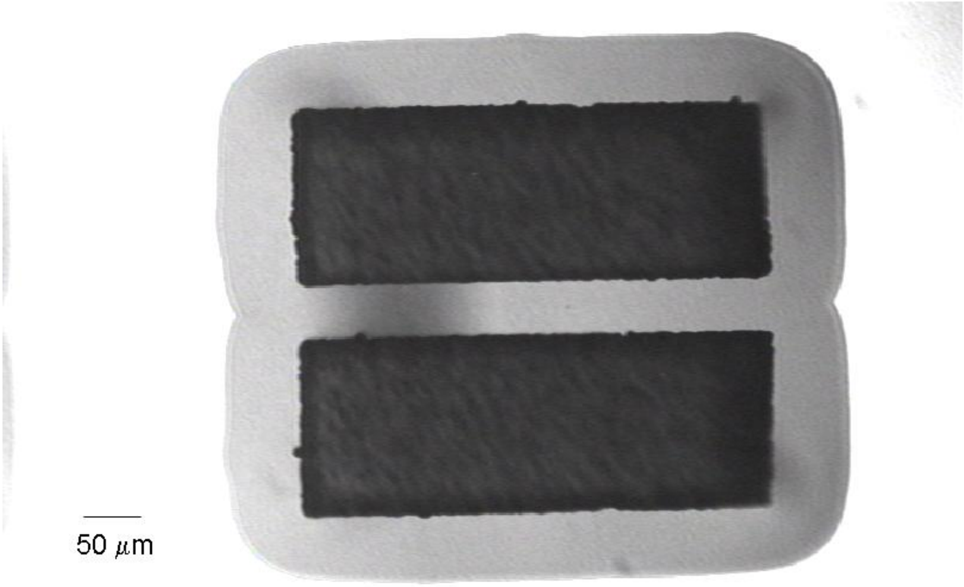

Figure 3.1: Optical micrograph of released SiO_2 bridge.

is at least half the width of the bridge. Also because the undercut occurs on all sides of the lithographically exposed rectangles, the structure is most like a membrane with rectangular holes defining a central 'bridge.' Figure 3.1 is an optical micrograph of a released bridge, where the undercut is visible from the image contrast.

3.3.1.2 Layer growth

Once the SiO_2 bridges have been released, any template layer, electrodes, and active layers are deposited, depending on the microstructure desired in the active film. The bottom electrodes used are traditional evaporated metal (Au) and a lattice-matched oxide electrode ($SrRuO_3$), as the two microstructures investigated in this chapter are polycrystalline films and biaxially textured films. IBAD MgO (see Chapter 2) thin film templates are deposited prior to the bottom electrode when biaxial texture is desired. Thus the passive layers of the bridge structure become either Au/SiO_2 (for a polycrystalline texture) or $SrRuO_3$/IBAD MgO/SiO_2 (for biaxial texture).

Lead titanate is grown by either MOCVD or PLD for the active material in these devices. MOCVD growth details were given in Chapter 1 and the substrate temperature was 650 °C. Completed bridge structures are robust and intact after deposition, as seen

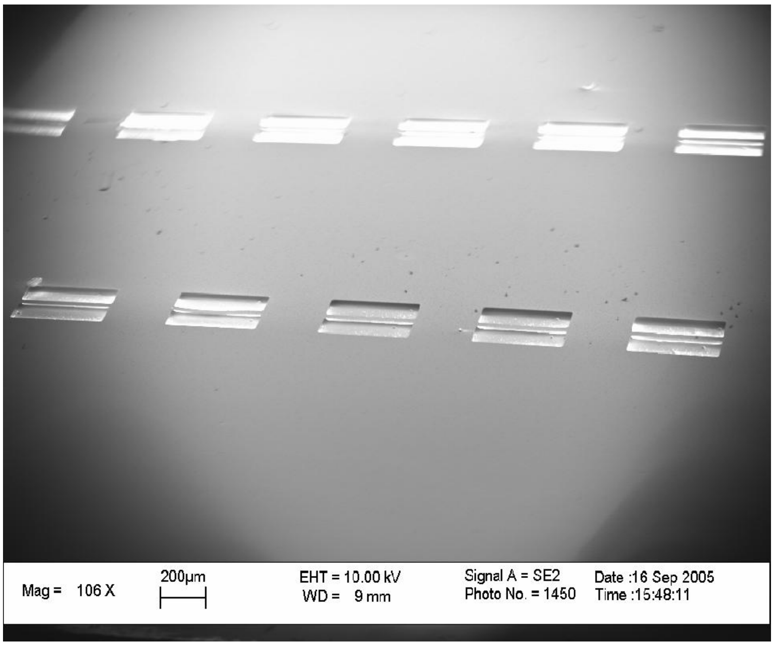

Figure 3.2: SEM image showing MOCVD $PbTiO_3/Au/SiO_2$ bridges.

in Figure 3.2. PLD growth conditions for $PbTiO_3$ were substrate temperature of 650 °C, O_2 pressure of 10 mTorr, turbo at 1000 Hz, and 18000 shots at 10Hz by a 350 mJ laser. The microstructures mentioned above were easily achieved. However, the island growth and coalescence kinetics of CVD proved less than desirable for a continuous film with the correct stoichiometry, as the Au/SiO_2 substrate exhibited inhomogeneities upon heating and $PbTiO_3$ growth (see Section 3.4.2.1). The PLD $PbTiO_3$ films exhibited correct texture and stoichiometry, but the well-known particle issues of the technique may have contributed to shorts in the structure (see section Section 3.4.3.1).

Top electrodes were either Pt or Au, deposited via sputtering or thermal evaporation, respectively.

3.3.2 Load-displacement apparatus

A non-contacting method using a laser beam and a position sensitive detector (PSD) are used to avoid the standard difficulties in the mechanical characterization methods for sensitive, fragile MEMS devices. The loading method developed for testing the thin film devices is an applied load via a magnetostatic interaction (Zhang, 2005). A schematic of the original experimental setup is shown in Figure 3.3 and a photograph of the modified setup for this

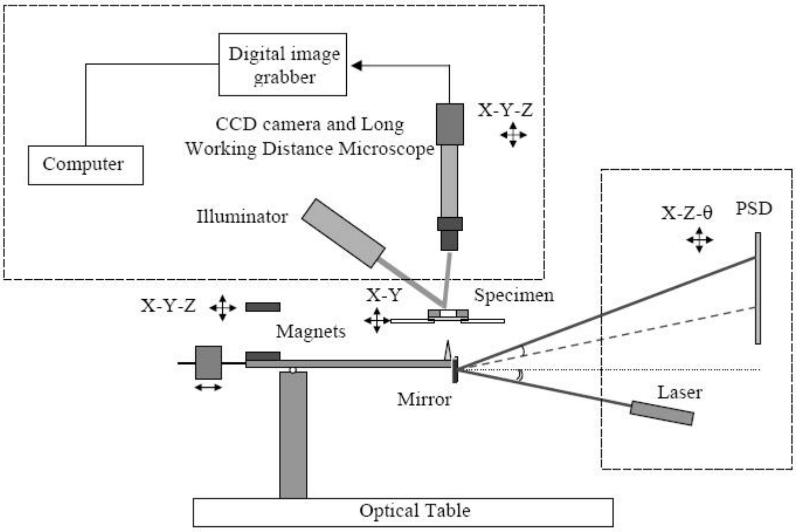

Figure 3.3: Schematic illustration of experimental setup.

application, to account for a device that is not transparent as in Zhang's thesis, but instead mounted upside down, is shown in Figure 3.4.

The load is applied by a tip, in this case a 90 μm wide knife-edge tip, that is attached to one end of a substantially rigid beam. The force applied to the sample is proportional to the magnetostatic force being applied to the other end of the rigid beam. This later force is controlled by changing the distance between a pair of permanent magnets; the lower magnet being attached to the beam and the upper affixed to an external post that is able to move vertically.

In order to enable dynamic experiments, the loading tip displacement, which is the same as the displacement of the sample at the contact point, is measured by monitoring the deflection of a single laser beam, which is reflected from a mirror attached to the end of the rigid beam. The reflected laser beam is sensed by a position-sensitive detector (PSD), which is attached to an external post, and the resulting voltage signal is recorded using an oscilloscope.

The sample is mounted on an X-Y-Z micro-stage and its alignment with respect to the tip is monitored by a long working distance optical microscope equipped with a CCD camera. This view is seen in Figure 3.5. The tip is brought into contact with magnetic controls. When tip vibration ceases, contact is established and the force and displacement are zeroed.

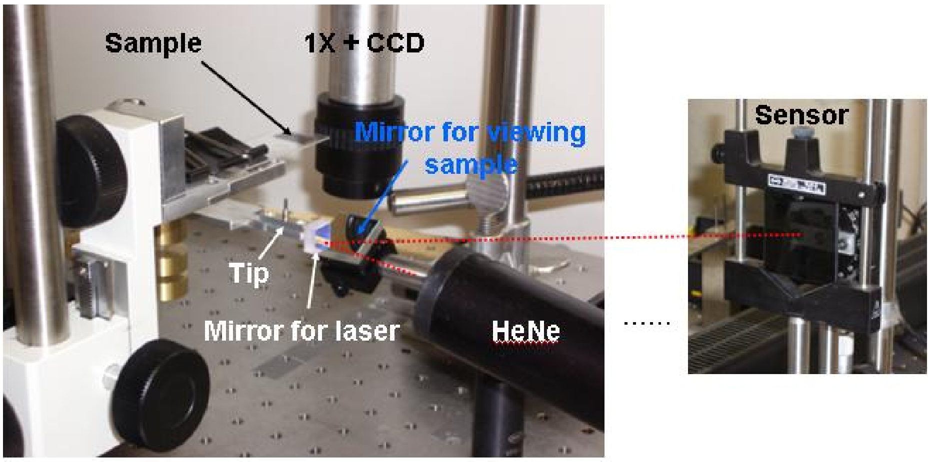

Figure 3.4: Setup modifications, including mirror and new CCD placement.

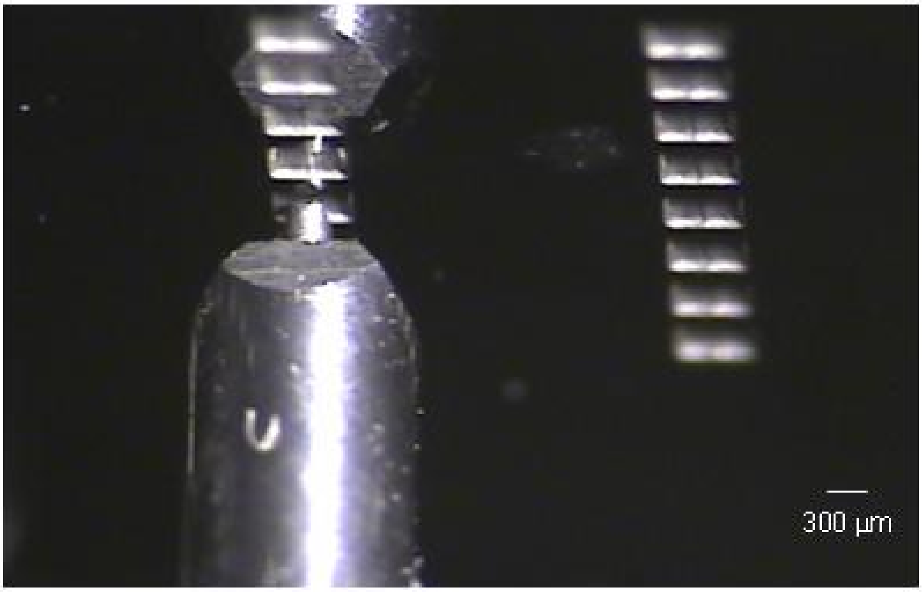

Figure 3.5: View of sample from CCD above mirror.

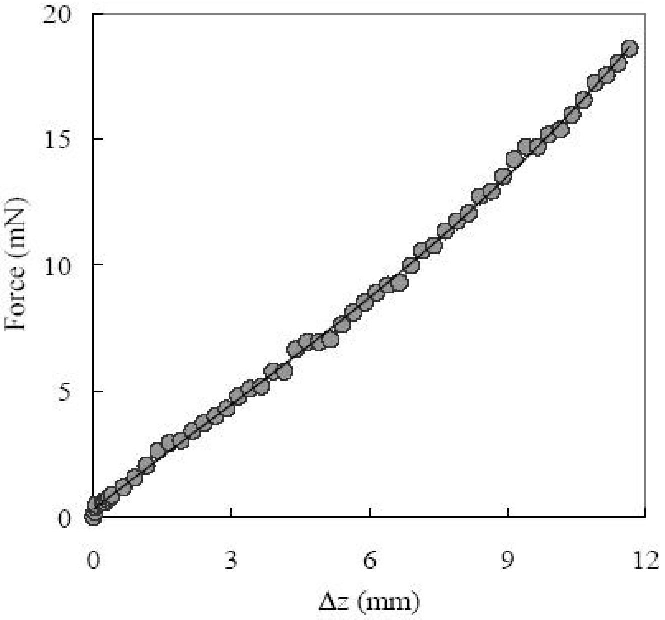

Figure 3.6: The applied force, F in mN, as a function of the change in the position (displacement) of the upper magnet, Δz in mm. This response curve was obtained by applying force on a load cell.

It should be noted that all the controlling and monitoring components: the upper magnet, the laser, the PSD, and the microscope, are isolated from the rigid beam. This fact significantly reduces the vibration and noise and protects the very fragile structures that are being tested (Zhang, 2005).

The force may be calibrated by placing a load cell in the sample location instead of the sample (but at the same height), as presented in Figure 3.6.

Thus the collected data are the calibrated force as the input variable, applied in increments in the z-direction position of the magnets, and the displacement as the response variable, measured as a voltage output on the oscilloscope monitoring the PSD.

3.3.2.1 Force-displacement fitting

Based on the force balances during the experiment where we are applying a force F and measuring a displacement d, as seen in Figure 3.7, we can see:

$$F = 2T \sin\theta \,, \tag{3.1}$$

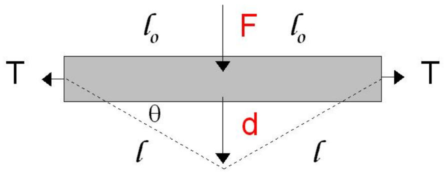

Figure 3.7: Free-body diagram of force-displacement experiment.

or that the tension T is

$$T = \frac{F}{2\sin\theta}\,. \tag{3.2}$$

Knowing that the tension is a superposition of forces, both from the initial stress and stress relationship via Hooke's law, we have:

$$T = T_o + EA\epsilon = \frac{F}{2\sin\theta}\,. \tag{3.3}$$

Now the strain, ϵ, may be written,

$$\epsilon = \frac{l - l_o}{l_o} = \frac{\frac{l_o}{\cos\theta} - l_o}{l_o} = \frac{1-\cos\theta}{\cos\theta}\,, \tag{3.4}$$

where the new length may be written as a trigonometric relationship.

This may be substituted into Equation (3.3):

$$T = \sigma_o A + EA\frac{1-\cos\theta}{\cos\theta} = \frac{F}{2\sin\theta}\,. \tag{3.5}$$

By using small angle approximations,

$$\cos\theta = 1 - \frac{\theta^2}{2}; \qquad \sin\theta = \theta; \qquad \theta = tan\theta = \frac{d}{l_o}\,, \tag{3.6}$$

and rearranging terms, we have the relationship between F and d:

$$F = \frac{2\sigma_o A}{l_o} d + \frac{EA}{l_o^3} d^3\,. \tag{3.7}$$

Thus using known parameters of half the length $l_o = 200\mu m$ and area $A = 100\mu m^2$ (width times thickness of SiO_2 film, because it dominates), we can fit the force-displacement data obtained from the experiments to determine the effective modulus, E, and initial stress, σ_o, for the composite beams and accordingly may study the performance of the device based on the properties of the composite films.

3.4 Results and Discussion

3.4.1 Controls

In order to best understand the effects of the active films on the mechanical performance of the devices, suitable controls were necessary. Thus plain as-etched SiO_2 bridges were tested, as well as SiO_2 bridges that were heated to 650 °C, the growth temperature for the lead titanate. Results for several bridges are shown in Figure 3.8. The heated samples were tested on a different day, thereby with a different calibration, and thus the forces used were not as high. The response of both the unheated and heated bridges is nearly identical. The bridges load and unload elastically with little to no hysteresis and inspection by optical microscope before and after testing shows no cracking or damage due to the cycling.

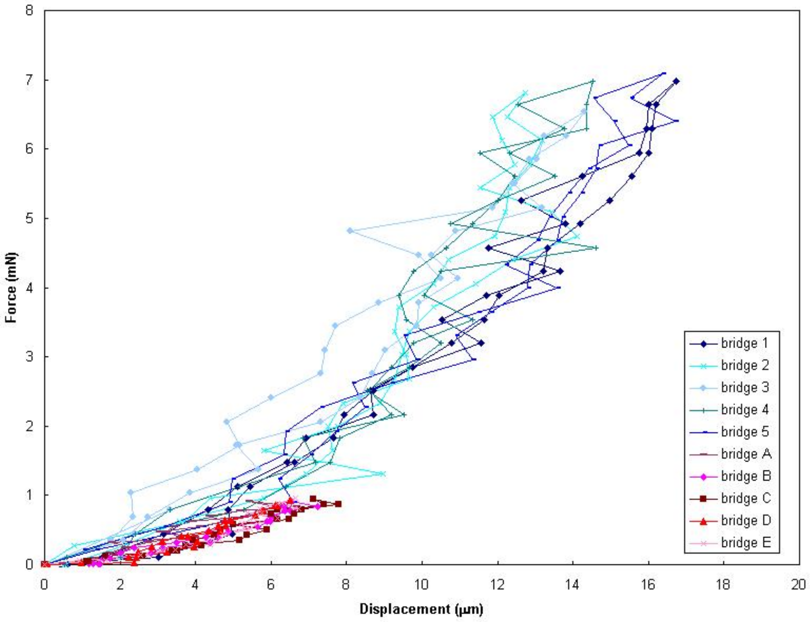

Figure 3.8: Force-displacement curves for SiO_2 bridges. Shades of blue indicate as-released SiO_2 while shades of red indicate SiO_2 bridges that have been heated to the growth temperature.

Considering the experimental data as scattered points, the initial stress and modulus for these controls is obtained by fitting to Equation (3.7) using least squares methods in a MATLAB 7.0 package. The fit is quite good, as seen in Figure 3.9, an example data set and fit.

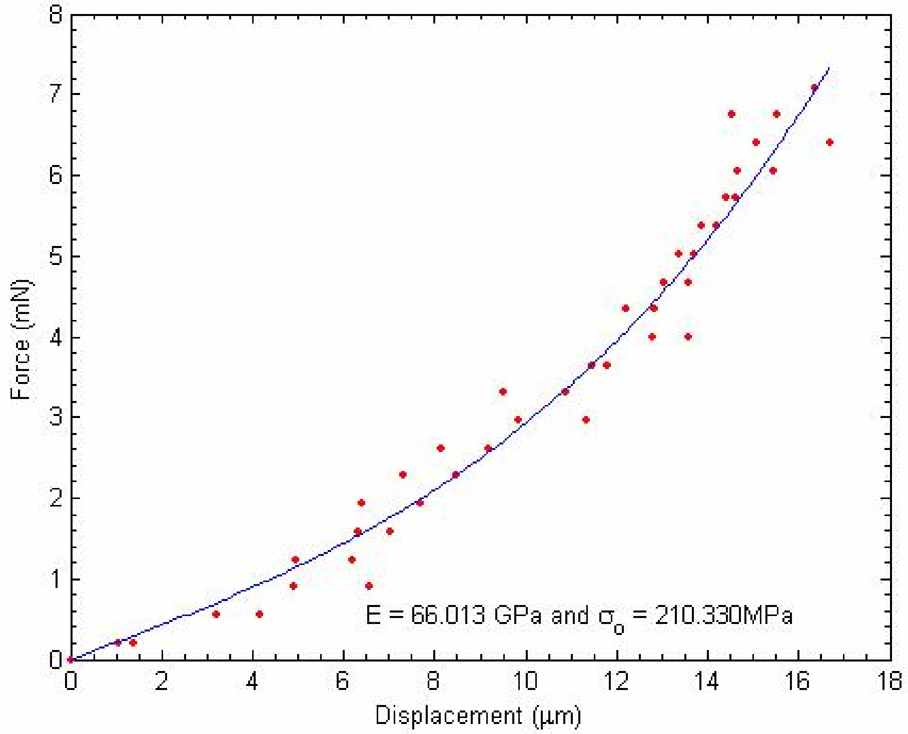

Figure 3.9: Fit determined by least squares.

We have values for SiO_2 bridges as released shown in Table 3.1. The average values are consistent with what is known for PECVD SiO_2 films. After heating, the results for modulus and initial stress in the SiO_2 bridges are shown in Table 3.2. The modulus increases slightly and the stress decreases. This makes physical sense as the material may be slightly hardened with heating, and stress may be recovered.

	bridge 1	bridge 2	bridge 3	bridge 4	bridge 5	AVG	STDEV
E (GPa)	55.90	122.09	51.79	90.54	66.01	77.27	29.23
σ_o (MPa)	217.10	191.67	332.73	235.25	210.33	237.41	55.52

Table 3.1: SiO_2 controls data from least squares fit.

	bridge A	bridge B	bridge C	bridge D	bridge E	AVG	STDEV
E (GPa)	25.91	104.56	82.24	176.03	182.41	114.23	65.93
σ_o (MPa)	127.41	65.40	65.41	60.02	41.51	71.95	32.52

Table 3.2: SiO_2 with heat controls data from least squares fit.

As layers are incorporated after patterning and release of the SiO_2 bridges, it is next suitable to test the cumulative layers. As Au is used as a bottom electrode, we also use Au/SiO_2 bridges as controls. (It should be noted at this point that there was a Cr adhesion layer used in between the Au and SiO_2, but because its thickness is around 1 nm, it is neglected from mechanical consideration as well as future nomenclature regarding the layer structure.) The force-displacement curves are shown in Figure 3.10.

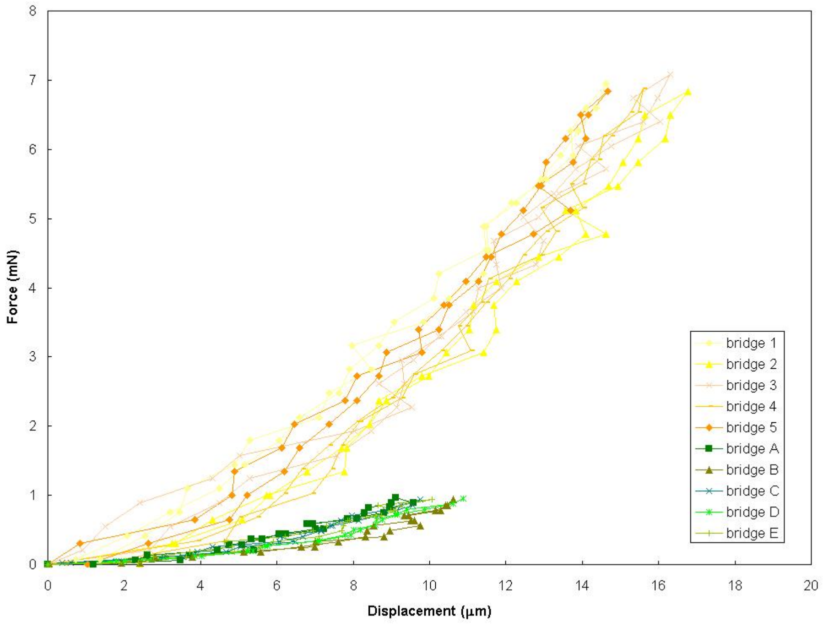

Figure 3.10: Force-displacement curves for Au/SiO_2 bridges. Shades of yellow indicate post-evaporation Au/SiO_2 while shades of green indicate Au/SiO_2 bridges that have been heated to the $PbTiO_3$ growth temperature.

The modulus and stress data for the Au/SiO_2 bridges immediately after Au evaporation are shown in Table 3.3. The average values are similar to the oxide controls. However after heating, the data for the Au/SiO_2 bridges, shown in Table 3.4, present some confusion. The initial stress is decreased by an order of magnitude upon heating, which could be explained by stress recovery with temperature. However, the modulus also decreases. Thus, an expanded study of the mechanics was necessary.

	bridge 1	bridge 2	bridge 3	bridge 4	bridge 5	AVG	STDEV
E (GPa)	71.40	67.69	64.80	96.79	92.32	78.60	14.84
σ_o (MPa)	283.08	185.04	231.65	157.38	221.55	215.74	47.88

Table 3.3: Au/SiO$_2$ controls data from least squares fit.

	bridge A	bridge B	bridge C	bridge D	bridge E	AVG	STDEV
E (GPa)	55.03	50.29	51.92	43.33	51.53	50.42	4.33
σ_o (MPa)	40.02	11.23	35.54	26.82	35.11	29.74	11.39

Table 3.4: Au/SiO$_2$ with heat controls data from least squares fit.

Equation (3.7) assumes that the beam is only stretched, so the analysis was reevaluated with the incorporation of bending and shear terms given a fixed supported beam (Jing et al., 2006). The expression for bending force is

$$F_{bending} = \frac{24EId}{l_o^3} \, , \tag{3.8}$$

where $I = \frac{tw^3}{12}$ is the moment of inertia, a function of thickness and width, based on beam geometry. The shear force is

$$F_{shear} = \frac{2\mu Ad}{l_o} \, , \tag{3.9}$$

where μ, the shear modulus, is Young's modulus divided by $2(1+\nu)$, where ν is Poisson's ratio, usually approximated at 0.2.

As the displacement resulting from these three forces is in the same vector direction, by nature of the experiment, the displacements can be added. Thus Equation (3.7) is rewritten in d as the cube root,

$$\begin{aligned} d_{total} = {} & \frac{l_o}{6(EA)^{\frac{1}{3}}}(108F + 12\sqrt{3}\sqrt{\tfrac{32\sigma^3A^2+27F^2E}{E}})^{\frac{1}{3}} \\ & -4\sigma Al_o(108F + 12\sqrt{3}\sqrt{\tfrac{32\sigma^3A^2+27F^2E}{E}})E^2A^{2^{\frac{-1}{3}}} \, , \end{aligned} \tag{3.10}$$

and the new F-d fitting equation is:

$$d_{total} = d_{bending} + d_{shear} + d_{stretch} \ , \tag{3.11}$$

$$\begin{aligned} d_{total} = \tfrac{Fl_o^3}{2Etw^3} + \tfrac{l_o}{6(EA)^{\frac{1}{3}}}(108F + 12\sqrt{3}\sqrt{\tfrac{32\sigma^3 A^2 + 27F^2 E}{E}})^{\frac{1}{3}} \\ -4\sigma A l_o(108F + 12\sqrt{3}\sqrt{\tfrac{32\sigma^3 A^2 + 27F^2 E}{E}}) E^2 A^{2^{\frac{-1}{3}}} \ . \end{aligned} \tag{3.12}$$

	bridge A	bridge B	bridge C	bridge D	bridge E	AVG	STDEV
E (GPa)	83.81	51.52	64.31	54.27	75.33	65.85	13.73
σ_o (MPa)	24.83	14.36	30.46	20.90	22.16	22.54	5.87

Table 3.5: Au/SiO$_2$ with heat controls data from least squares fit of Equation (3.12).

The least squares fitting method is repeated on the samples shown in Table 3.4, with the new results shown in Table 3.5. Since the general trend is still a decrease in modulus, we abandon Equation (3.12) in favor of the original fit equation, Equation (3.7). The new fit most likely cannot account for additional phenomena that may not be explained with mechanical modifications to the force-displacement expression, such as crystallization of the evaporated Au.

The final control structure discussed in this section is that of IBAD MgO/SiO$_2$. This interface will be the first occurrence of an oxide film being incorporated after the patterning and release of the SiO$_2$ bridges. The force-displacement data are shown in Figure 3.11. No heated control is necessary because the IBAD process necessitates elevated temperatures.

	bridge 1	bridge 2	bridge 3	AVG	STDEV
E (GPa)	92.30	124.73	62.44	93.16	31.15
σ_o (MPa)	152.14	98.18	149.48	133.27	30.42

Table 3.6: IBAD/SiO$_2$ controls data from least squares fit.

If we use the data from Table 3.6, we can surmise the contribution from the IBAD layer. The IBAD and SiO$_2$ films' modulus act as parallel springs on the composite beam, and therefore:

$$E_{measured} = \frac{t_{SiO_2} + t_{IBAD}}{\frac{t_{SiO_2}}{E_{SiO_2}} + \frac{t_{IBAD}}{E_{IBAD}}} \ . \tag{3.13}$$

We can resolve the modulus of each layer in the stack using the average composite modulus

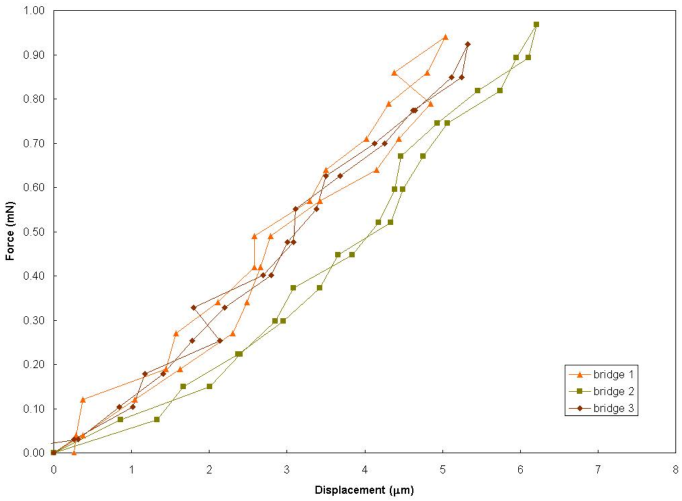

Figure 3.11: Force-displacement curves for IBAD MgO/SiO_2 bridges.

in Table 3.6 and the average heated SiO_2 modulus from Table 3.2. Assuming 50 nm thick IBAD MgO, 2 μm thick IBAD/SiO_2, the IBAD modulus alone is 11.10 GPa. This value seems quite small and inaccurate, but considering the data were taken at such low forces, the curve is very much linear, and as the modulus is within the coefficient of the cubic term, this is understandable.

Finally, the combined individual stresses may not be resolved because the films may interact in a way such that we cannot isolate the effects. All that can be said is that after IBAD MgO deposition, the composite beam has a higher initial stress than with SiO_2 alone.

3.4.2 CVD $PbTiO_3$/Au/SiO_2 bridges

3.4.2.1 Microstructural characterization

The $PbTiO_3$ deposition method for the polycrystalline microstructure was MOCVD. Patterned, free-standing SiO_2 bridges with Au bottom electrodes were introduced into the CVD reactor. During growth the sample was heated to 650 ^{o}C, thus causing some crystallization of the Au film. With no underlying texture, the film was expected to not inherit any orientation from the substrate. XRD analysis, shown in Figure 3.12, confirms that the film is polycrystalline.

Cathodoluminescence (CL) spectroscopy was performed to determine if the individual grain orientations could be imaged. As the technique is performed in the SEM, sample to-

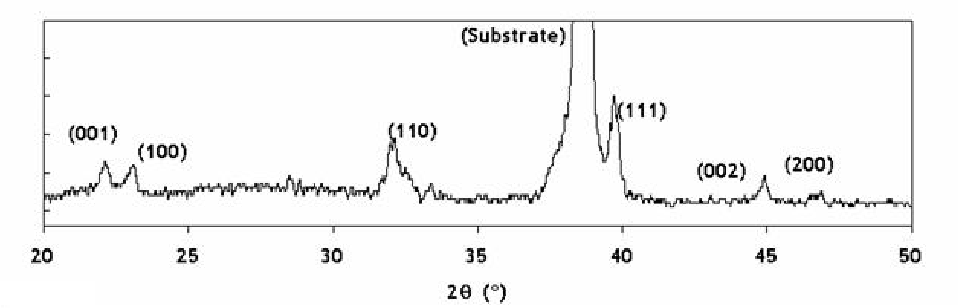

Figure 3.12: XRD of $PbTiO_3/Au/SiO_2/Si$ film.

pography information is simultaneously obtained. The CL image is a map of light collected from the entire sample while the e-beam dwells at the particular spot on the image. Results are shown in Figure 3.13. The SEM/CL set of images reveals that the microstructure of the film has pockets of active (white or grey) regions and suppressed (dark) regions. The active regions appear to have grain structure whereas the darker islands have a smooth, amorphous appearance. EDS analysis reveals these islands are a lead-rich phase of lead titanate. The granular cluster regions have the correct stoichiometry. Thus during CVD growth, nucleation sites develop on the Au film that are either advantageous or disadvantageous to the development of correct stoichiometry. For instance, it has been shown that Au/MgO substrates develop small holes in the Au during the heating to growth temperature of $PbTiO_3$ (Gao et al., 1993). In their case it was advantageous to have holes as nucleation pathways to the MgO substrate, but in this case, the SiO_2 substrate may instead be a pathway for

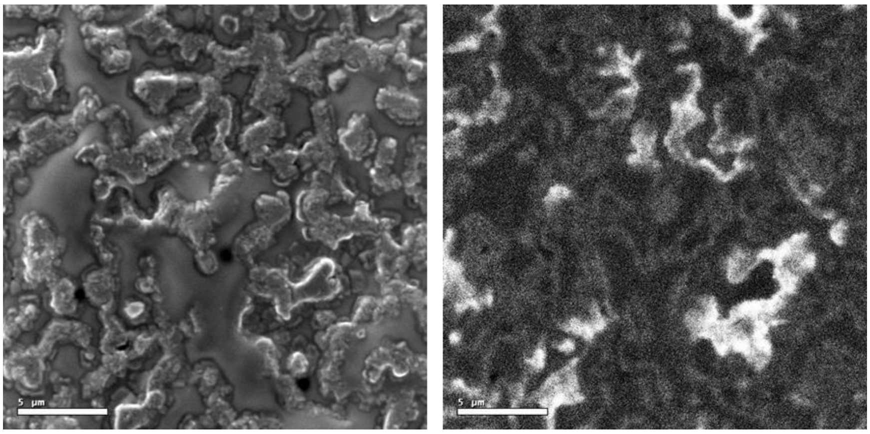

Figure 3.13: Left: SEM, Right: CL of $PbTiO_3/Au/SiO_2$ stack.

Au diffusion and interference with $PbTiO_3$ deposition.

Electron back-scattered diffraction (EBSD) was performed as a means of orientation imaging. The sample was tilted at 70^o from the e-beam, and electron penetration Monte Carlo simulations (CASINO) (Figure 3.15) of a 250 nm $PbTiO_3$ / 150 nm Au / 2 μm SiO_2 / Si substrate sample for a 20 keV beam confirm that this enables a surface-sensitive technique.

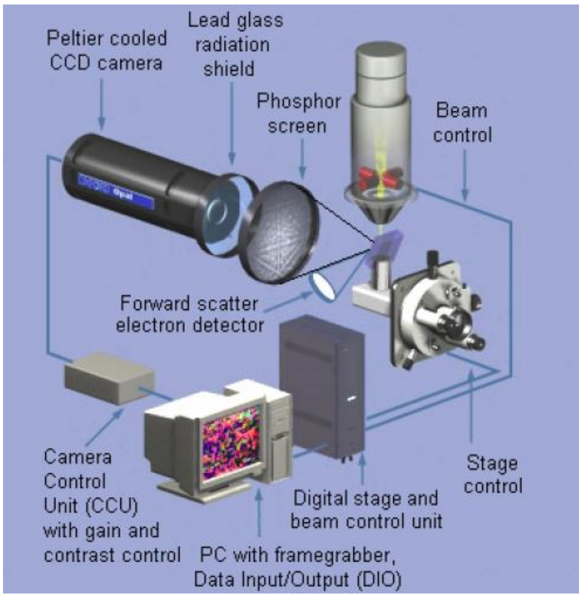

Figure 3.14: EBSD schematic.

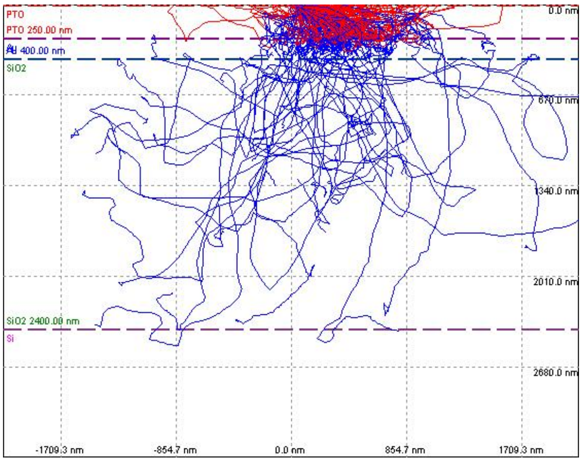

Figure 3.15: Electron penetration simulation. Red trajectories indicate diffracted electrons. Most diffracted electrons are from top layer and therefore the EBSD technique is sufficiently surface sensitive.

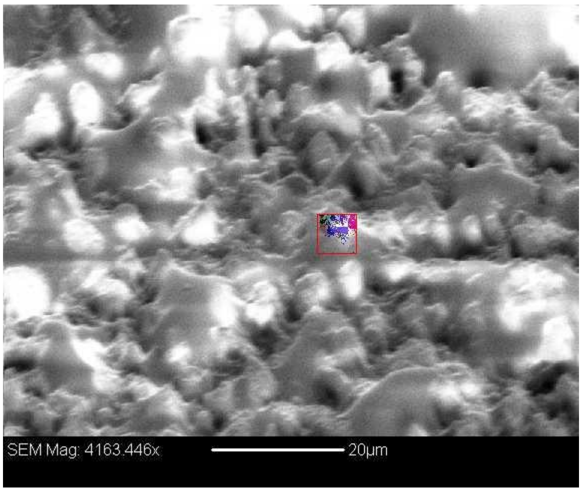

Figure 3.16: SEM image with overlaid EBSD mapping technique, where colors correspond to triplet of Euler angles.

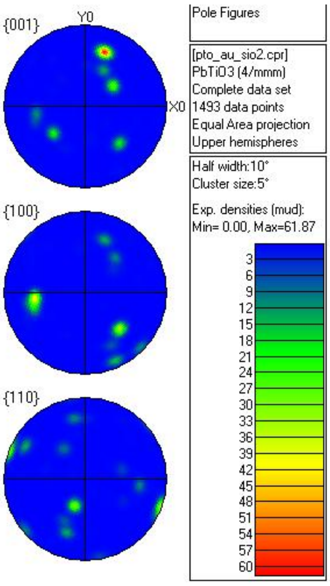

Figure 3.17: Pole figure for $PbTiO_3/Au/SiO_2$ film.

Figure 3.16 shows an SEM image with an overlaid orientation map, where each color corresponds to a particular triplet of Euler angles, thus defining the orientation at that pixel. There is an excellent correspondence between the colored regions and the grain size of the film. This collection of orientations can be mapped onto a pole figure, shown in Figure 3.17. There is no primary pole direction where the orientations cluster, thus further confirming the random nature of the polycrystalline film.

3.4.2.2 Force-displacement results

The polycrystalline $PbTiO_3/Au/SiO_2$ bridges were tested for their performance under load with results shown in Figure 3.18. The force-displacement results are classified as three types: type A, showing a hardening and elastic loading/unloading, type B, showing a linear regime followed by a large jump in displacement and finally a loading/unloading at some high displacement, and type C, which is a type B bridge unloaded before the jump in displacement.

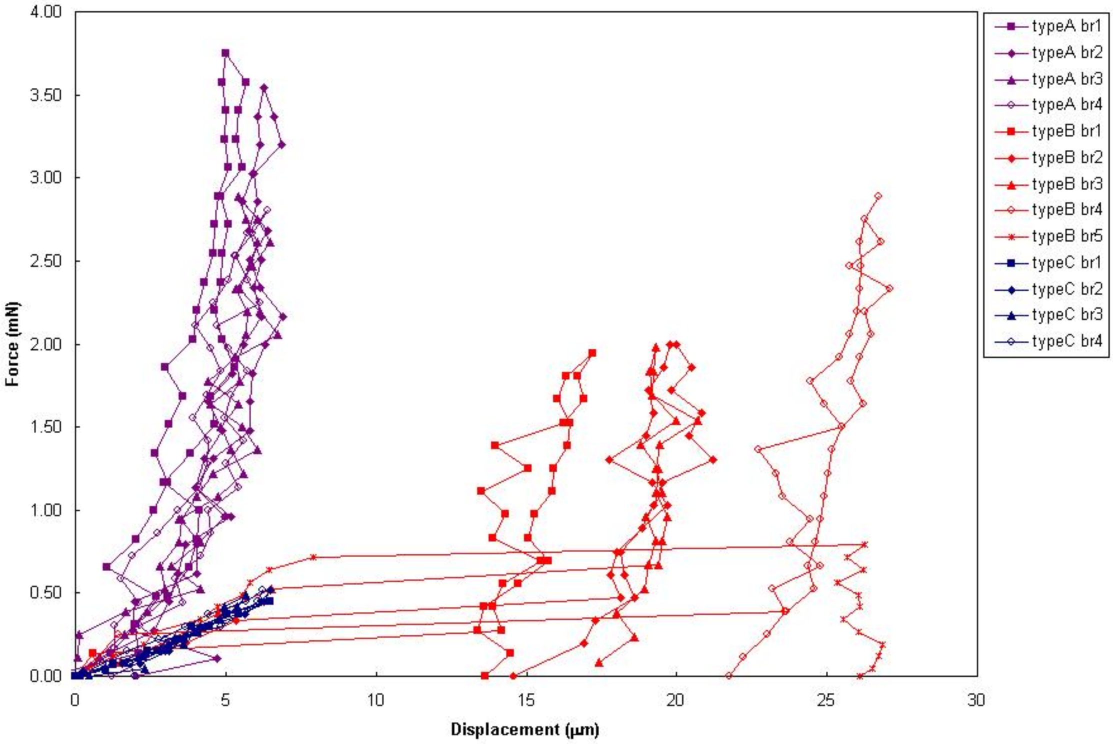

Figure 3.18: Force-displacement curves for $PbTiO_3/Au/SiO_2$ bridges.

The three types of bridge performance may be understood upon inspection of each classification in optical microscopy images taken after testing. Type A bridges remain intact, but cracking is evident in the span, as seen in Figure 3.19. The crack developed at some force, but became arrested and thus the bridge loaded and unloaded elastically, exhibiting stiffening as compared with the controls, as seen in Figure 3.20. This is the expected behavior, as more force becomes necessary to generate the same displacements as a beam with one less layer. Least squares fits of the type A bridges are shown in Table 3.7.

These data are most representative of the mechanical performance of the composite beam with the active $PbTiO_3$ top layer.

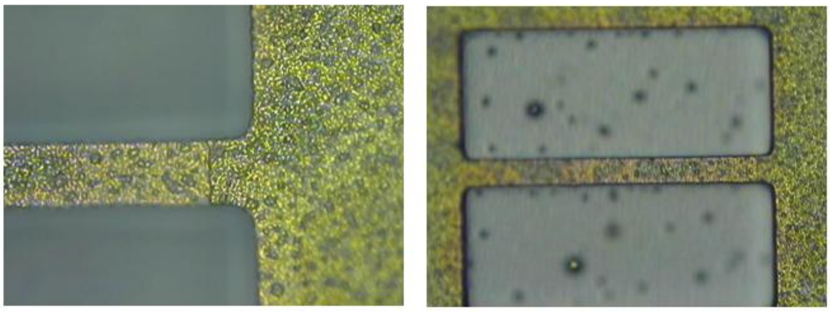

Figure 3.19: Typical OM images for type A bridges after testing, exhibiting arrested cracks. Left: 50X, Right: 20X

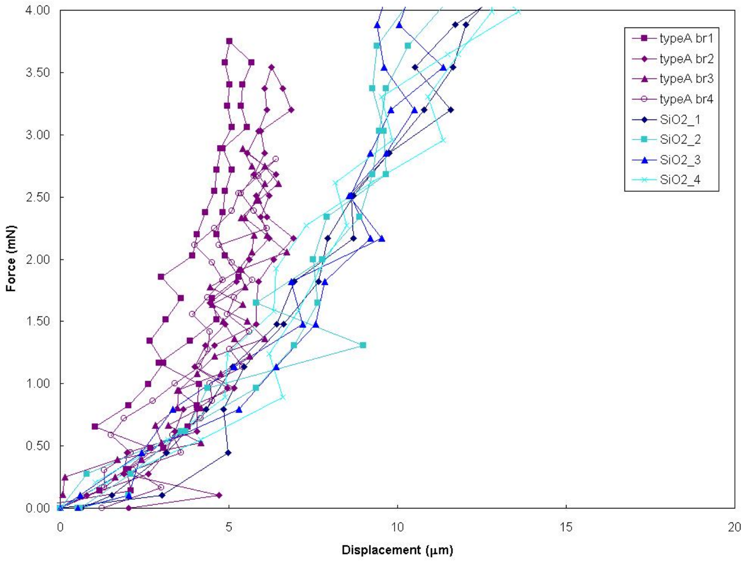

Figure 3.20: F-d $PbTiO_3/SrRuO_3$/IBAD/SiO_2 type A bridges and some SiO_2 control bridges.

	bridge 1	bridge 2	bridge 3	bridge 4	AVG	STDEV
E (GPa)	1037.90	650.81	389.81	428.92	626.86	297.15
σ_o (MPa)	224.53	104.28	197.77	217.04	185.91	55.57

Table 3.7: $PbTiO_3/Au/SiO_2$ type A bridges: results from least squares fit.

Type B bridges also show cracking after testing when viewed in the optical microscope, but to a different extent than type A bridges. Figure 3.21 shows typical bridges that, after loading, have cracked and disconnected from the substrate. The cracks either occur at the weak end or in the span, but in both cases the bridge is no longer supported. Thus the large jump in displacement as seen in Figure 3.18 must be attributed to the release of the bridge from this support. Nevertheless, after the crack has propagated, the bridge behaves more like the type A classification, with a stiffening vs. the control bridges and elastic loading and unloading.

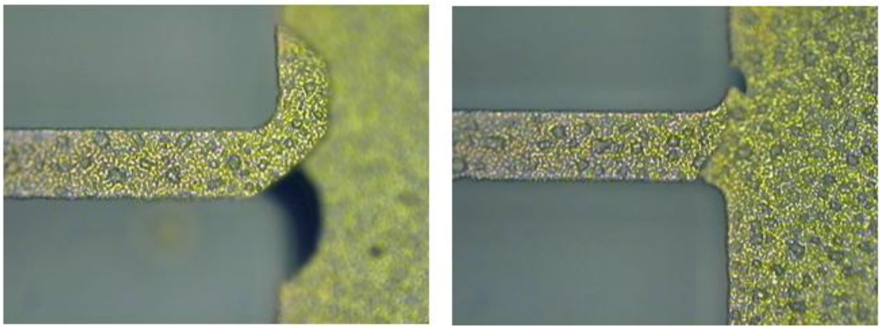

Figure 3.21: Typical 50X OM images for Type B bridges after testing, exhibiting complete cracks.

Type C bridges are merely type B bridges that have been unloaded before the critical applied force which causes the jump in displacement. These bridges load and unload elastically, but are much softer than those of type A. When type C bridges are studied after testing, as seen in Figure 3.22, cracks are only visible under very high magnification. Type C bridges may also be fit according to beam stretch theory via least squares methods, and the values for modulus and initial stress are shown in Table 3.8. These bridges are not only softer than the type A bridges, but they also exhibit lower moduli than the Au/SiO_2 controls, indicating that the specific crack formation that will ultimately lead to a catastrophic

	bridge 1	bridge 2	bridge 3	bridge 4	AVG	STDEV
E (GPa)	16.09	43.6	114.93	38.11	53.18	42.85
σ_o (MPa)	63.04	53.77	40.08	60.71	54.40	10.33

Table 3.8: $PbTiO_3$/Au/SiO_2 type C bridges: results from least squares fit.

freeing of the bridge significantly softens the composite beam.

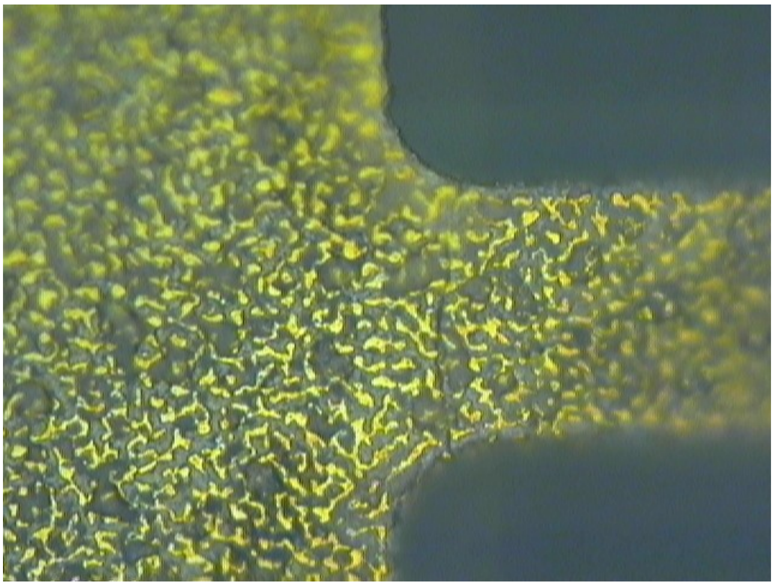

Figure 3.22: Typical 100X OM image for type C bridges after testing, depicting crack formation at most early stage.

Whether a bridge performs as type A or B is a result of defects in the surface, which may propagate or arrest the cracks as they nucleate.

After the load testing on the $PbTiO_3/Au/SiO_2$ bridges was completed, 50 nm of sputtered Pt was blanket deposited on the chip so that the devices could be tested electromechanically. Figure 3.23 shows force-displacement results for a $Pt/PbTiO_3/Au/SiO_2$ bridge tested normally as well as a second bridge that was loaded to a certain force, then experienced a $0 \rightarrow 13.5V \rightarrow 0$ cycle, and then was unloaded. While bridge 1 shows little hysteresis, the bridge that experiences the electric field shows pronounced hysteresis, indicating that the film is rearranging and straining under the applied field and thus the performance of the bridge with unloading of force is not identical to the loading case.

The effect of voltage on bridge displacement is seen in Figure 3.24. With the application of voltage, the sample moves to a less-displaced state (or flatter configuration) due to the field encouraging domains to reorient along the direction of the field. Therefore the bridge becomes more flat as the ferroelectric layer prefers a shorter configuration. Removing the voltage reduces this saturated state to some remnant displacement. Finally, when the sample is then unloaded, it recovers the new, lower displacement.

Cracks were not seen in $Pt/PbTiO_3/Au/SiO_2$ bridges, although it is not clear whether

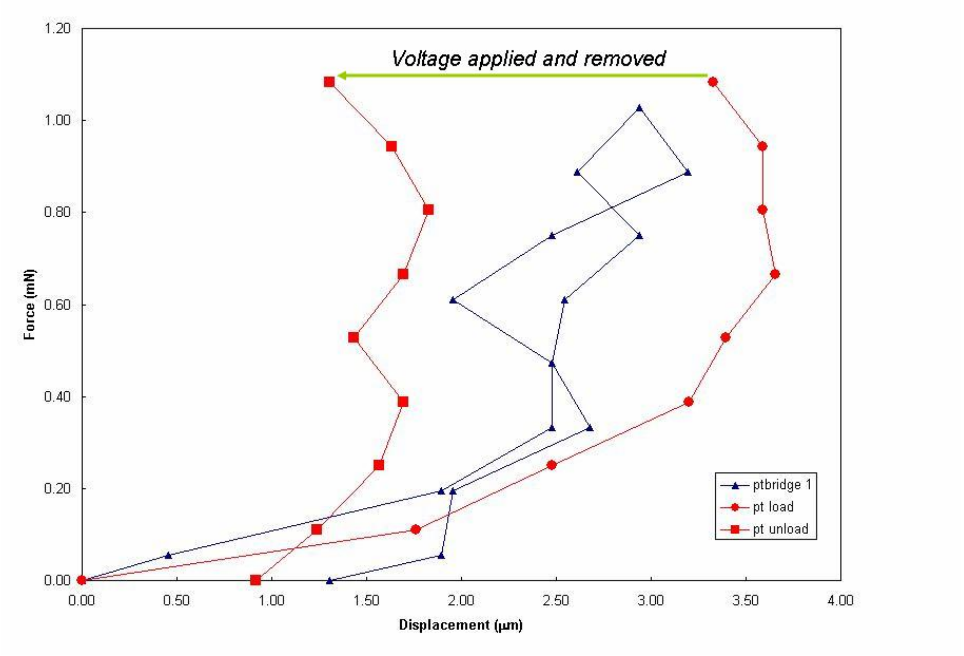

Figure 3.23: F-d results for typical Pt/$PbTiO_3$/Au/SiO_2 bridge and one with voltage at some applied force and unload.

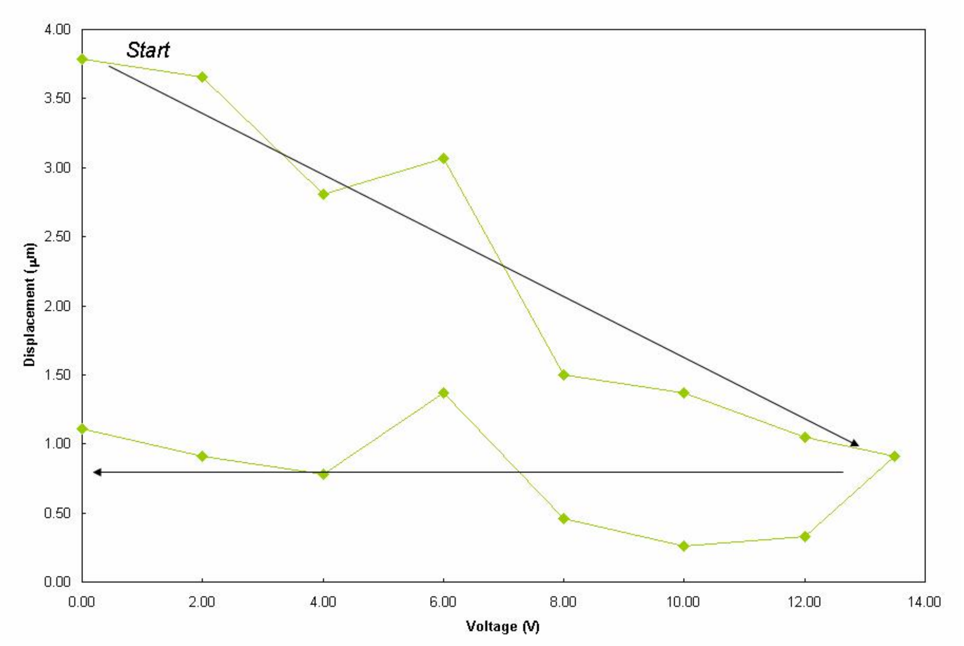

Figure 3.24: Effect of voltage on sample held at nonzero force. Arrows are used as guides to the eye.

they were simply difficult to image because of film roughness or because the cracks (if present) did not propagate through the topmost layer.

3.4.3 PLD $PbTiO_3/SrRuO_3$/IBAD MgO/SiO_2 bridges

3.4.3.1 Microstructural characterization

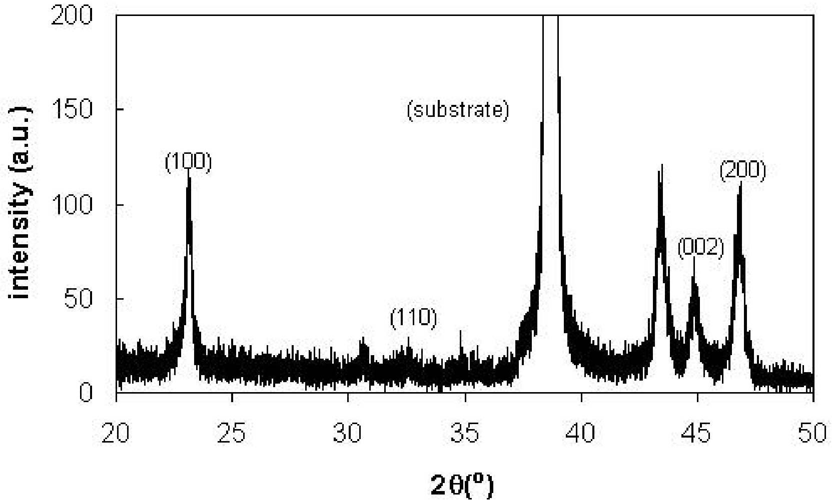

Figure 3.25: XRD of $PbTiO_3/SrRuO_3$/IBAD $MgO/SiO_2/Si$ film. Only $PbTiO_3$ peaks are indexed.

The $PbTiO_3/SrRuO_3$/IBAD MgO/SiO_2 structures utilized PLD deposition for both the $PbTiO_3$ and $SrRuO_3$, and an e-beam evaporation with an ion-beam source for IBAD MgO film. We have a biaxially textured microstructure because the perovskite $PbTiO_3$ and $SrRuO_3$ films inherit the texture of the MgO template. This is confirmed with XRD analysis, shown in Figure 3.25. The prominent orientation is a-axis $PbTiO_3$.

Upon inspection with SEM (Figure 3.26), the film unfortunately exhibits pinholes. Thus during growth the surface did not develop evenly. To confirm that the hole, shown in Figure 3.27, is in fact a non-continuous spot, EDS analysis was performed with spectra sampled inside and outside of the hole. These spectra are shown in Figure 3.28. Spectrum 2 shows a lack of signal in Pb, Ti, and Mg, thus indicating a lack of agreement with the proper elemental spectra of spectrum 1, taken on the surface just outside the hole.

EBSD analysis was performed on a pinhole-free region. Figure 3.29 shows a high mag-

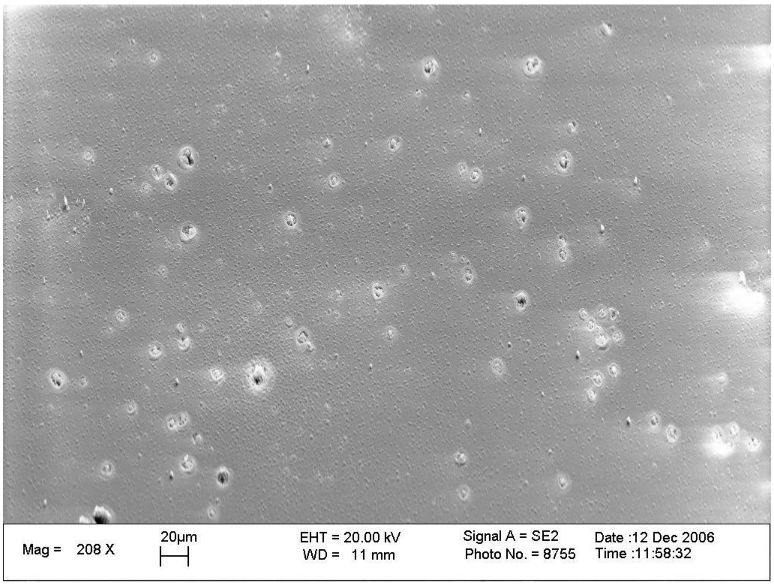

Figure 3.26: SEM image of $PbTiO_3/SrRuO_3/IBAD/SiO_2$ showing pinholes.

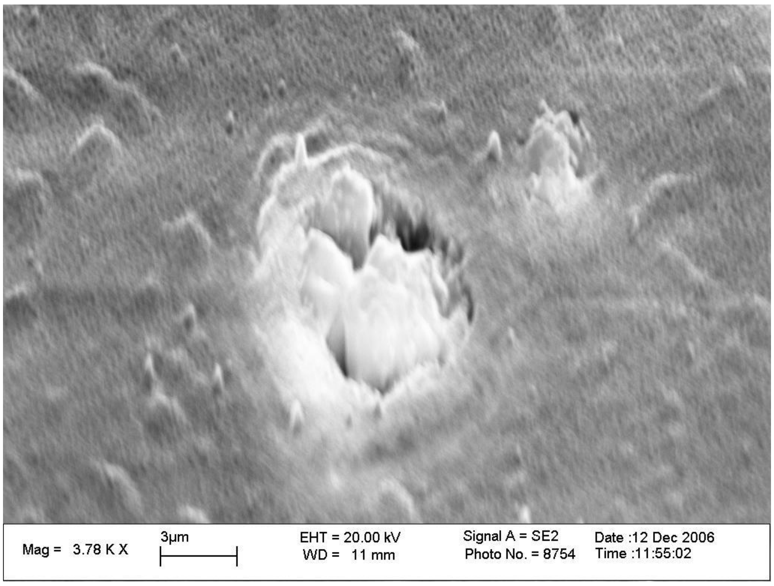

Figure 3.27: SEM image of $PbTiO_3/SrRuO_3/IBAD/SiO_2$ pinhole.

nification SEM image with the orientation mapping overlay. Some grain-scale orientation is evident. These data are plotted on a pole figure, shown in Figure 3.30. The pole plots clearly indicate biaxial texture, as both the 001 and 100 poles have 4-fold symmetry and a central pole.

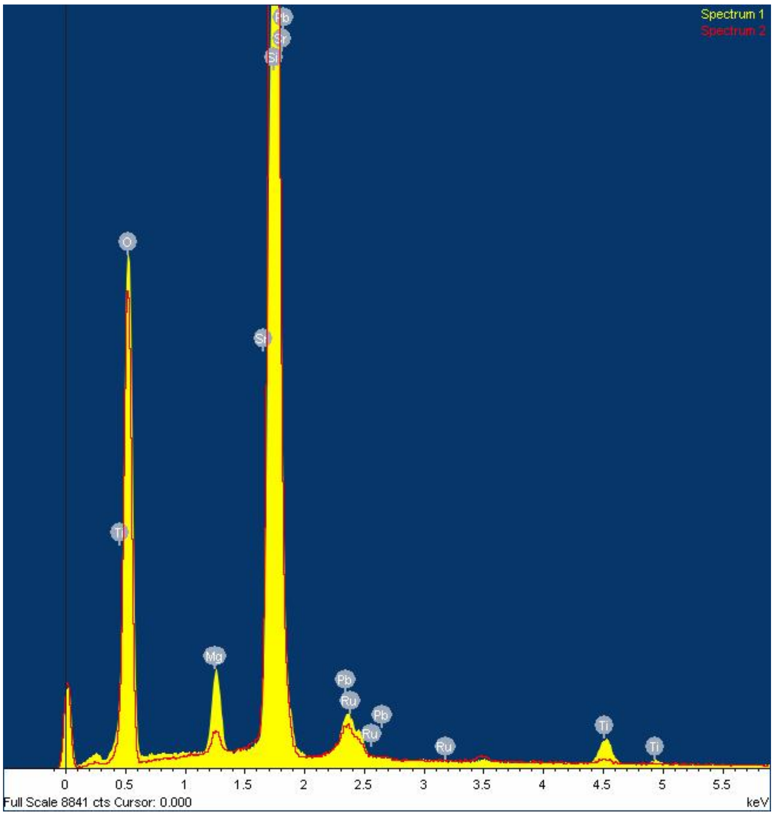

Figure 3.28: Spectrum 1 is outside pinhole, spectrum 2 is inside pinhole.

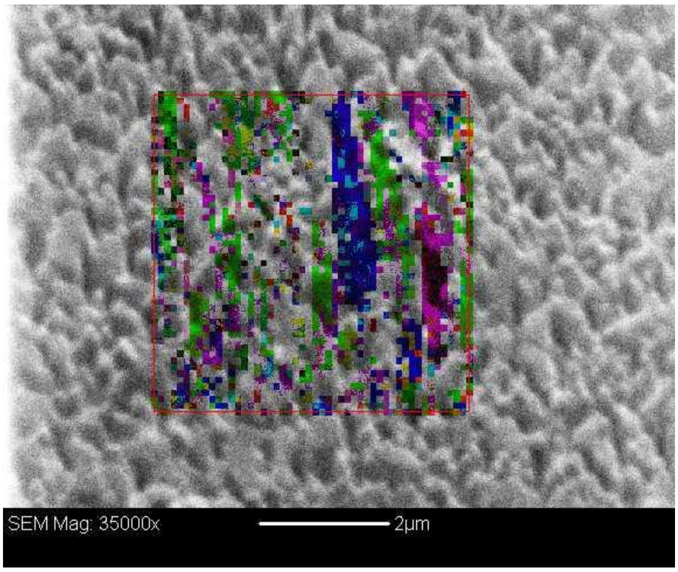

Figure 3.29: High magnification SEM image of $PbTiO_3/SrRuO_3$/IBAD/SiO_2 with EBSD overlay.

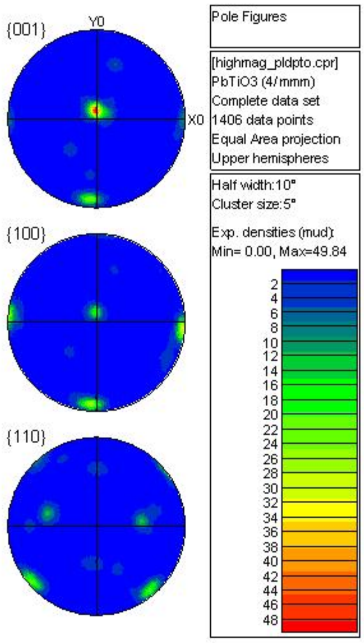

Figure 3.30: Pole figure for $PbTiO_3/SrRuO_3$/IBAD/SiO_2 film.

3.4.3.2 Force-displacement results

Force-displacement testing results from the $PbTiO_3/SrRuO_3$/IBAD/SiO_2 bridges are shown in Figure 3.31. The bridges show elastic loading and unloading. To prevent cracking, the samples were tested at very low forces. The data were fit for effective modulus and initial stress, as seen in Table 3.9. Because these bridges show a softening in modulus as compared with the IBAD MgO/SiO_2 control bridges, it is expected that there is some unknown shear force within the layers of the sample, perhaps causing delamination or lateral cracking.

	bridge 1	bridge 2	bridge 3	AVG	STDEV
E (GPa)	64.79	81.71	82.57	76.35	10.03
σ_o (MPa)	66.24	50.94	50.15	55.78	9.07

Table 3.9: $PbTiO_3/SrRuO_3$/IBAD/SiO_2 results from least squares fit.

Electromechanical switching on these bridges was unsuccessful, either due to poor electrical contacts or because of the pinholes. A 150 nm Au film (with a Cr adhesion layer) is evaporated for a top contact. As expected, a current was produced with the application of voltage, and a resistance of 700 ohms was measured. This resistance is most likely the resistance of the $SrRuO_3$ bottom contact, but a handheld multimeter also indicated a low re-

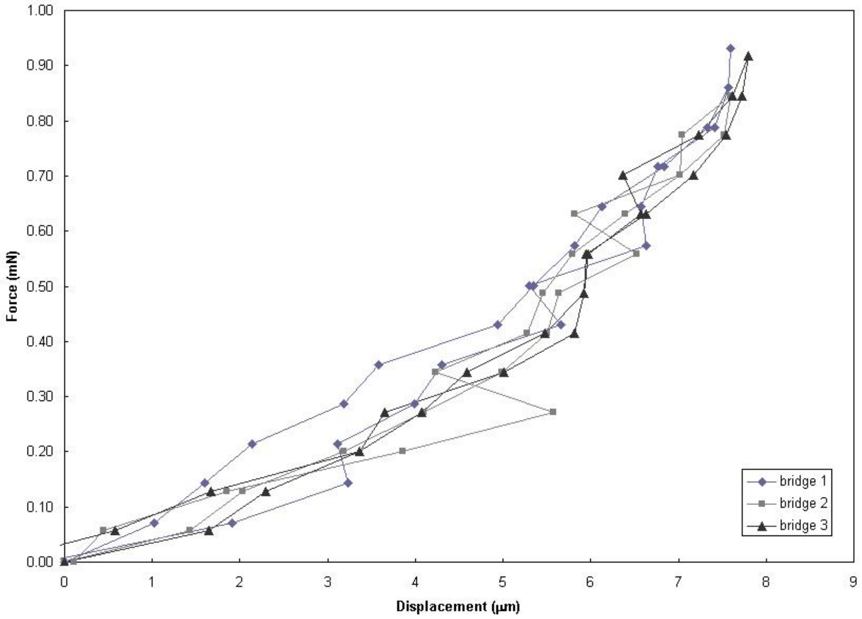

Figure 3.31: F-d $PbTiO_3/SrRuO_3/IBAD/SiO_2$.

sistance in the film itself, indicating an oxygen deficiency. Finally, although the application of voltage did not actuate the films, the measurement proved useful as a means to detect the error in the PSD. As voltage was applied and removed, the sample did not displace by any significant amount with any statistically significant trend. The data was scattered about zero displacement and as evident from Figure 3.32, the error is approximately 0.5 μm.

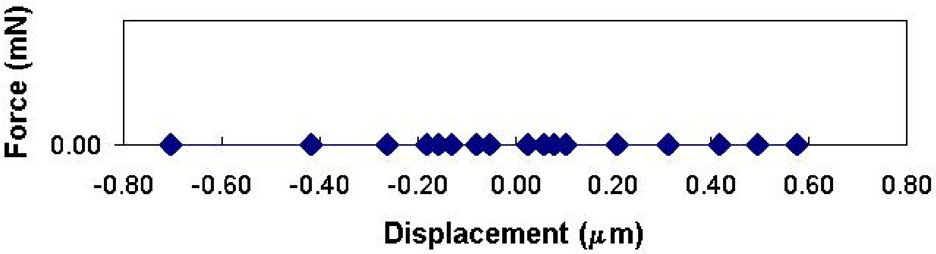

Figure 3.32: Displacement plotted for ineffective voltages from -10 to 10 V.

3.5 Conclusion

Although the fabrication techniques presented here are novel and lithographic patterning has CMOS compatibility and device volume advantages, postprocessing of ferroelectric MEMS is not a desirable process. The layer-by-layer ex-situ processing creates major film quality concerns. The XeF_2 etching most likely slightly roughens the SiO_2 surface during the long Si removal etch. The choice of Au as a bottom electrode was detrimental for CVD growth. PLD films of $PbTiO_3$ on the oxide electrode were non-continuous and mechanically unstable.

Nevertheless, the test method for mechanically characterizing these devices has proven repeatable, and data fitting has given some insight into the mechanical properties of the layers. Also, the characterization techniques confirmed the microstructures developed were accurate.

The next chapter will investigate how to make MEMS devices with monolithically integrated layers and ion milling to define device structures as an alternative to post-patterning growth.

Chapter 4

Voltage-Displacement Testing of Thin Film Barium Titanate MEMS Cantilevers

4.1 Abstract

Three critical microstructures - fiber textured, biaxially textured, and single crystal textured are realized in $BaTiO_3$ MEMS cantilever devices. Layers are grown monolithically, and devices are patterned on the surface via focused ion beam (FIB) milling of structures and XeF_2 etching of silicon substrates. Testing is done with voltage applied across the active layer, and displacement of the cantilever is measured via inspection with optical microscopy. Macroscopic device performance is related to microscopic piezoelectric constants via multimorph calculations. The experiment shows evidence that the device performance is enhanced with enhancement in microstructure - from fiber to biaxial to single crystal texture.

4.2 Introduction and Model

The relationship between crystallographic microstructure and thin film device performance is one of fundamental scientific importance in the field of materials science. Ferroelectric materials, specifically considering perovskite $BaTiO_3$, are of interest due to their electromechanical response via domain switching, which may be exploited in MEMS actuator devices. This chapter will present a systematic study of three key microstructures incorporated into cantilever devices. Utilizing a d_{31} actuation scheme in a cantilever geometry, where an

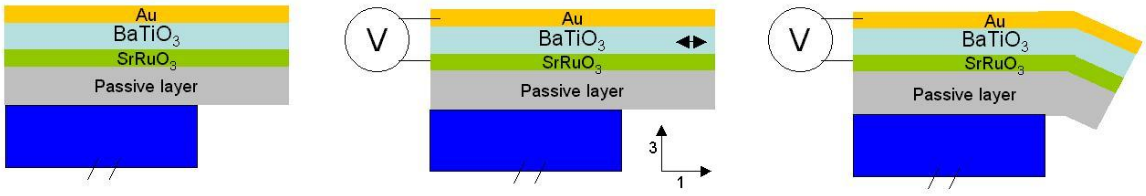

Figure 4.1: Cantilever device actuation schematic.

electric field in the 3-direction causes a contraction of grains in the 1-direction (hence why the d_{31} constant is negative) (Figure 4.1), the deflection of the device is proportional to this piezoelectric value and also the applied voltage. Thus the microstructures may be quantitatively compared in a meaningful way as realized in these devices.

The basic model considered will investigate the performance of piezoelectric heterogeneous multimorph actuators. The structures consist of a single active piezoelectric layer, with electrodes on top and bottom, and an additional bottom elastic layer. The purpose of the elastic layer is to offset the neutral axis of the system so that a lateral strain produced by the piezoelectric effect is translated into an applied moment on the bimorph. The multimorph model used to analyze the devices presented here is described in (DeVoe and Pisano, 1997). Assumptions of the model include negligible shear effects and electrostriction, ignoring stress-induced curvature, beam thickness less than piezoelectric induced curvature, and xz-plane strain and xy-plane stress enforced. For this application, we assume a 4-layer multimorph where the layer 4 is the top electrode, layer 3 is the piezoelectric $BaTiO_3$, layer 2 is the $SrRuO_3$ bottom electrode, and layer 1 is either SiO_2, Si_3N_4, or MgO, depending on thin film microstructure (to be discussed in the following section). Enforcing static equilibrium and strain compatibility between successive layers in the device yields the following equations. First, the sum of axial forces (F) and moments (M) must be zero at equilibrium, where t is thickness:

$$\sum_{i=1}^{4} F_i = 0 \,, \tag{4.1}$$

$$\sum_{i=1}^{4} M_i = F_1(\frac{t_1}{2}) + F_2(t_1 + \frac{t_2}{2}) + F_3(t_1 + t_2 + \frac{t_3}{2}) + F_4(t_1 + t_2 + t_3 + \frac{t_4}{2}) \,. \tag{4.2}$$

Next, from Euler's beam equation, $MR = EI$, it is clear that each individual layer's moment is related to the radius of curvature, R (approximately equal for each layer based on assumptions above), the individual modulus E_i and moment of inertia I_i:

$$M_i = \frac{E_i I_i}{R} \,. \tag{4.3}$$

Combining Equation (4.2) and Equation (4.3) and solving for curvature, we have

$$\frac{1}{R} = \frac{F_1(\frac{t_1}{2}) + F_2(t_1 + \frac{t_2}{2}) + F_3(t_1 + t_2 + \frac{t_3}{2}) + F_4(t_1 + t_2 + t_3 + \frac{t_4}{2})}{E_1 I_1 + E_2 I_2 + E_3 I_3 + E_4 I_4} \,, \tag{4.4}$$

that may be written in matrix form as follows:

$$\frac{1}{R} = \begin{bmatrix} d_1 & d_2 & d_3 & d_4 \end{bmatrix} \cdot \begin{bmatrix} F_1 \\ F_2 \\ F_3 \\ F_4 \end{bmatrix} \,, \tag{4.5}$$

where d_1, d_2, d_3, d_4, are defined as

$$\begin{aligned} d_1 &= \tfrac{\frac{t_1}{2}}{E_1 I_1 + E_2 I_2 + E_3 I_3 + E_4 I_4} \,, \; d_2 = \tfrac{t_1 + \frac{t_2}{2}}{E_1 I_1 + E_2 I_2 + E_3 I_3 + E_4 I_4} \,, \\ d_3 &= \tfrac{t_1 + t_2 + \frac{t_3}{2}}{E_1 I_1 + E_2 I_2 + E_3 I_3 + E_4 I_4} \,, \; d_4 = \tfrac{t_1 + t_2 + t_3 + \frac{t_4}{2}}{E_1 I_1 + E_2 I_2 + E_3 I_3 + E_4 I_4} \,. \end{aligned} \tag{4.6}$$

For the sake of brevity, we may redefine Equation (4.5) as

$$\frac{1}{R} = \mathbf{D} \cdot \mathbf{F} \,. \tag{4.7}$$

Additionally, enforcing strain compatibility at the 3 interfaces (between each layer i and $i + 1$) of the device yields:

$$d_{31} E_i + \frac{F_i}{A_i E_i} - \frac{t_i}{2R} = d_{31} E_{i+1} + \frac{F_{i+1}}{A_{i+1} E_{i+1}} + \frac{t_{i+1}}{2R} \,, \tag{4.8}$$

where the individual strains are a superposition of the piezoelectric effect, axial force, and beam bending and E_i is only nonzero for the piezoelectric layer. Incorporating all interfaces and rewriting the strain compatibility condition expression in matrix form, we have:

$$\begin{bmatrix} \frac{1}{A_1E_1} & \frac{-1}{A_2E_2} & 0 & 0 \\ 0 & \frac{1}{A_2E_2} & \frac{-1}{A_3E_3} & 0 \\ 0 & 0 & \frac{1}{A_3E_3} & \frac{-1}{A_4E_4} \\ 1 & 1 & 1 & 1 \end{bmatrix} \cdot \begin{bmatrix} F_1 \\ F_2 \\ F_3 \\ F_4 \end{bmatrix} - \tfrac{1}{2R} \begin{bmatrix} t_1+t_2 \\ t_2+t_3 \\ t_3+t_4 \\ 0 \end{bmatrix} - d_{31} \begin{bmatrix} E_2-E_1 \\ E_3-E_2 \\ E_4-E_3 \\ 0 \end{bmatrix} = \begin{bmatrix} 0 \\ 0 \\ 0 \\ 0 \end{bmatrix} . \tag{4.9}$$

This expression may be defined as:

$$\mathbf{A} \cdot \mathbf{F} - \frac{1}{2R}\mathbf{B} - d_{31}\mathbf{C} = 0\,. \tag{4.10}$$

Combining this with Equation (4.7) and solving for curvature, we see:

$$\frac{1}{R} = \frac{2d_{31}\mathbf{D}\mathbf{A}^{-1}\mathbf{C}}{2 - \mathbf{D}\mathbf{A}^{-1}\mathbf{B}}\,. \tag{4.11}$$

Deflection of beam device is related to curvature by $\delta(x) = \frac{x^2}{2R}$ where x is the point along the beam where displacement is measured and thus we have:

$$\delta(x) = \frac{x^2}{2R} = x^2[\frac{d_{31}\mathbf{D}\mathbf{A}^{-1}\mathbf{C}}{2 - \mathbf{D}\mathbf{A}^{-1}\mathbf{B}}]\,. \tag{4.12}$$

Assuming identical widths, $E_3 = \frac{V}{t_3}$ for piezoelectric layer 3, $x = L$ for the tip deflection, and moment of inertia $\frac{wt^3}{12}$ for rectangular cross section we derive:

$$\begin{aligned} \delta(x) = {} & [-(3d_{31}E_3(E_2t_2(t_2+t_3) + E_1t_1(t_1+2t_2+t_3) - E_4t_4(t_3+t_4)))VL^2] \\ & /[E_1^2t_1^4 + E_2^2t_2^4 + E_3^2t_3^4 + 4E_3E_4t_3^3t_4 + 6E_3E_4t_3^2t_4^2 + 4E_3E_4t_3t_4^3 + E_4^2t_4^4 \\ & +2E_1t_1(E_2t_2(2t_1^2 + 3t_1t_2 + 2t_2^2) + E_3t_3(2t_1^2 + 6t_1t_2 + 6t_2^2 + 3t_1t_3 + 6t_2t_3 \\ & +2t_3^2) + 2E_4(t_1^2 + 3t_1(t_2+t_3) + 3(t_2+t_3)^2)t_4 + 3E_4(t_1 + 2(t_2+t_3))t_4^2 \\ & +2E_4t_4^3) + 2E_2t_2(E_3t_3(2t_2^2 + 3t_2t_3 + 2t_3^2) + E_4t_4(2t_2^2 + 6t_2t_3 + 6t_3^2 + 3t_2t_4 \\ & +6t_3t_4 + 2t_4^2))]\,. \end{aligned} \tag{4.13}$$

Thus we may use the above expression to fit the data (given layer thicknesses and assuming moduli) and extract an effective d_{31} for devices of each microstructure type.

4.3 Experimental

4.3.1 Monolithic sample preparation

Samples were prepared with layer-by-layer growth. Substrates used include Si_3N_4/Si or SiO_2/Si (studied for the possibility of CMOS integration applications) and single crystal MgO for homoepitaxial growth. IBAD MgO templates were used to achieve fiber and biaxial texture on the silicon substrates. $SrRuO_3$ was used as a bottom electrode in all cases, deposited via PLD. $SrRuO_3$ was deposited with an O_2 pressure of 200 mTorr, turbo at 600 Hz, for 18000 shots at 10 Hz with a 350 mJ laser. The substrate temp was 650 °C. $BaTiO_3$ was also deposited via PLD, at an O_2 pressure of 10 mTorr, turbo at 1000 Hz with 18000 shots at 10 Hz of a 350 mJ laser. Substrate temperature was also 650 °C. Both the $SrRuO_3$ and $BaTiO_3$ were approximately 250 nm thick. Thermally evaporated Au was used as a top contact.

Fiber textured samples were realized on SiO_2/Si substrates. Using existing samples from Chapter 3, the surface of which had already experienced slight roughening from XeF_2 etching of old oxide bridge structures, IBAD MgO templates were deposited. The resulting MgO texture is evident from the RHEED pattern shown in Figure 4.2. The MgO film is essentially polycrystalline and a good candidate for encouraging fiber texture, as there is no in-plane texture to be inherited.

Biaxially textured samples were realized on Si_3N_4/Si substrates. IBAD MgO templates were deposited and excellent biaxial texture is achieved, due to the surface roughness being quite low (less than 1 nm RMS). The RHEED pattern is shown in Figure 4.3 and exhibits clear spots and a cubic structure. The MgO film on Si_3N_4 is therefore a suitable template for biaxial texture inheritance.

Fiber texture and biaxial textures samples were prepared as described above, with the IBAD MgO growth in the MBE chamber. Both samples were then removed from vacuum and introduced into the PLD chamber for $SrRuO_3$ and $BaTiO_3$ depositions. Between the electrode and piezoelectric growth, the sample was removed from vacuum and masked. It was found that this break in vacuum introduces some degree of contamination resulting in

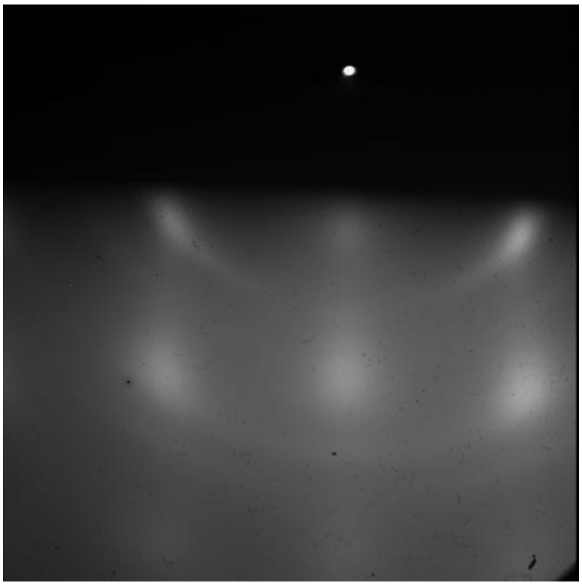

Figure 4.2: RHEED image of MgO template on SiO_2/Si.

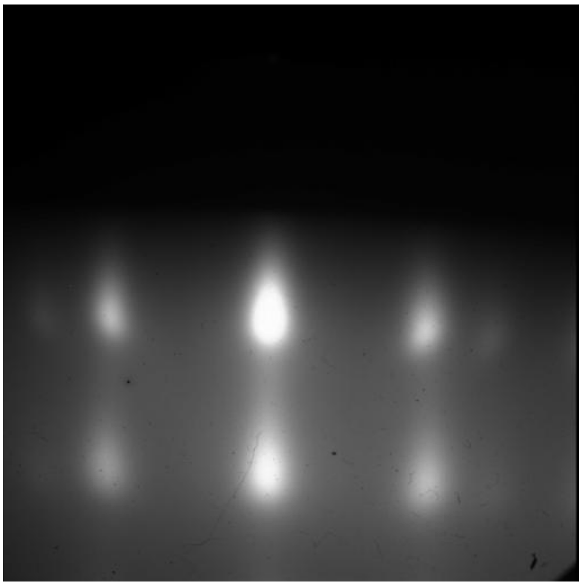

Figure 4.3: RHEED image of MgO template on Si_3N_4/Si.

a degree of polycrystallinity in the microstructures of the films. Therefore the single crystal microstructure is prepared without breaking vacuum.

The single crystal microstructure results from the epitaxial growth of $SrRuO_3$ and $BaTiO_3$ via PLD in succession without a break in vacuum. The RHEED pattern for bulk, single crystal MgO is shown in Figure 4.4. Due to the excellent lattice match between the

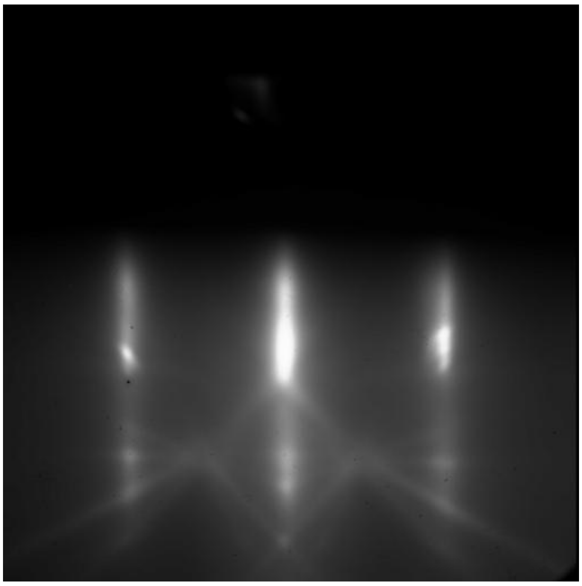

Figure 4.4: RHEED image of single crystal MgO substrate.

substrate and the deposited layers, the microstructure of our deposited films was nearly single crystal.

4.3.2 Focused ion beam milling

A gallium ion beam system was used to etch material from the surface of the monolithic samples. Initial work on fiber textured samples utilized a beam energy of 30 kV and a current of 20nA. Due to the high beam current and rapid etch rate of Au, the Au top contact was etched away on the remaining cantilever as initially less than 100nm of Au was deposited. This is seen in Figure 4.5. Thus subsequent devices had thicker gold electrodes, 250 nm or more.

In the case of fiber textured samples, the etch process resulted in some of the 2 μm thick SiO_2 being redeposited and collecting on the sidewalls after the patterns had been defined. After the XeF_2 etch (done ex situ of the FIB SEM), Figure 4.6 shows the redeposited material on the released cantilever. This is avoided by incorporating an oxide etch gas (2,2,2-trifluoroacedtamide as provided by the FEI Company) while the beam was on as well. This significantly reduced milling time and also removed sputtered material while the depth was defined. Figure 4.7 shows fiber textured cantilevers etched with various dose times of the FIB. Figure 4.8 shows the cantilevers after the XeF_2 etching. The higher doses

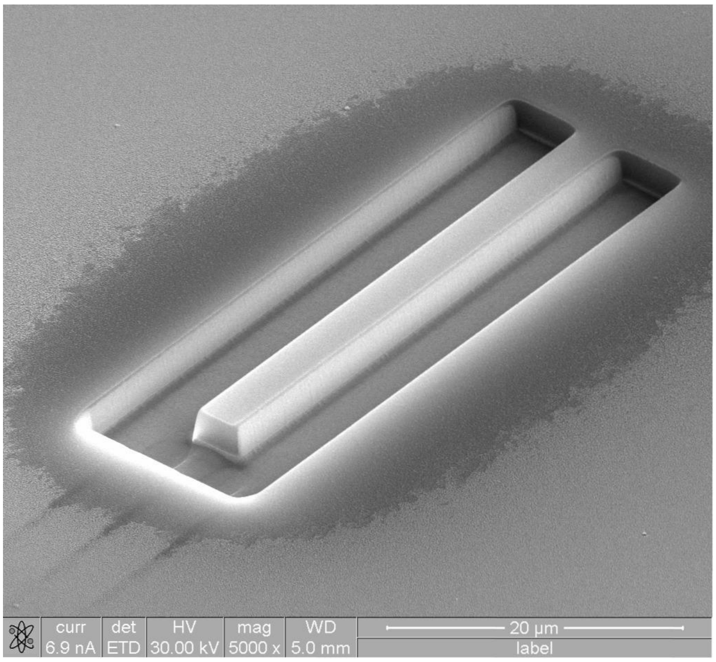

Figure 4.5: SEM image indicating FIB milling with 20 nA beam current clearly damages Au layer on patterned device.

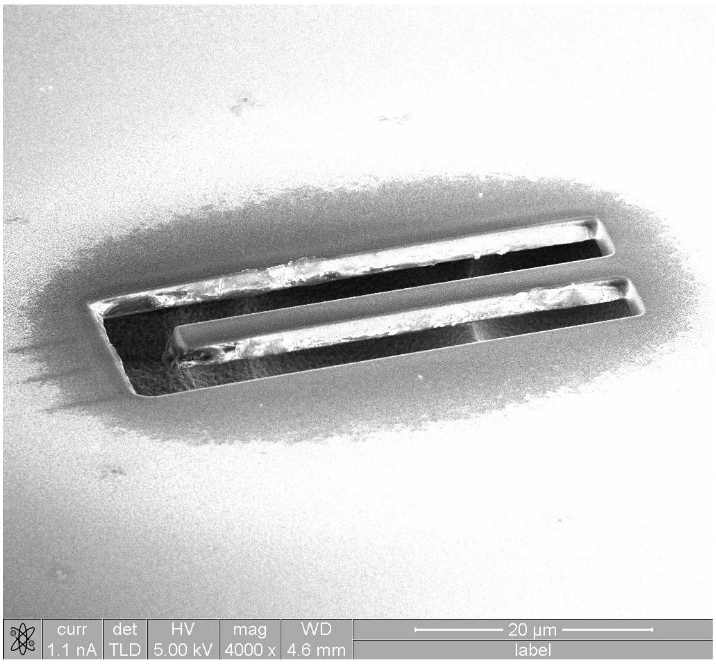

Figure 4.6: SEM image of cantilever released after XeF_2 etching of Si substrate. Cantilever has debris collected on sidewalls.

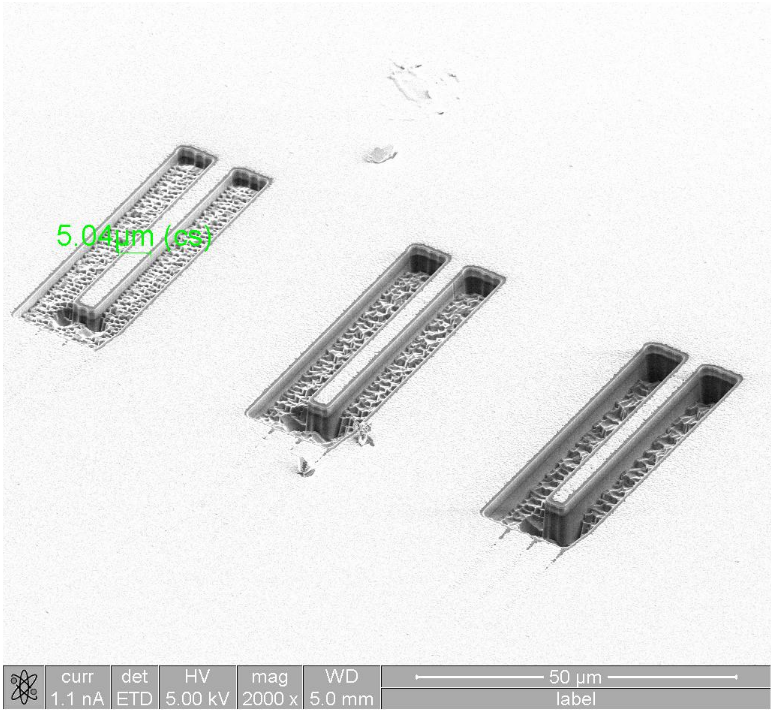

Figure 4.7: Using a delineation etch during patterning, cantilevers are defined with increasingly deep patterns, from left to right.

(depths of 5 μm or higher) are preferable, as some critical depth into the silicon must be reached in order to ensure all SiO_2 has been removed, as the XeF_2 cannot puncture through it. This is seen in Figure 4.9.

The beam energy was 30 kV, and the current was 5nA for milling of biaxially textured samples. Biaxially textured samples did not require an oxide etch gas as the Si_3N_4 was only 70 nm thick. Milling to a depth of approximately 500 nm was quick and did not cause any damage to the 250 nm Au top contact, as seen in Figure 4.10. Images of milled patterns prior to XeF_2 etching are shown in Figure 4.11.

As single crystal texture is achieved by epitaxial growth on single crystal MgO substrates instead of Si, the XeF_2 etch may not be utilized. Instead, structures are released by FIB milling at a 52^o angle to the surface and freeing a triangular shaped cantilever. The FIB voltage was in all cases 30 kV, and the current utilized for single crystal texture samples was varied throughout processing steps, depending on proximity to sample and reasonable milling time. A detailed process schematic is shown in Figure 4.12. First two large trenches are dug using a high beam current, 20 nA. They were defined particularly far from each

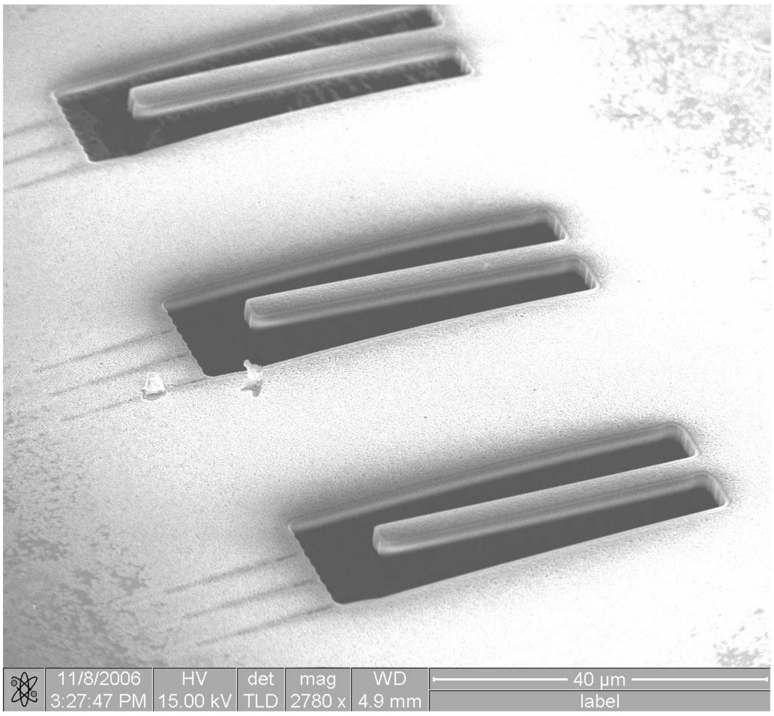

Figure 4.8: SEM image of $Au/BaTiO_3/SrRuO_3/MgO/SiO_2$ cantilevers after XeF_2 etching.

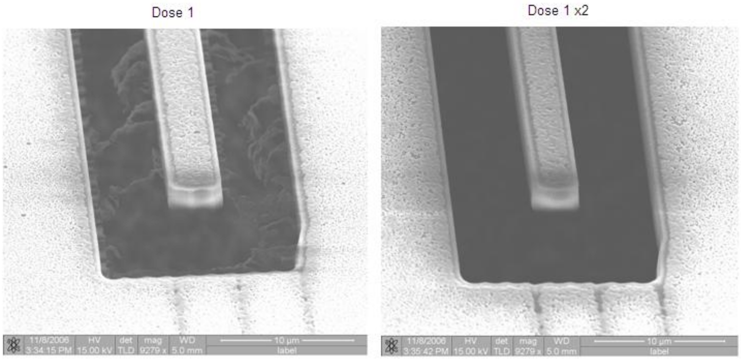

Figure 4.9: Comparison of released cantilevers after XeF_2 etching. The lower dose milled device (left) shows residual SiO_2.

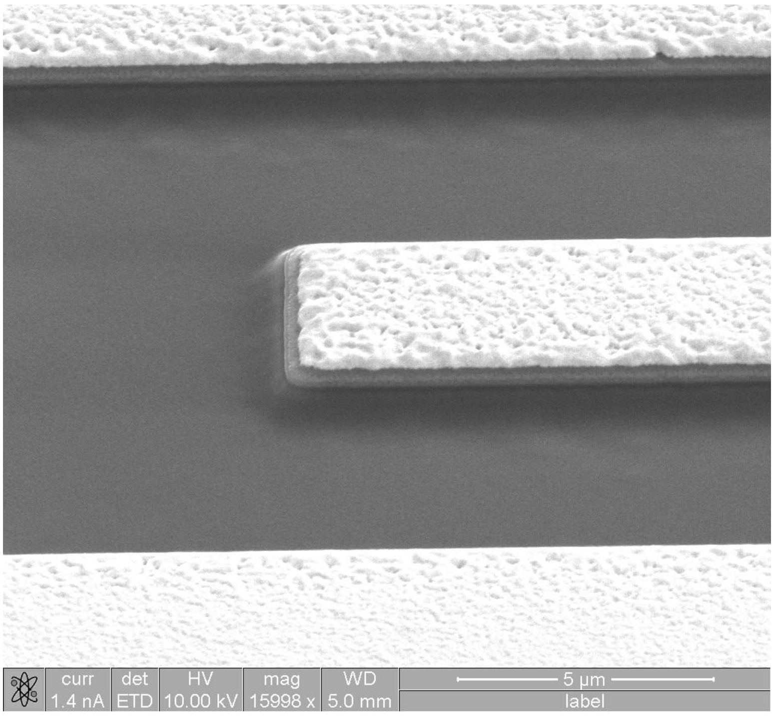

Figure 4.10: SEM image after FIB milling with 5 nA beam current shows no damage to Au top electrode.

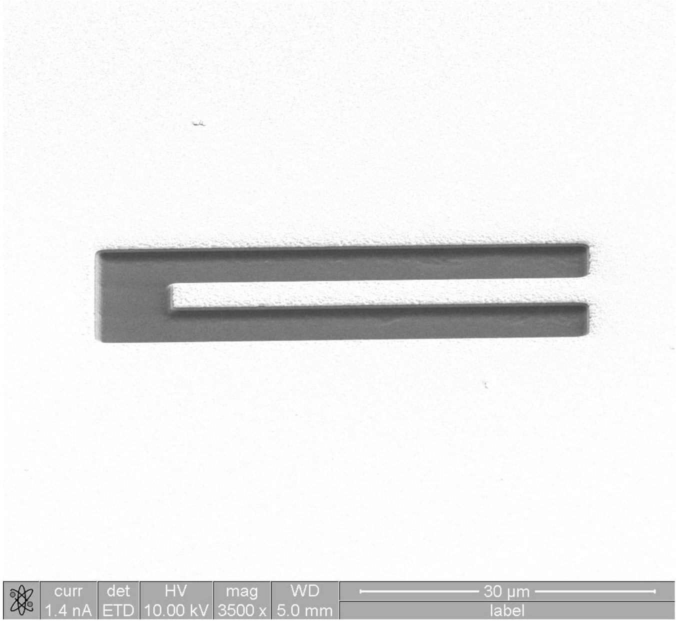

Figure 4.11: SEM image of Au/$BaTiO_3$/$SrRuO_3$/MgO/Si_3N_4/Si after FIB milling.

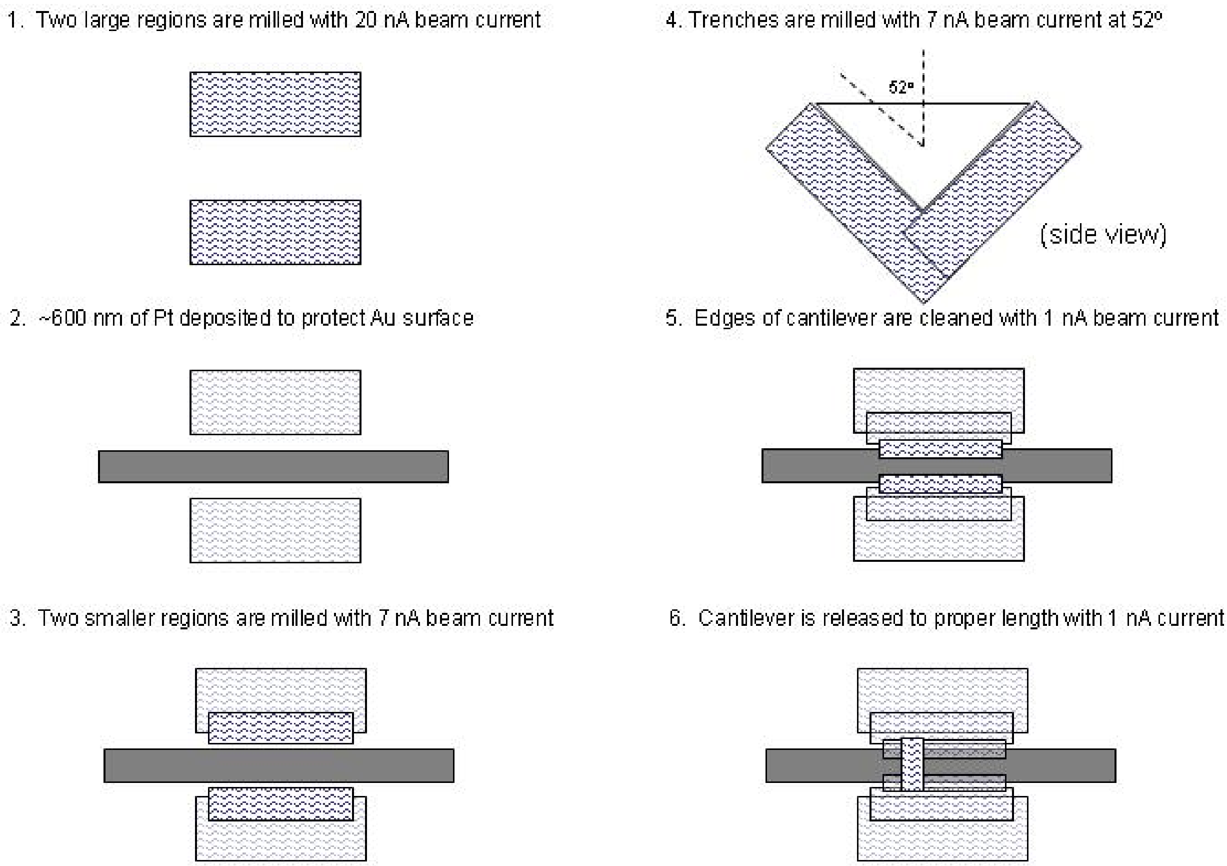

Figure 4.12: Schematic of FIB process to release cantilever from single crystal MgO substrate.

other because the higher current was sure to damage the surface. Next, a layer of Pt was deposited to protect the Au and also to serve as an initial target width for the cantilever. Next two smaller boxes were milled closer towards the Pt. A beam current of only 7 nA was used. Next the sample was tilted 52° and two trenches were dug underneath the cantilever, rotating the sample 180° between them. Finally, the three edges of the cantilever were cleaned with a small 1 nA current.

The completed structure is seen in Figure 4.13. The height of the triangular MgO support is estimated to be 4.9 μm in Figure 4.14 for use in modeling calculations.

All cantilever geometries were 40 μm long for straightforward direct comparison after testing. The widths may vary, but as seen in Equation (4.2), the width does not affect the displacement of the beam.

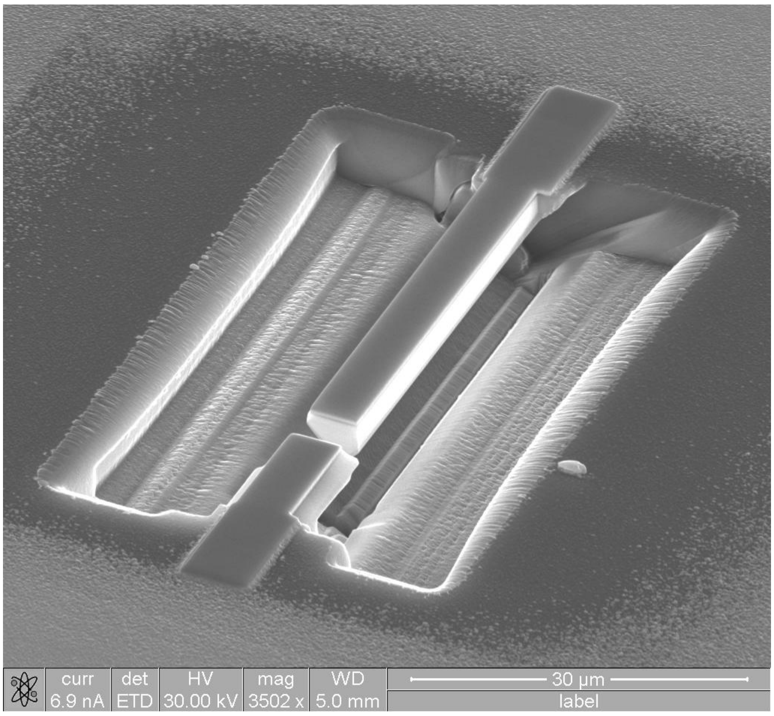

Figure 4.13: SEM image of completed cantilever etched out of single crystal MgO substrate.

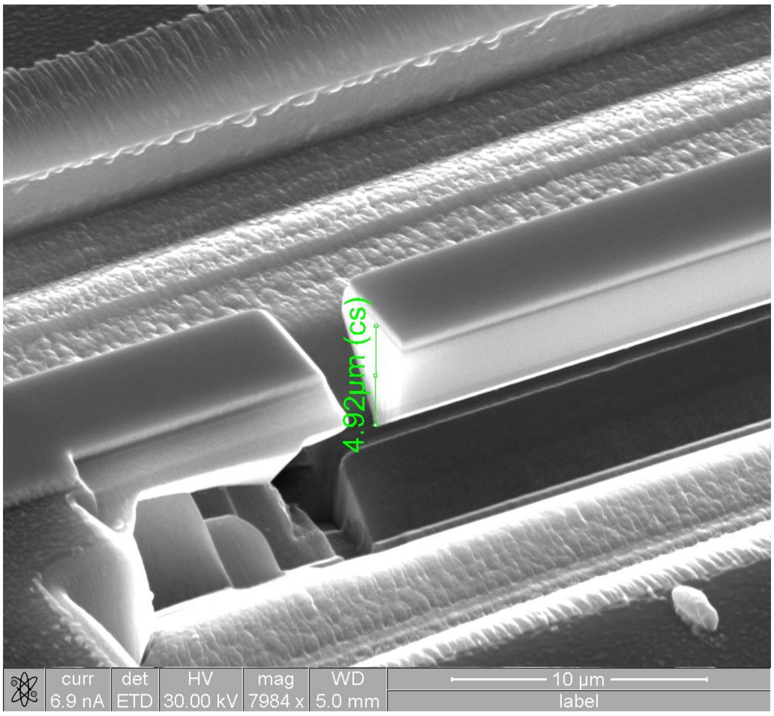

Figure 4.14: SEM image depicting triangularly shaped MgO passive layer for single crystal texture device.

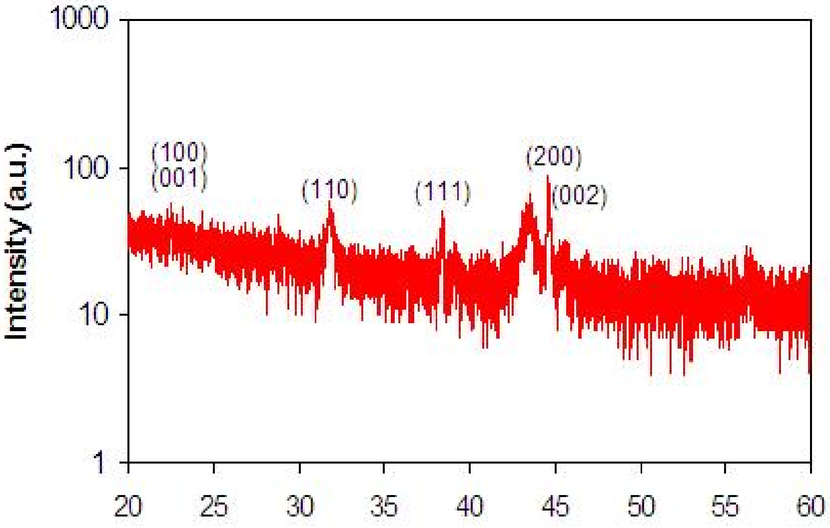

Figure 4.15: XRD θ-2θ scan of $BaTiO_3/SrRuO_3/SiO_2/Si$ sample. Only $BaTiO_3$ orientations are indexed.

4.4 Results and Discussion

4.4.1 Fiber texture

4.4.1.1 Microstructural characterization

Several techniques were utilized to analyze the fiber textured thin film microstructure. As discussed earlier, the break in vacuum during layer depositions introduces a degree of polycrystallinity into the microstructure, as seen in Figure 4.15. Off-axis 110 and 111 peaks are present in the film.

EBSD analysis was performed with a manual scanning technique, where patterns are indexed individually, instead of with the automatic recognition software. However, the patterns are very weak (Figure 4.16) and sparse, thus only a limited data sampling is collected (Figure 4.17). A pole figure plot is generated anyway, and results are seen in Figure 4.18. Thus despite the polycrystalline nature of the XRD, the data that were collected indicates some fiber texture.

Piezoresponse force microscopy (PFM) was performed using a modified Veeco Auto-Probe CP atomic force microscope equipped with conducting tips (either highly n-doped Si or Co-coated Si) with bias AC voltage in the 1-5 V range with frequency of 3-29 kHz and

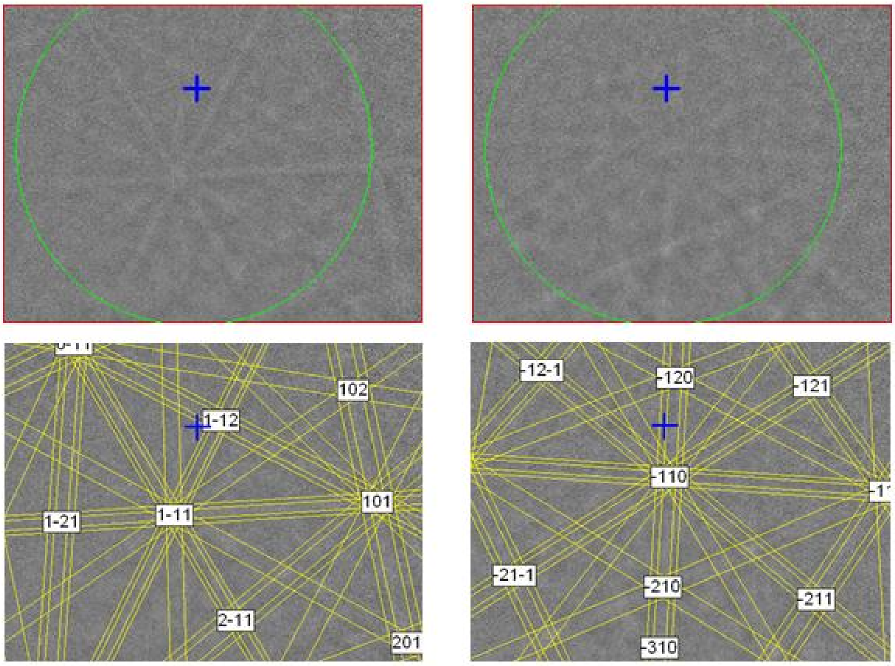

Figure 4.16: EBSD orientation patterns of fiber textured sample were faint.

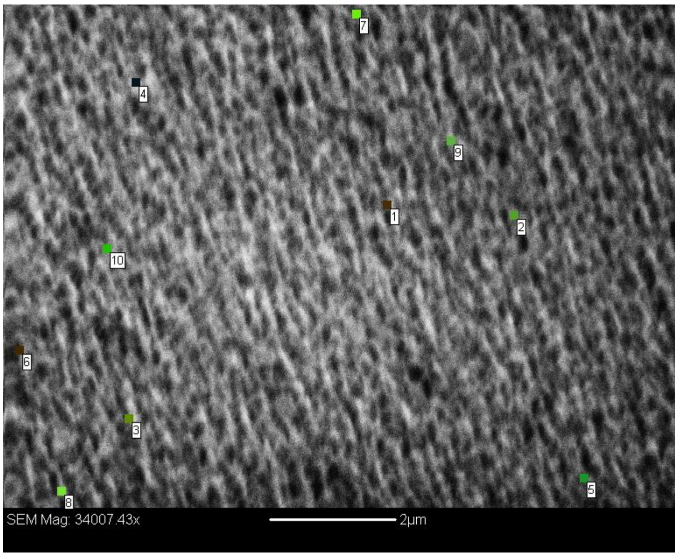

Figure 4.17: SEM of $BaTiO_3/SrRuO_3/MgO/SiO_2/Si$ sample with overlay of grains able to be indexed within view.

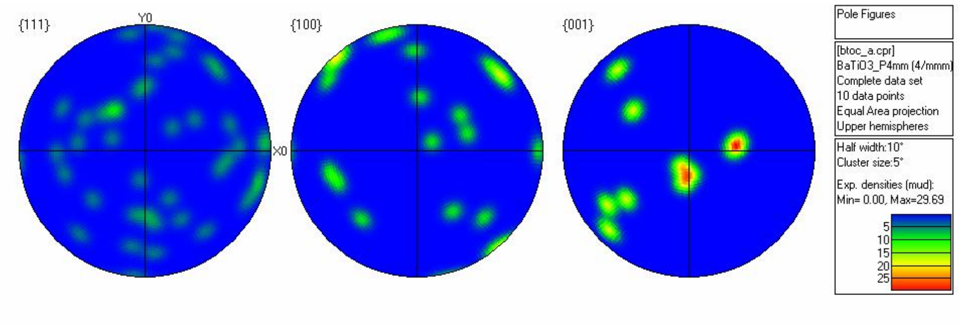

Figure 4.18: EBSD pole figure of $BaTiO_3/SrRuO_3/MgO/SiO_2/Si$ sample.

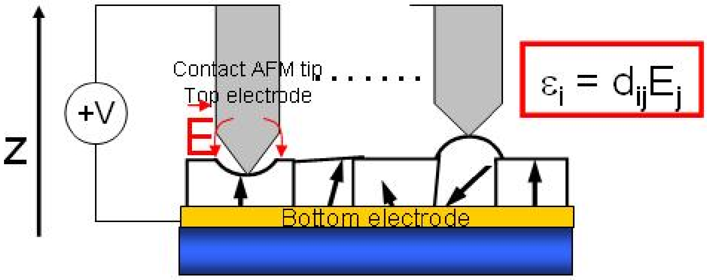

Figure 4.19: PFM schematic.

lock-in amplifier-based detection of the local piezoelectric response. The bottom electrode may be biased with the AFM tip as a top electrode and the response of each grain may be obtained along the scan (see Figure 4.19) simultaneously with AFM topographic information. Also, a piezoelectric hysteresis loop may be obtained by sweeping a DC bias source connected in series with the AC voltage source and recording the piezoresponse signal, which is proportional to the piezoelectric coefficient in that direction (Harnagea, 2001). PFM analysis was performed on unpoled samples to give an initial look at the microstructure as deposited. Figure 4.20 shows grain-scale domains as the piezoelectric signal correlates well with the grain topography. Also, Figure 4.20 shows the enhancement in grain boundaries and piezosignal when the voltage is increased. A tip voltage of 5V is therefore used in all subsequent scans.

Figure 4.21 shows the PFM scans and loops generated by leaving the AFM tip on a particular grain and sweeping the voltage from -10 to 10 Volts with 200 points per cycle and 0.2 seconds per bias. The average piezoresponse signal is around 6-8 mV.

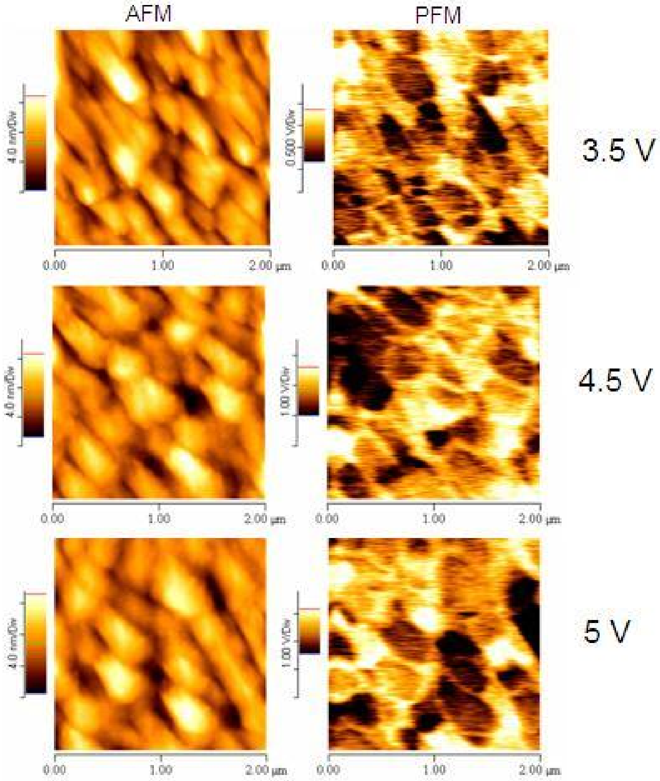

Figure 4.20: PFM of $BaTiO_3/SrRuO_3/MgO/SiO_2/Si$ with changing tip voltage. Tip frequency was 3 kHz and lock-in amplifier settings were 30 ms time constant and 500 μV sensitivity.

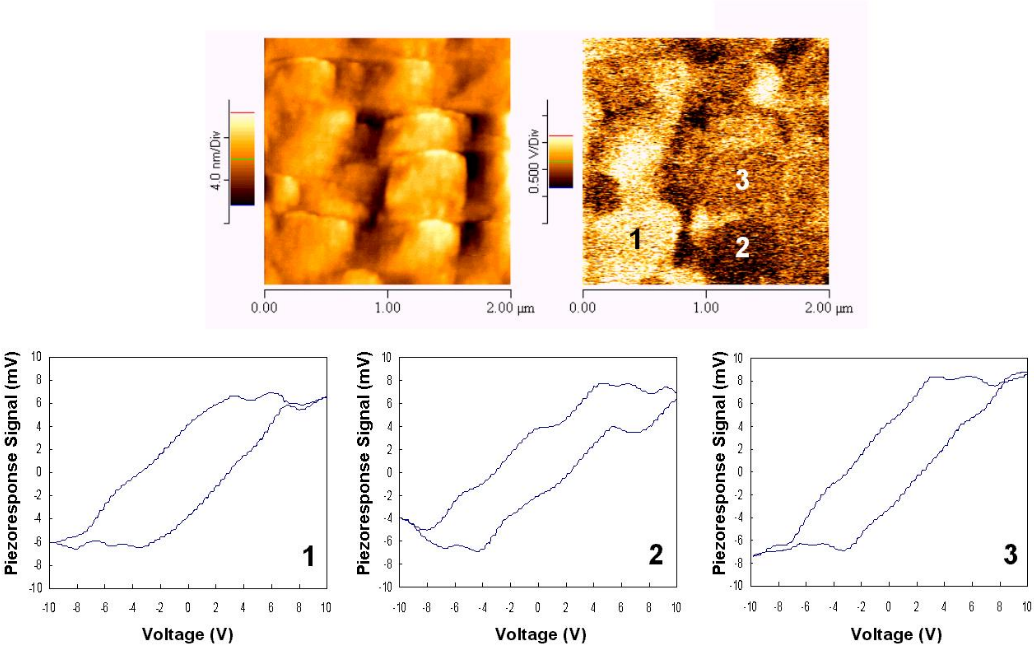

Figure 4.21: AFM/PFM images of fiber textured sample. PFM tip was 5 V, 5 kHz. 3 ms time constant and 1 mV sensitivity were lock-in settings. Also shown are piezohysteresis loops of specified grains.

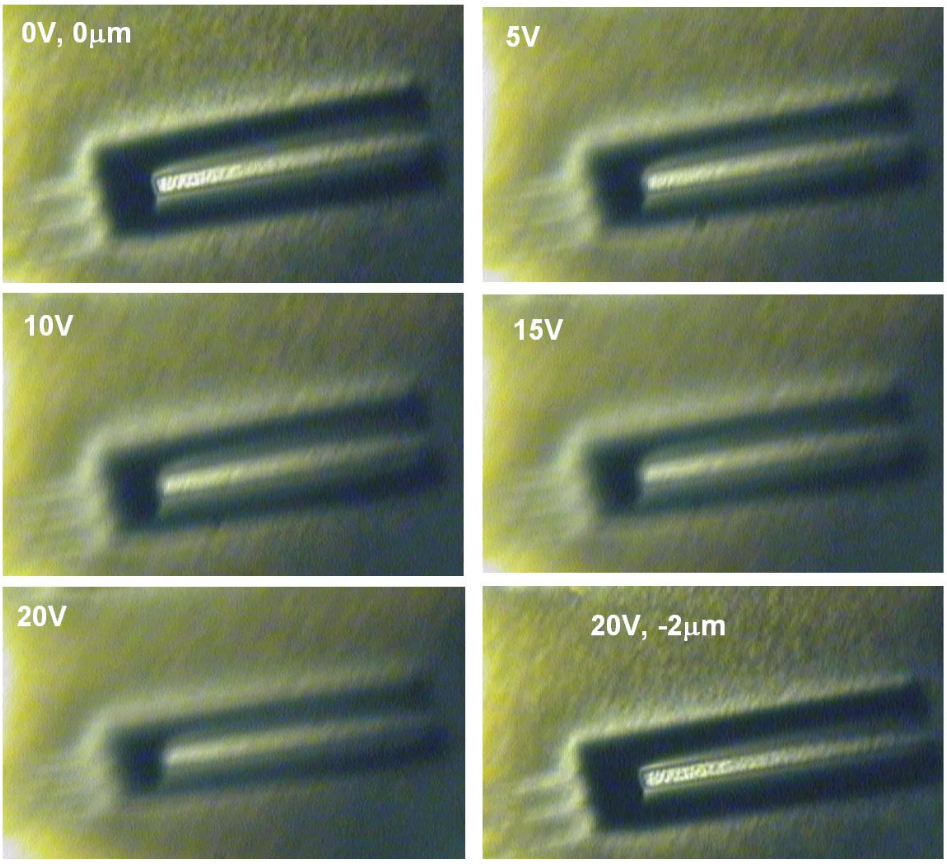

Figure 4.22: Fiber textured cantilever actuation at 100 X objective.

4.4.1.2 Macroscopic device testing

Device testing was performed on several cantilevers. Wires were run from the power supply to copper tape to the Au pad and exposed $SrRuO_3$. The tape ensured that the sample could be kept planar for viewing under the optical microscope objective. In all cases, devices were first tested by focusing on the cantilever tip, applying voltage and confirming that the cantilever tip moved out of focus and collecting images with increasing bias. Then the devices were retested, but were refocused for every voltage applied and the displacement necessary due to focusing was recorded. A combination of these techniques is presented in Figure 4.22, depicting a fiber textured cantilever. As each device was not electrically isolated from the next, the fact that data were repeatable is a testament to the robustness of the mechanical response mechanisms of the active $BaTiO_3$.

It should be noted that the optical images shown in Figure 4.22 depict the tip of the cantilever as well as the entire background going in and out of focus. This indicates that the substrate itself is moving with the applied field. An improved test method would include measuring the deflection of the tip of the cantilever with the base of the beam as a zero, as opposed to the focal plane of the microscope being the zero reference.

In the case of the fiber texture microstructure, each cantilever tested moved 1 μm with every 10 V applied (whether positive or negative). The resolution of the optical microscope was approximately 1 μm, so the data are not shown here, as they all were identical within this resolution. The data are exact, so the input of 1 μm displacement for 10 V applied voltage is fit to the model outlined in Section 4.2. The moduli of the oxide and Au are each assumed to be 70 GPa. In Chapter 4, the F-d fits reveal that the oxide bridges and un-annealed Au layers' moduli were approximately that value. The moduli of the $BaTiO_3$ and $SrRuO_3$ were assumed to be 250 GPa, as Chapter 2 suggested that texturing increases the stiffness in $BaTiO_3$ to larger than the single crystal value, or approximately 250 GPa (Figure 2.7). It was assumed that the SiO_2 is 2 μm thick, and the $BaTiO_3$, $SrRuO_3$, and deposited Au are 250 nm each. The MgO template and the Cr adhesion layers are ignored. The total beam length is 40 μm, as seen from the SEM images in the FIB milling section. With the aforementioned parameters, the effective d_{31} is found to be -117.95 pm/V. This value is nearly predicted from simulation in Chapter 2, Figure 2.5, with a texturing of low FWHM ψ and FWHM θ near 1 radian resulting in an effective d_{31} around -100 pm/V. However we have no real reason to speculate why a fiber textured device would have low FWHM ψ, other than assuming that the templating from the MgO to $SrRuO_3$ to $BaTiO_3$ for fiber texture ensures low twist about each of the out-of-plane angles.

4.4.2 Biaxial texture

4.4.2.1 Microstructural characterization

XRD for the biaxial texture classification is seen in Figure 4.23. There is more signal from the 001 and 100 orientations vs. the fiber textured sample thus indicating the enhanced MgO template provided better texturing.

EBSD analysis was also performed manually on the biaxially textured sample, but with a larger sampling of data points, as seen in Figure 4.24. The pole figure from these data, Figure 4.25, shows concentrations about 001 and 100, confirming the biaxial classification. The stray data arise from the off-axis orientations no doubt developed with the break in

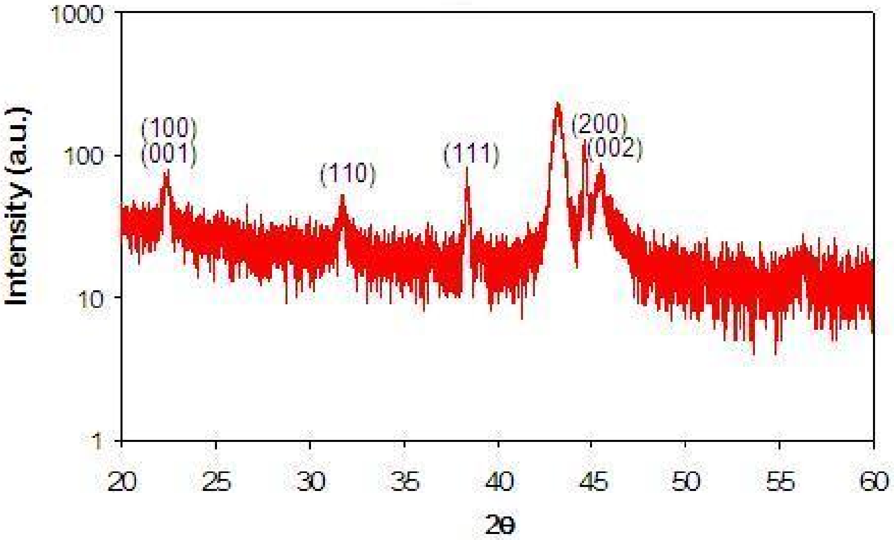

Figure 4.23: XRD θ-2θ scan of $BaTiO_3/SrRuO_3/Si_3N_4/Si$ sample. Only $BaTiO_3$ orientations are indexed.

vacuum during depositions.

PFM analysis of the biaxially textured film shows similar piezoresponse signal to the fiber textured film (6-8 mV), but with less noise during the sweep of voltages to generate the hysteresis plots, as seen in Figure 4.26.

4.4.2.2 Macroscopic device testing

Because the biaxially textured sample substrate is a thin Si_3N_4 layer on Si as opposed to a thick SiO_2 layer in the case of the fiber textured film devices, we expect the biaxially textured devices to deflect more. Images from the optical microscope are shown in Figure 4.27 and results from tip refocusing with every voltage applied are presented in Figure 4.28. As predicted, the devices move substantially more than the fiber textured devices, especially at low voltages. Therefore testing is only performed up to 10 V applied, to ensure the beam does not deflect low enough to hit the surface below it.

The moduli of the Si_3N_4 and Au are each assumed to be 70 GPa and $BaTiO_3$ and $SrRuO_3$ were assumed to be 250 GPa, identical to the biaxial texture case. The Si_3N_4 is assumed to be 100 nm thick, which really incorporates some of the MgO thickness, that is now more relevant considering the passive layers are much thinner than in the fiber textured samples. The $BaTiO_3$ and $SrRuO_3$ are 250 nm, and the deposited Au is also 250

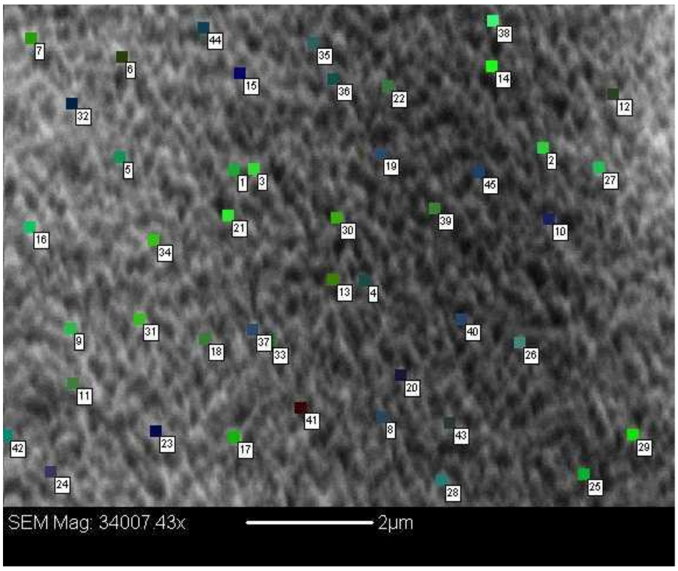

Figure 4.24: SEM of $BaTiO_3/SrRuO_3/MgO/Si_3N_4/Si$ sample with overlay of grains able to be indexed within view.

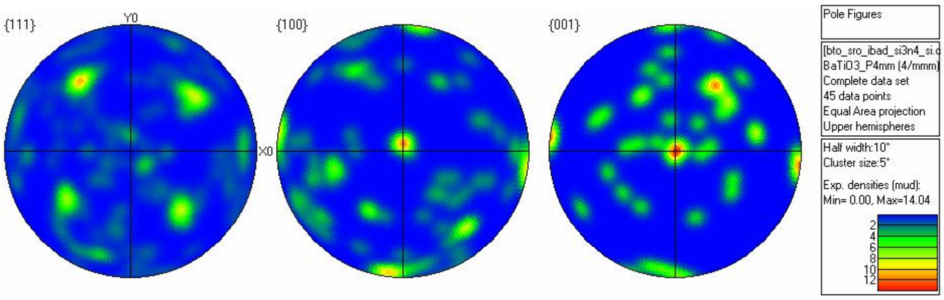

Figure 4.25: EBSD pole figure of $BaTiO_3/SrRuO_3/MgO/Si_3N_4/Si$ sample.

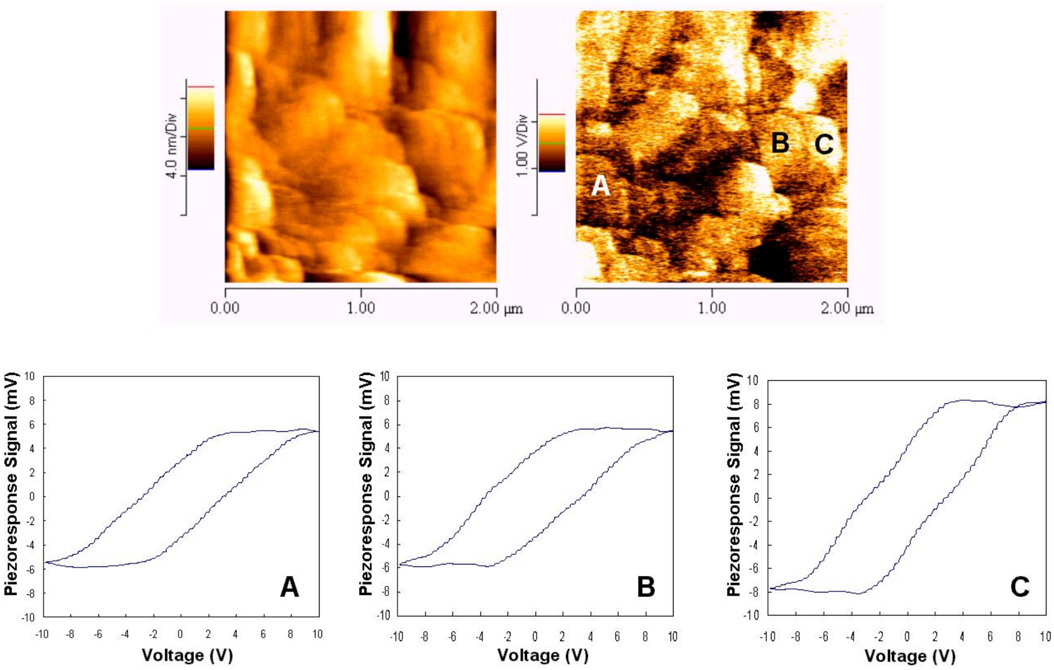

Figure 4.26: AFM/PFM images of biaxially textured sample. PFM tip was 5 V, 5 kHz. 3 ms time constant and 1 mV sensitivity were lockin settings. Also shown are piezo hysteresis loops of specified grains.

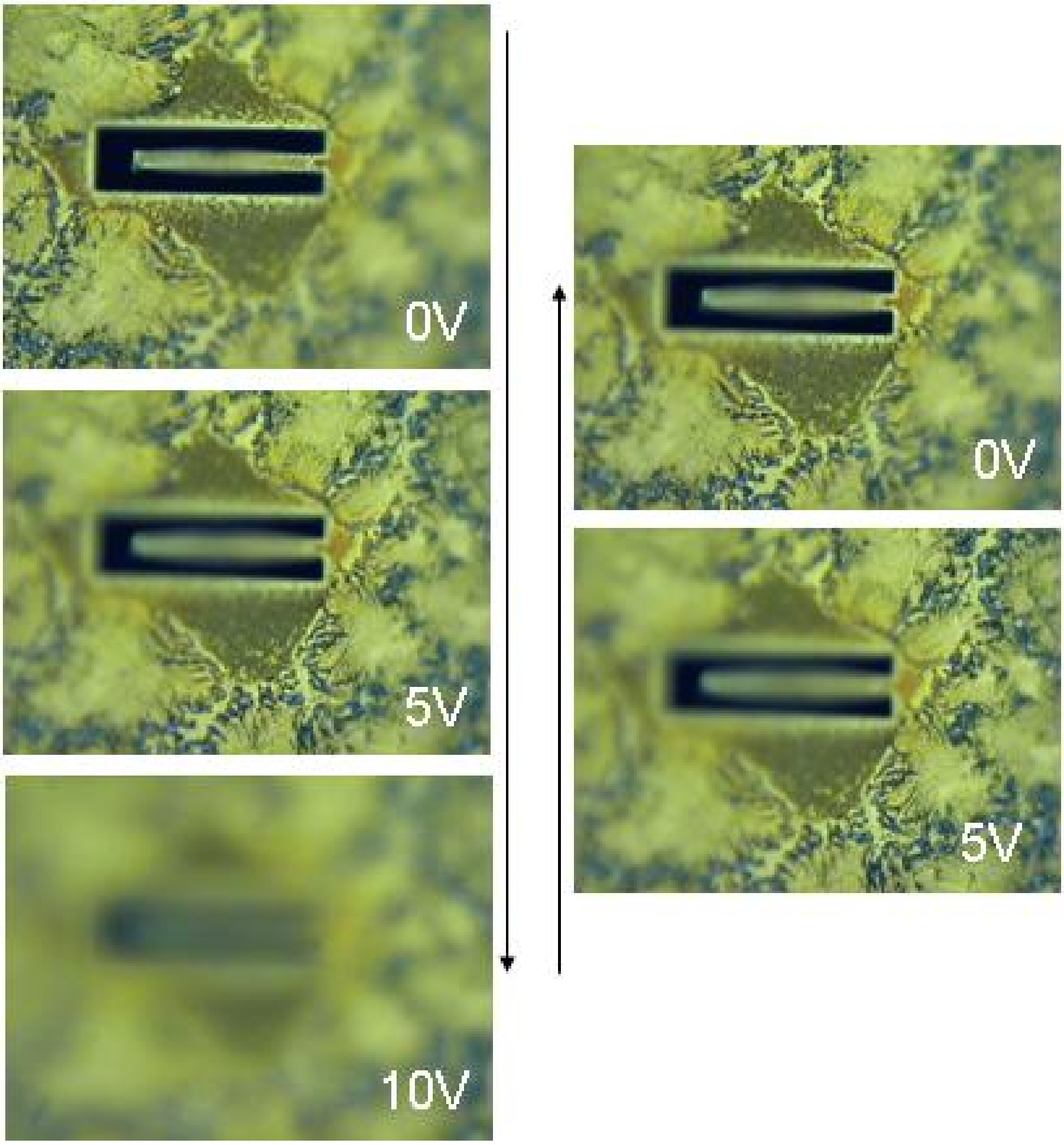

Figure 4.27: Biaxially textured cantilever actuation at 100 X objective.

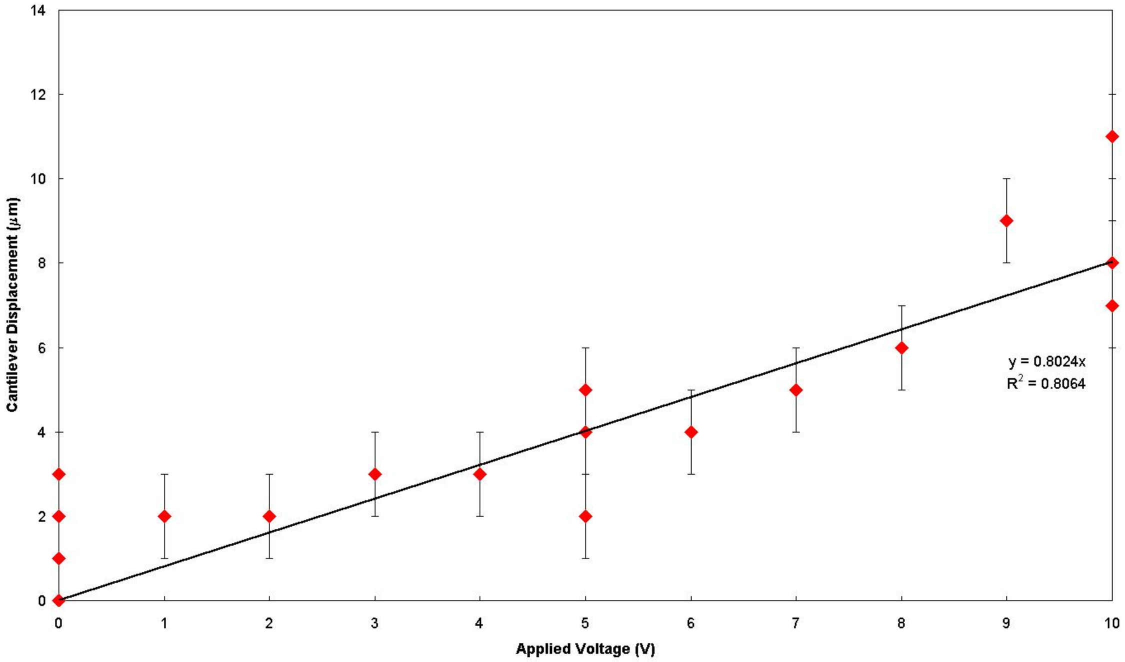

Figure 4.28: Displacement-voltage results for cantilevers of biaxial texture. Error in optical microscope focus is 1 μm.

nm. The total beam length is 40 μm. Inputting a beam displacement of 8 μm with 10 V applied (from fit in Figure 4.28), the effective d_{31} is -237.90 pm/V. This is nearly double the fiber texture microstructure devices value! The larger displacements at identical voltages are not only caused by the thinner passive layer but by an enhancement in the effective piezoelectric constant. The effective d_{31} for the biaxially textured devices is much higher than the single crystal value, and thus there must be small-scale switching in the $BaTiO_3$. Having more grains well aligned in- and out-of-plane increases the number of grains that may participate in switching, and thus the biaxially textured microstate has more switching and thus a much higher effective d_{31}, as compared with the fiber textured microstate.

4.4.3 Single crystal texture

4.4.3.1 Microstructural characterization

The single crystal microstructure was achieved by subsequent $SrRuO_3$ and $BaTiO_3$ deposition on single crystal MgO substrate without breaking vacuum in the PLD chamber. Because $SrRuO_3$ is so excellently lattice matched to $BaTiO_3$ and $SrRuO_3$ textures on single

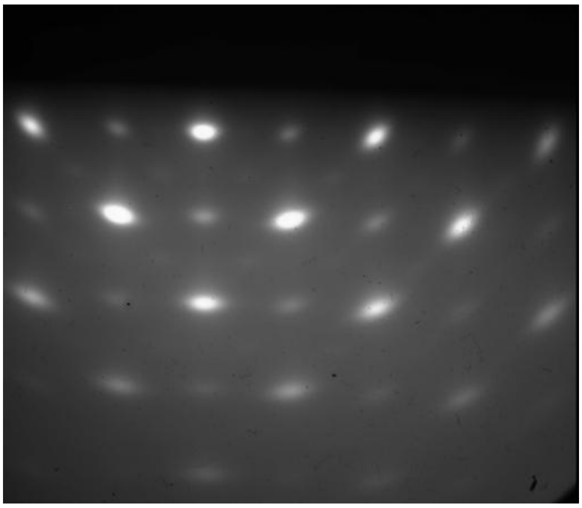

Figure 4.29: RHEED of PLD deposited $SrRuO_3$ on single crystal MgO substrate.

crystal MgO, giving evidence of pseudocubic structure from RHEED pattern as seen in Figure 4.29, the growth of $BaTiO_3$ will nearly be homoepitaxial.

The XRD from this sample is shown in Figure 4.30. Only 100 and 001 orientations are present. It is not possible to distinguish between them given the 1% difference in lattice constants of $BaTiO_3$.

EBSD analysis on this sample was done with only a few points as signal was hard to detect, due to charging of the surface. However faint the patterns, it was clear that the orientation was not changing much from grain to grain. Selecting some of these patterns and mapping to a pole figure, there is evidence of centers at 100 and 001 and 4-fold patterns otherwise, shown in Figure 4.31. Additionally, the technique for assigning orientations is not necessarily sensitive to delineate 100 or 001 orientations, so we may indeed call the texture single crystal.

PFM analysis results, shown in Figure 4.32, are quite similar to the fiber and biaxially textured samples, as piezoelectric hysteresis gives a maximum piezoresponse signal around 7 mV. Given that all three samples have given similar piezoresponse signals, perhaps the technique is not the correct characterization to predict how the active film will respond in the device, especially now that domain switching may play a significant role. All that can be said is that with substrate clamping, all textured film types have similar intrinsic response.

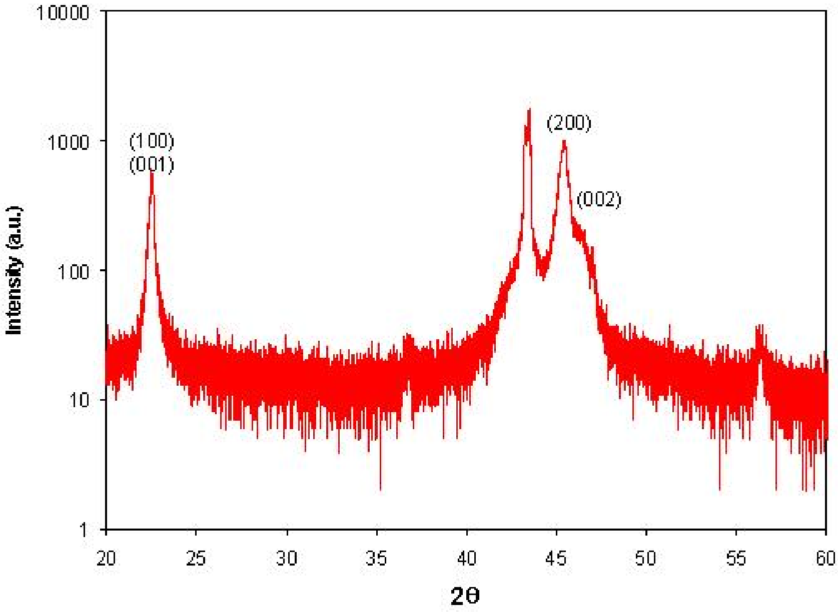

Figure 4.30: XRD θ-2θ scan of $BaTiO_3$/$SrRuO_3$/MgO sample. Only $BaTiO_3$ orientations are indexed.

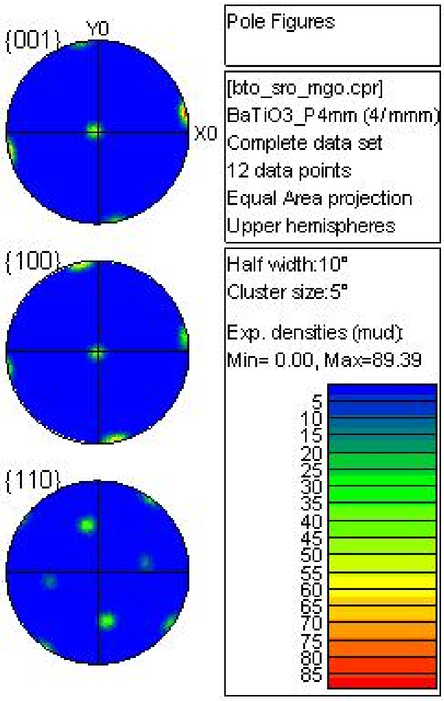

Figure 4.31: EBSD pole figure of $BaTiO_3$/$SrRuO_3$/MgO sample.

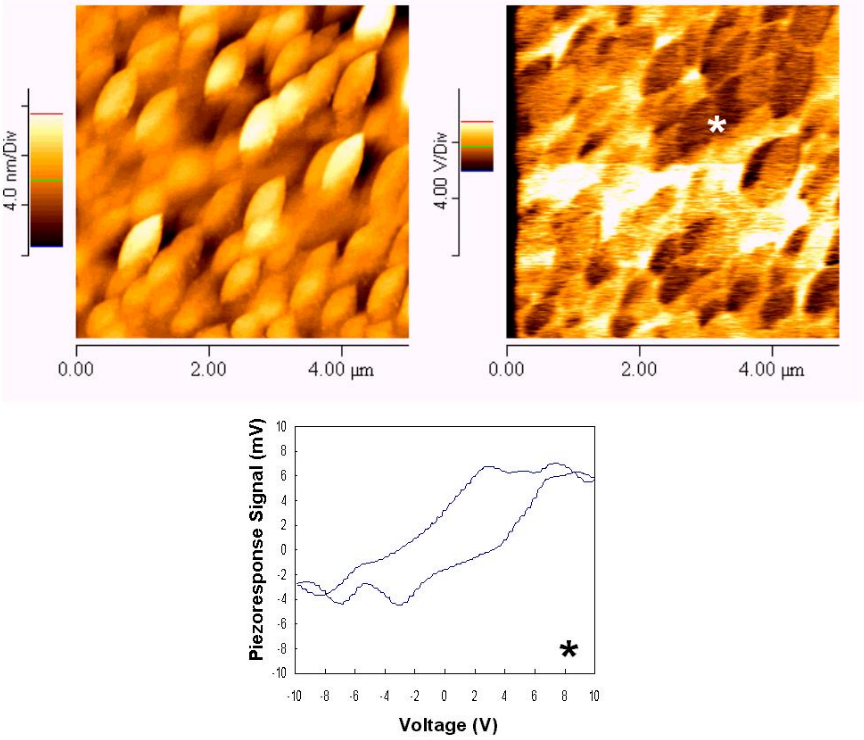

Figure 4.32: AFM/PFM images of single crystal textured sample. PFM tip was 5 V, 5 kHz. 3 ms time constant and 1 mV sensitivity were lockin settings. Also shown is piezo hysteresis loop of specified grain.

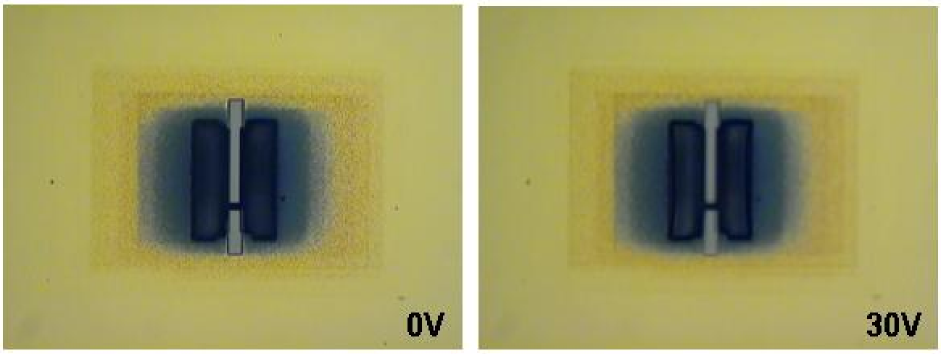

Figure 4.33: Representative single crystal cantilever actuation at 50 X objective.

4.4.3.2 Macroscopic device testing

The single crystal textured sample was grown without a mask step between the $SrRuO_3$ and $BaTiO_3$, so some $BaTiO_3$ was scratched off the sample and silver paste was applied over the scratch. This allowed access to the bottom electrode via the paste. However this arrangement was less than planar and limited the working distance during testing with the optical microscope, so the single crystal textured cantilevers were tested at 50 X objective. A representative view during actuation of the single crystal texture device is shown in Figure 4.33. Beam displacement as a function of voltage is shown in Figure 4.34. The cantilever deflection is lower than both the fiber and biaxially textured devices, as expected due to the thick passive MgO layer. Also, the error in these measurements is higher compared with previous textures and thus the data are more scattered, due to the 50X objective during testing (instead of 100X) and because only a single cantilever is tested.

The moduli of the MgO is assumed as 100 GPa. It is also assumed to be the only triangular cross section of all the layers, and therefore it's moment of inertia changes from $\frac{wt^3}{12}$ to $\frac{wt^3}{36}$, thus altering Equation (4.2) slightly. The thickness of the triangle is deduced from Figure 4.14 to be 4.9 μm. The top electrode is now given the properties of the combined Au and Pt, and we assume 100 GPa and 1 μm thickness. $BaTiO_3$ and $SrRuO_3$ still have 250 GPa moduli and each are 250 nm thick. The total beam length is 40 μm. Inputting a beam displacement of 0.9 μm with 10 V applied (from fit in Figure 4.34), the effective d_{31} is -430.11 pm/V. Thus the microstate with no degree of polycrystallinity and only 100 and 001 orientations indeed produces the highest effective d_{31} in a MEMS device.

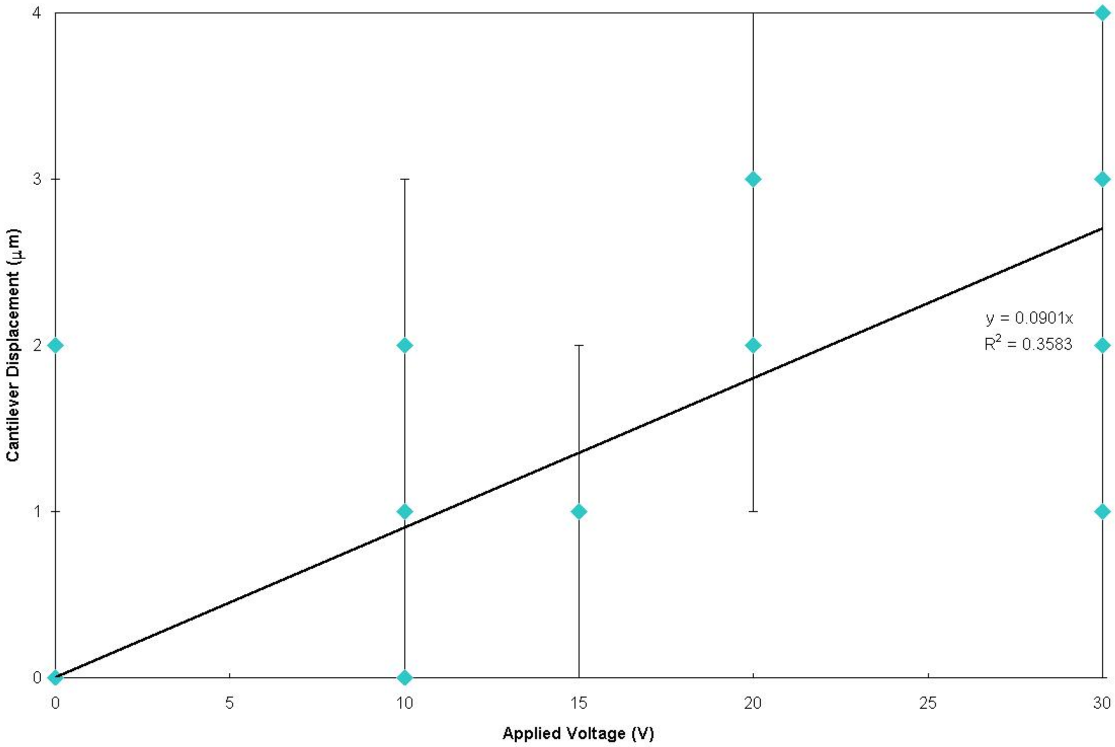

Figure 4.34: Displacement-voltage results for cantilevers of single crystal texture. Error in optical microscope focus is 1 μm.

Texture type	Fiber	Biaxial	Single
Beam displacement (μm)	**1**	**8**	**0.90**
Applied voltage (V)	10	10	10
E_{Au} (GPa)	70	70	**100**
E_{BaTiO_3} (GPa)	250	250	250
E_{SrRuO_3} (GPa)	250	250	250
$E_{passive}$ (GPa)	70	70	**100**
t_{Au} (μm)	0.25	0.25	**1**
t_{BaTiO_3} (μm)	0.25	0.25	0.25
t_{SrRuO_3} (μm)	0.25	0.25	0.25
$t_{passive}$ (μm)	**2**	**0.10**	**4.90**
d_{31} (pm/V)	-117.95	-237.90	-430.11

Table 4.1: Effective piezoelectric constants for the fiber, biaxial, and single crystal microstructures. Major differences in input values are highlighted.

A comparison of textured devices and modeled d_{31} values is shown in Table 4.1. The cantilever actuation with applied voltage is measured and fit with a linear relationship. The layer thicknesses and moduli, as well as the device dimensions have been considered in the model, and the comparison is reduced to the piezoelectric constant. So, although the single crystal textured film device deflected least in the beam actuation testing and was fabricated on the thickest passive layer, the microstructure produced the highest effective piezoelectric constant.

4.5 Conclusion

When an electric field is applied to a piezoelectric film, the mechanical response has two contributions: intrinsic due to the changes in polarization at the atomistic scales and extrinsic due to switching of domains (Bhattacharya and Ravichandran, 2003). Microstructural characterization in this chapter indicates piezoresponse signals from Figure 4.21, Figure 4.26, and Figure 4.32 are all nealy identical. As the scans were taken on a region of each sample that was clamped by the substrate, there was only signal due to intrinsic mechanical responses. If the devices were to perform and result in nearly identical d_{31} constants, we would expect the performance to be mostly due to intrinsic effects. However because we saw a difference in d_{31} dependent on microstructure, we must consider both intrinsic and extrinsic mechanical responses.

Different passive layer thicknesses added another dimension to analysis because each device had to strain against a different thickness layer, but results still show effective d_{31} increasing as we would expect, from fiber to biaxial to single crystal texture. Even if model lacks some sophistication due to guesswork of moduli, assumptions, etc., we still clearly see an increasing trend in performance.

The piezoelectric response (intrinsic and extrinsic) in these MEMS cantilever devices showed a clear trend, increasing from fiber textured to biaxially textured to single crystal textured film microstates. Our experiments show that ferroelectric thin film device performance may be enhanced by improving the underlying grain-scale crystalline microstructure.

Chapter 5

Summary and Conclusions

This thesis work has investigated the relationship between length scales in ferroelectric thin film devices. Grain-scale film properties are analyzed with various characterization techniques and device-scale performance is studied by realizing simple ferroelectric MEMS actuators. Devices are patterned via lithography or FIB milling, as device fabrication that prioritizes CMOS compatibility paves the way for exciting materials integration opportunities. In this work, we focus on four key ferroelectric thin film microstructures: poorly oriented, fiber textured, biaxially textured, and single crystal. We find that the texture of the film not only effects intrinsic electromechanical constants but also extrinsic mechanical response via domain switching.

5.1 The Effect of Biaxial Texture on the Effective Electromechanical Constants of Polycrystalline Perovskite Materials

In Chapter 2, the electromechanical properties of barium titanate and lead titanate were investigated as a function of biaxial texture. We see that independent in-plane texturing has little effect on the piezoelectric displacement tensor. Increased out-of-plane texturing gives rise to an enhanced piezoelectric effect for barium titanate films, but not for lead titanate. Twist texturing about these out-of-plane angles shows a further enhancement in the non-shear components of the piezoelectric displacement tensor for both materials. Single crystal stiffness and dielectric constants for barium and lead titanate are similar and as such the trends in effective constants with texture are similar. Finally, we use the effective piezoelectric coupling factor as the primary figure of merit for the effective piezoelectric properties of polycrystal devices, thus utilizing all electromechanical constants of this simulation. This quantity shows a primary dependence on the out-of-plane texture.

Future work may include expanding the biaxial texture model for materials with symmetries other than 4MM, such as the common piezoelectric $Pb(Zr,Ti)O_3$ (PZT). Additionally, assumptions in the model (grain size, shape) may be altered based on experimentally determined parameters for perhaps better predictions of the electromechanical properties of polycrystalline films.

5.2 Force-Displacement Testing of Ferroelectric Thin Film MEMS Bridges

A novel fabrication technique utilizing surface micromachining is used to create MEMS bridges with $PbTiO_3$ as the active layer. By lithographically patterning devices on SiO_2/Si substrates, the application shows promise for CMOS compatibility and obviously device volume advantages. Bridge testing is performed with a custom apparatus wherein an individual device experiences an applied load via magnetostatic interaction and its displacement is recorded by a laser beam bounce and a position sensitive detector. The force-displacement data are repeatable and lend insight into the initial stress and modulus of the composite beam devices. Polycrystalline and biaxially textured bridges were characterized for texture with various grain-scale techniques. However, cracking becomes a problem in these devices.

Ongoing work might include making bridges via FIB milling as in Chapter 4. This would allow for smaller devices and they could be tested via nanoindentation, for example, to extract mechanical properties such as modulus, which obviously becomes a necessary parameter for fitting device performance and understanding the mechanical response of the piezoelectric film.

5.3 Voltage-Displacement Testing of Ferroelectric Thin Film MEMS Cantilevers

Three critical microstructures - fiber textured, biaxially textured, and single crystal textured are realized in $BaTiO_3$ MEMS cantilever devices. Layers are grown monolithically and devices are patterned on the surface via FIB milling of structures and XeF_2 etching of silicon substrates. Testing is done with voltage applied across the active layer and displacement of the cantilever is measured via inspection with optical microscopy. Macroscopic device performance is related to microscopic piezoelectric constants via multimorph calculations. The experiment shows evidence that the device performance is enhanced with enhancement in microstructure - from fiber to biaxial to single crystal texture.

Obviously many additional parameters in the beam displacement expression (such as beam length, passive layer properties, layer thicknesses) may be varied in a new study, but the most interesting phenomenon of the experiment was the extrinsic response of domain switching. This could be further examined by measuring the change in length of the cantilever during testing, perhaps in the SEM. Also, instead of $BaTiO_3$ with a predicted 1% maximum strain, $PbTiO_3$ could be used for the much larger 6% a–c switching strain. Utilizing $PbTiO_3$ would also make characterization techniques such as EBSD more quantitatively useful, as the a and c grains could be properly determined. Finally, given the FIB milling as a fabrication technique, devices could be made as small as the resolution of the SEM and therefore incorporating an exact number of ferroelectric grains into each device. Testing may have to be modified from the optical microscope measurement of deflection to perhaps a laser beam bounce measurement of deflection, such as in the AFM.

5.4 Integration of Single Crystal Ferroelectric Thin Films on Silicon via Wafer Bonding and Layer Transfer

In recent years, there has been considerable interest in layer transfer and wafer bonding processes that produce single crystal thin film layers. Light elements such as hydrogen and helium are implanted into a wafer to a specified projected range and a film of equivalent thickness is exfoliated (Tong and Gosele, 1999; Bruel, 1995). Utilizing this method in single crystal ferroelectric materials bonded to Si-based substrates creates a pathway toward high quality single crystal ferro/piezoelectric and electro-optic thin films. Such integration with Si and other device substrates has the potential to enable a new class of high work/volume piezoelectric devices for MEMS integration of ferroelectrics.

The wafer bonding process is shown schematically in Figure 5.1. The donor and receptor substrates are thoroughly cleaned. A water layer is used between the donor and receptor

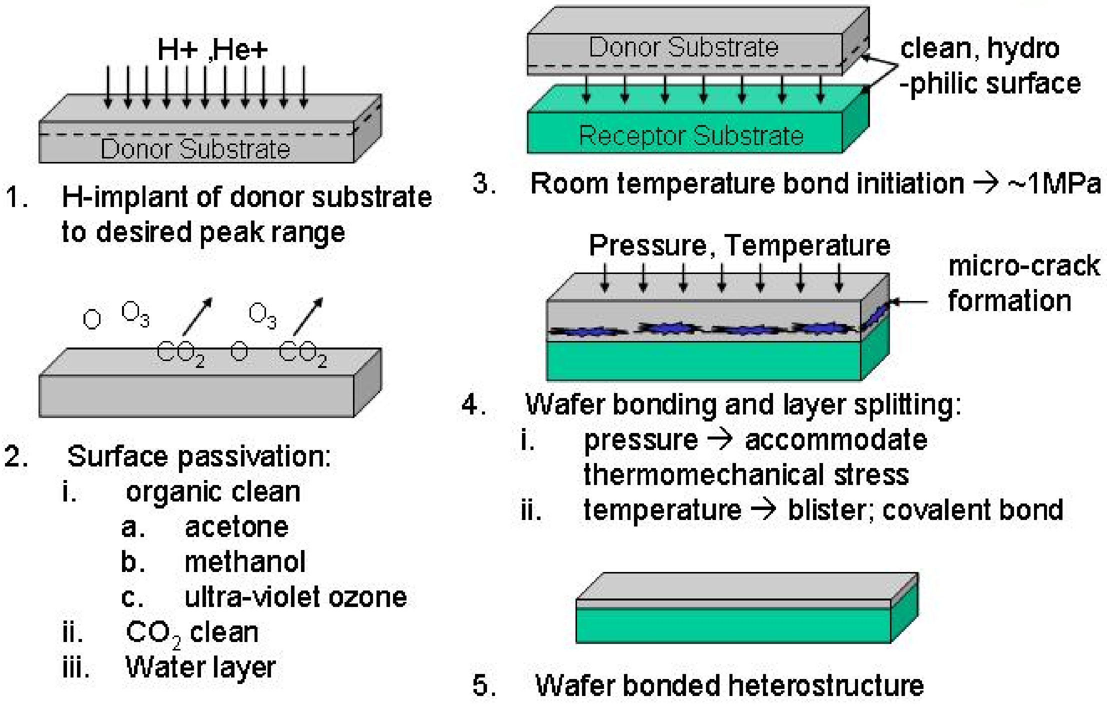

Figure 5.1: Schematic of wafer bonding process.

substrates to facilitate hydrophilic bonding. Samples are bonded at room temperature with a gentle hand pressure and then annealed for blistering and layer splitting under some pressure. The annealing step causes microcracks to form in the damaged region and subsequently cavities nucleate, coalesce, and blister. Thus the thickness of the film transferred to the receptor substrate corresponds approximately to the implantation depth in donor substrate.

Park et al. (2004) have demonstrated the wafer bonding and layer transfer technique in $BaTiO_3$. 300 nm thick $BaTiO_3$ was successfully transferred to a $Pt/Si_3N_4/Si$ substrate with a 25 mm^2 area, limited only by the size of the bulk donor crystal. Figure 5.2 shows a typical AFM topographic image and a simultaneously acquired PFM piezoresponse image of the transferred $BaTiO_3/Pt/Si_3N_4/Si$ sample, as well as an effective piezoelectric constant d_{zz} hysteresis loop (Park et al., 2004). The domain pattern and piezoelectric constant are nearly identical to that of the bulk $BaTiO_3$.

Additionally, a variety of characterization techniques have shown (Park et al., 2004; Ruglovsky et al., 2003) that the transferred thin films remain single crystal and stoichio-

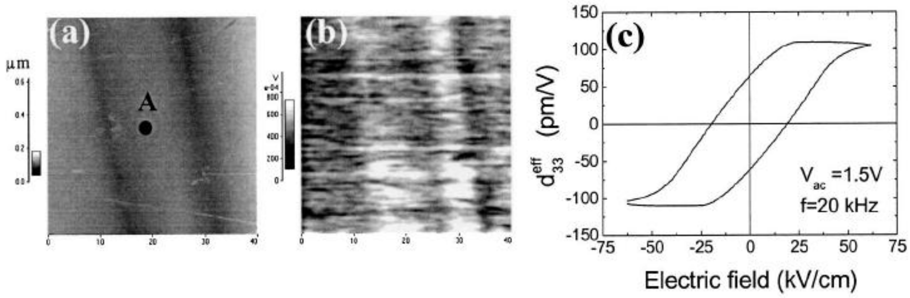

Figure 5.2: Simultaneously obtained (a) AFM topographic and (b) PFM images of the transferred $BaTiO_3$ layer on Pt-coated Si_3N_4/Si and (c) piezoelectric hysteresis curve at point A in (a).

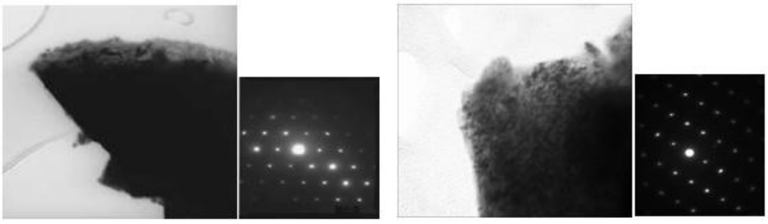
(a) (b) (c) (d)

Figure 5.3: Plan-view TEM images (a) $LiNbO_3$ and (c) $BaTiO_3$ and SAD patterns (b) $LiNbO_3$ and (d) $BaTiO_3$ for single crystal thin films after layer splitting with annealing.

metric, and that the implantation or annealing steps do not damage the film microstructure. TEM analysis, for example, has been done to investigate the microstructure of exfoliated layers of blistered $LiNbO_3$ and $BaTiO_3$ thin films, shown in Figure 5.3. Single crystal select area diffraction (SAD) patterns are evident (Ruglovsky et al., 2003).

Another useful technique is Rutherford backscattering (RBS) analysis, wherein 2 MeV He^+ ions are incident to the sample and elastically scatter from the atoms in the sample. The number of scattered ions and their energy is measured. These data provide information on the composition of the sample, the distribution of those components, and the thickness of the sample. RBS was performed on $LiNbO_3/SiO_2/Si$ bonded samples and $BaTiO_3$ bulk implanted with and without annealing. The results and simulated fit (Figure 5.4) for $LiNbO_3$ show residual Si on the surface when the analysis beam area is focused on bonded and unbonded (Si-exposed) regions. The flat niobium peak indicates that the composition

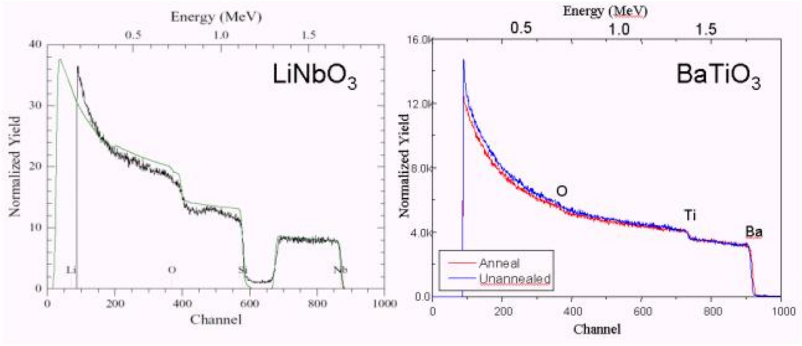

Figure 5.4: RBS spectra for transferred $LiNbO_3$ on SiO_2/Si and bulk implanted $BaTiO_3$ with and without annealing.

of the film remains uniform in depth. Simulation indicates the film is approximately 800 nm thick. The $BaTiO_3$ bulk implanted crystal shows no change upon annealing. The data indicates that even after a high-dose H^+ and He^+ implantation, the samples remains stoichiometric.

Therefore, instead of realizing polycrystalline devices with nearly single crystal texture, the wafer bonding and layer transfer technique may be utilized to fabricate ferroelectric thin films with exact stoichiometry, and domain patterns and electromechanical constants similar to bulk. If the ferroelectric transferred onto silicon substrates would be large enough in area and also on a suitably masked electrode, it would be possible to FIB out a device, utilizing FIB milling and XeF_2 silicon etch as in Chapter 4.

5.5 Final Thoughts

This thesis has discussed ferroelectric thin films of various textures and how the grain-scale properties relate to MEMS device-scale performance. Specifically, MEMS actuators were fabricated. However, another side of ferroelectric applications focuses on the intriguing optical properties of these materials. Ferroelectric $BaTiO_3$, for example, is an interesting candidate for thin film optical devices because of its large electro-optic coefficients and electrically switchable structural and optical properties. Optical quality perovskite oxide thin films grown on sufficiently thick, low optical index template layers would allow for electro-optic thin film waveguides, modulators, and statically tunable photonic devices to be designed and fabricated on silicon and silicon compatible substrates (Dicken et al., 2007). $LiNbO_3$, discussed briefly above, has been called the “silicon of nonlinear optics” and holds tremendous promise in single crystal thin film form for optoelectronic applications, with advantages such as monolithic integration, high-speed modulation, and lower operating voltages.

As with any fundamental study of materials and device physics, this research effort needs to incorporate expertise from many disciplines. The study of inherent materials properties and device performance will no doubt continue for several years and will increase in breath and depth as technology and society advances.

Appendix A: 3x6 Tensor for d with 4MM Symmetry Rotated by Euler Angles θ and ϕ

Column 1

0

$d_{31} \sin\theta$

$d_{31} \cos\theta$

Column 2

0

$\frac{1}{2} \sin\theta(d_{15} + d_{31} + d_{33} + (d_{15} + d_{31} - d_{33}) \cos 2\theta)$

$\frac{1}{2} \cos\theta(-d_{15} + d_{31} + d_{33} + (d_{15} + d_{31} - d_{33}) \cos 2\theta)$

Column 3

0

$-\frac{1}{2} \sin\theta(d_{15} - d_{31} - d_{33} + (d_{15} + d_{31} - d_{33}) \cos 2\theta)$

$\frac{1}{2} \cos\theta(d_{15} + d_{31} + d_{33} - (d_{15} + d_{31} - d_{33}) \cos 2\theta)$

Column 4

0

$\frac{1}{2} \cos\theta(-d_{31} + d_{33} + (d_{15} + d_{31} - d_{33}) \cos 2\theta)$

$-\frac{1}{2} \sin\theta(d_{31} - d_{33} + (d_{15} + d_{31} - d_{33}) \cos 2\theta)$

Column 5

$\frac{1}{2}d_{15}\cos\theta$

0

0

Column 6

$\frac{1}{2}d_{15}\sin\theta$

0

0

Appendix B: 3x6 Tensor for d with 4MM Symmetry Rotated by Euler Angles θ and ψ

Column 1

$\sin\psi\sin\theta(d_{15}+d_{31})(\cos^2\psi+\cos^2\theta\sin^2\psi)+d_{33}\sin^3\psi\sin^3\theta$

$\cos\psi\sin\theta(d_{31}\cos^2\psi+\sin^2\psi(-d_{15}+(d_{15}+d_{31})\cos^2\theta+d_{33}\sin^2\theta))$

$\cos\theta(d_{31}\cos^2\psi+\sin^2\psi(d_{31}\cos^2\theta+(-d_{15}+d_{33})\sin^2\theta))$

Column 2

$\sin\psi\sin\theta(d_{31}\sin^2\psi+\cos^2\psi(-d_{15}+(d_{15}+d_{31})\cos^2\theta+d_{33}\sin^2\theta))$

$\cos\psi\sin\theta(d_{15}+d_{31})(\cos^2\psi\cos^2\theta+\sin^2\psi)+d_{33}\cos^3\psi\sin^3\theta$

$\cos\theta(d_{31}\sin^2\psi+\cos^2\psi(d_{31}\cos^2\theta+(-d_{15}+d_{33})\sin^2\theta))$

Column 3

$\sin\psi\sin\theta((-d_{15}+d_{33})\cos^2\theta+d_{31}\sin^2\theta)$

$\cos\psi\sin\theta((-d_{15}+d_{33})\cos^2\theta+d_{31}\sin^2\theta)$

$d_{33}\cos^3\theta+(d_{15}+d_{31})\cos\theta\sin^2\theta$

Column 4

$-(d_{15}+d_{31}-d_{33})\cos\psi\cos\theta\sin\psi\sin^2\theta$

$\frac{1}{2}\cos\theta(\cos^2\psi(-d_{31}+d_{33}+(d_{15}+d_{31}-d_{33})\cos 2\theta)+d_{15}\sin^2\psi)$

$-\frac{1}{2}\cos\psi\sin\theta(d_{31}-d_{33}+(d_{15}+d_{31}-d_{33})\cos 2\theta)$

Column 5

$\frac{1}{2}\cos\theta(d_{15}\cos^2\psi+(-d_{31}+d_{33}+(d_{15}+d_{31}-d_{33})\cos 2\theta)\sin^2\psi)$

$-(d_{15}+d_{31}-d_{33})\cos\psi\cos\theta\sin\psi\sin^2\theta$

$-\frac{1}{2}\sin\psi\sin\theta(d_{31}-d_{33}+(d_{15}+d_{31}-d_{33})\cos 2\theta)$

Column 6

$\frac{1}{2}\cos\psi\sin\theta(d_{15}\cos^2\psi+(-d_{31}+d_{33}+(d_{15}+d_{31}-d_{33})\cos 2\theta\sin^2\psi))$

$\frac{1}{2}\sin\psi\sin\theta(\cos^2\psi(-d_{31}+d_{33}+(d_{15}+d_{31}-d_{33})\cos 2\theta)+d_{15}\sin^2\psi)$

$-(d_{15}+d_{31}-d_{33})\cos\psi\cos\theta\sin\psi\sin^2\theta$

Appendix C: 6x6 Tensor for C With 4MM Symmetry Rotated by Euler Angles θ and ϕ

Column 1

$$\tfrac{1}{8}(6C_{11} + C_{12} + C_{21} + 4C_{66} + (2C_{11} - C_{12} - C_{21} - 4C_{66})\cos 4\phi)$$

$$\cos^2\theta(C_{12}\cos^4\phi + 2(C_{11} - 2C_{66})\cos^2\phi\sin^2\phi + C_{21}\sin^4\phi) + C_{13}\sin^2\theta$$

$$C_{13}\cos^2\theta + (C_{12}\cos^4\phi + 2(C_{11} - 2C_{66})\cos^2\phi\sin^2\phi + C_{21}\sin^4\phi)\sin^2\theta$$

$$\cos\theta(-C_{12}\cos^4\phi + \sin^2\phi(C_{13} - C_{21}\sin^2\phi) + \cos^2\phi(C_{13} - 2(C_{11} - 2C_{66})\sin^2\phi))\sin\theta$$

$$-\tfrac{1}{4}(C_{12} - C_{21} + (-2C_{11} + C_{12} + C_{21} + 4C_{66})\cos 2\phi)\sin 2\phi\sin\theta$$

$$\tfrac{1}{4}(C_{12} - C_{21} + (-2C_{11} + C_{12} + C_{21} + 4C_{66})\cos 2\phi)\cos\theta\sin 2\phi$$

Column 2

$$\cos^2\theta(C_{21}\cos^4\phi + 2(C_{11} - 2C_{66})\cos^2\phi\sin^2\phi + C_{12}\sin^4\phi) + C_{31}\sin^2\theta$$

$$\cos^4\theta(C_{11}\cos^4\phi + (C_{12} + C_{21} + 4C_{66})\cos^2\phi\sin^2\phi + C_{11}\sin^4\phi) + (C_{13} + C_{31} + 4C_{44}) \\ \cos^2\theta\sin^2\theta + C_{33}\sin^4\theta$$

$$C_{13}\cos^4\theta + \tfrac{1}{8}(6C_{11} + C_{12} + C_{21} + 8C_{33} - 32C_{44} + 4C_{66} + (2C_{11} - C_{12} - C_{21} - 4C_{66}) \\ \cos 4\phi)\cos^2\theta\sin^2\theta + C_{31}\sin^4\theta$$

$$\cos\theta\sin\theta(-\tfrac{1}{8}(6C_{11} + C_{12} - 8C_{13} + C_{21} - 16C_{44} + 4C_{66} + (2C_{11} - C_{12} - C_{21} - 4C_{66}) \\ \cos 4\phi)\cos^2\theta + (-C_{31} + C_{33} - 2C_{44})\sin^2\theta)$$

$$\tfrac{1}{4}(-C_{12} + C_{21} + (-2C_{11} + C_{12} + C_{21} + 4C_{66})\cos 2\phi)\cos^2\theta\sin 2\phi\sin\theta$$

$$-\tfrac{1}{4}(-C_{12} + C_{21} + (-2C_{11} + C_{12} + C_{21} + 4C_{66})\cos 2\phi)\cos^3\theta\sin 2\phi$$

Column 3

$$C_{31}\cos^2\theta + (C_{21}\cos^4\phi + 2(C_{11} - 2C_{66})\cos^2\phi\sin^2\phi + C_{12}\sin^4\phi)\sin^2\theta$$

$$C_{31}\cos^4\theta + \tfrac{1}{8}(6C_{11} + C_{12} + C_{21} + 8C_{33} - 32C_{44} + 4C_{66} + (2C_{11} - C_{12} - C_{21} - 4C_{66}) \\ \cos 4\phi)\cos^2\theta\sin^2\theta + C_{13}\sin^4\theta$$

$$C_{33}\cos^4\theta + (C_{13} + C_{31} + 4C_{44})\cos^2\theta\sin^2\theta + \tfrac{1}{8}(6C_{11} + C_{12} + C_{21} + 4C_{66} + (2C_{11} - \\ C_{12} - C_{21} - 4C_{66})\cos 4\phi)\sin^4\theta$$

$$\cos\theta\sin\theta((-C_{31} + C_{33} - 2C_{44})\cos^2\theta - \tfrac{1}{8}(6C_{11} + C_{12} - 8C_{13} + C_{21} - 16C_{44} + 4C_{66} + \\ (2C_{11} - C_{12} - C_{21} - 4C_{66})\cos 4\phi)\sin^2\theta)$$

$$\tfrac{1}{4}(-C_{12} + C_{21} + (-2C_{11} + C_{12} + C_{21} + 4C_{66})\cos 2\phi)\sin 2\phi\sin^3\theta$$

$$-\tfrac{1}{4}(-C_{12} + C_{21} + (-2C_{11} + C_{12} + C_{21} + 4C_{66})\cos 2\phi)\cos\theta\sin 2\phi\sin^2\theta$$

Column 4

$$\cos\theta(-C_{21}\cos^4\phi + \sin^2\phi(C_{31} - C_{12}\sin^2\phi) + \cos^2\phi(C_{31} - 2(C_{11} - 2C_{66})\sin^2\phi))\sin\theta$$

$$\cos\theta\sin\theta(-\tfrac{1}{8}(6C_{11} + C_{12} + C_{21} - 8C_{31} - 16C_{44} + 4C_{66} + (2C_{11} - C_{12} - C_{21} - 4C_{66}) \\ \cos 4\phi)\cos^2\theta + (-C_{13} + C_{33} - 2C_{44})\sin^2\theta)$$

$$\cos\theta\sin\theta(-C_{13} + C_{33} - 2C_{44})\cos^2\theta - \tfrac{1}{8}(6C_{11} + C_{12} + C_{21} - 8C_{31} - 16C_{44} + 4C_{66} + \\ (2C_{11} - C_{12} - C_{21} - 4C_{66})\cos 4\phi)\sin^2\theta$$

$$\tfrac{1}{64}(6C_{11} + C_{12} - 8C_{13} + C_{21} - 8C_{31} + 8C_{33} + 32C_{44} + 4C_{66} - (6C_{11} + C_{12} - 8C_{13} + C_{21} - \\ 8C_{31} + 8C_{33} + 32C_{44} + 4C_{66})\cos 4\theta + 2(2C_{11} - C_{12} - C21 - 4C_{66})\cos 4\phi\sin^2 2\theta)$$

$$-\tfrac{1}{4}(-C_{12} + C_{21} + (-2C_{11} + C_{12} + C_{21} + 4C_{66})\cos 2\phi)\cos\theta\sin 2\phi\sin^2\theta$$

$$\tfrac{1}{4}(-C_{12} + C_{21} + (-2C_{11} + C_{12} + C_{21} + 4C_{66})\cos 2\phi)\cos^2\theta\sin 2\phi\sin\theta$$

Column 5

$$-\tfrac{1}{4}(-C_{12} + C_{21} + (-2C_{11} + C_{12} + C_{21} + 4C_{66})\cos 2\phi)\sin 2\phi\sin\theta$$

$$\tfrac{1}{4}(C_{12} - C_{21} + (-2C_{11} + C_{12} + C_{21} + 4C_{66})\cos 2\phi)\cos^2\theta\sin 2\phi\sin\theta$$

$$\tfrac{1}{4}(C_{12} - C_{21} + (-2C_{11} + C_{12} + C_{21} + 4C_{66})\cos 2\phi)\sin 2\phi\sin^3\theta$$

$$-\tfrac{1}{4}(C_{12} - C_{21} + (-2C_{11} + C_{12} + C_{21} + 4C_{66})\cos 2\phi)\cos\theta\sin 2\phi\sin^2\theta$$

$$C_{44}\cos^2\theta - \tfrac{1}{8}(-2C_{11} + C_{12} + C_{21} - 4C_{66} + (2C_{11} - C_{12} - C_{21} - 4C_{66})\cos 4\phi)\sin^2\theta$$

$$\tfrac{1}{16}(-2C_{11} + C_{12} + C_{21} + 8C_{44} - 4C_{66} + (2C_{11} - C_{12} - C_{21} - 4C_{66})\cos 4\phi)\sin 2\theta$$

Column 6

$$\tfrac{1}{4}(-C_{12} + C_{21} + (-2C_{11} + C_{12} + C_{21} + 4C_{66})\cos 2\phi)\cos\theta\sin 2\phi$$

$$-\tfrac{1}{4}(C_{12} - C_{21} + (-2C_{11} + C_{12} + C_{21} + 4C_{66})\cos 2\phi)\cos^3\theta\sin 2\phi$$

$$-\tfrac{1}{4}(C_{12} - C_{21} + (-2C_{11} + C_{12} + C_{21} + 4C_{66})\cos 2\phi)\cos\theta\sin 2\phi\sin^2\theta$$

$$\tfrac{1}{4}(C_{12} - C_{21} + (-2C_{11} + C_{12} + C_{21} + 4C_{66})\cos 2\phi)\cos^2\theta\sin 2\phi\sin\theta$$

$$\tfrac{1}{16}(-2C_{11} + C_{12} + C_{21} + 8C_{44} - 4C_{66} + (2C_{11} - C_{12} - C_{21} - 4C_{66})\cos 4\phi)\sin 2\theta$$

$$\cos^2\theta(C_{66}\cos^4\phi - (-2C_{11} + C_{12} + C_{21} + 2C_{66})\cos^2\phi\sin^2\phi + C_{66}\sin^4\phi) + C_{44}\sin^2\theta$$

Appendix D: 6x6 Tensor for C With 4MM Symmetry Rotated by Euler Angles θ and ψ

Column 1

$$C_{11}\cos^4\psi + \tfrac{1}{8}(C_{12} + C_{13} + C_{21} + C_{31} + 4(C_{44} + C_{66}) + (C_{12} - C_{13} + C_{21} - C_{31} - 4C_{44} + 4C_{66}) \cos 2\theta)\sin^2 2\psi + sin^4\psi(C_{11}\cos^4\theta + (C_{13} + C_{31} + 4C_{44})\cos^2\theta\sin^2\theta + C_{33}\sin^4\theta)$$

$$\cos^4\psi(C_{12}\cos^2\theta + C_{13}\sin^2\theta) + \sin^4\psi(C_{21}\cos^2\theta + C_{31}\sin^2\theta) + \cos^2\psi\sin^2\psi(C_{11} + C_{11}\cos^4\theta - 4C_{44}\sin^2\theta + C_{33}\sin^4\theta + \cos^2\theta(-4C_{66} + (C_{13} + C_{31} + 4C_{44})\sin^2\theta))$$

$$\cos^2\psi(C_{13}\cos^2\theta + C_{12}\sin^2\theta) + \sin^2\psi(C_{13}\cos^4\theta + (C_{11} + C_{33} - 4C_{44})\cos^2\theta\sin^2\theta + C_{31}\sin^4\theta)$$

$$\cos\psi\cos\theta\sin\theta((-C_{12} + C_{13})\cos^2\psi + \sin^2\psi(-2C_{44} + 2C_{66} + (-C_{11} + C_{13} + 2C_{44})\cos^2\theta + (-C_{31} + 2(C_{33} - 2C_{44})\sin^2\theta))$$

$$\cos\theta\sin\psi\sin\theta((-C_{12} + C_{13} + 2C_{44} - 2C_{66})\cos^2\psi + \sin^2\psi((-C_{11} + C_{13} + 2C_{44})\cos^2\theta + (-C_{31} + C_{33} - 2C_{44})\sin^2\theta))$$

$$\cos\psi\sin\psi(\cos^2\psi(-C_{11} + (C_{12} + 2C_{66})\cos^2\theta + (C_{13} + 2C_{44})\sin^2\theta) + \sin^2\psi(-(C_{21} + 2C_{66}) \cos^2\theta + C_{11}\cos^4\theta + \tfrac{1}{2}(C_{13} - C_{31} + C_{33} + (C_{13} + C_{31} - C_{33} + 4C_{44})\cos 2\theta)\sin^2\theta))$$

Column 2

$$\sin^4\psi(C_{12}\cos^2\theta + C_{13}\sin^2\theta) + \cos^4\psi(C_{21}\cos^2\theta + C_{31}\sin^2\theta) + \cos^2\psi\sin^2\psi(C_{11} + C_{11}\cos^4\theta - 4C_{44}\sin^2\theta + C_{33}\sin^4\theta + \cos^2\theta(-4C_{66} + (C_{13} + C_{31} + 4C_{44})\sin^2\theta))$$

$$C_{11}\sin^4\psi + \tfrac{1}{8}(C_{12} + C_{13} + C_{22} + C_{31} + 4(C_{44} + C_{66}) + (C_{12} - C_{13} + C_{21} - C_{31} - 4C_{44} + 4C_{66}) \cos 2\theta)\sin^2 2\psi + \cos^4\psi(C_{11}\cos^4\theta + (C_{13} + C_{31} + 4C_{44})\cos^2\theta\sin^2\theta + C_{33}\sin^4\theta)$$

$$\sin^2\psi(C_{13}\cos^2\theta + C_{12}\sin^2\theta) + \cos^2\psi(C_{13}\cos^4\theta + (C_{11} + C_{33} - 4C_{44})\cos^2\theta\sin^2\theta + C_{31}\sin^4\theta)$$

$$\cos\psi\cos\theta\sin\theta((-C_{12} + C_{13} + 2C_{44} - 2C_{66}\sin^2\psi + \cos^2\psi((-C_{11} + C_{13} + 2C_{44})\cos^2\theta + (-C_{31} + C_{33} - 2C_{44})\sin^2\theta))$$

$$\cos\theta\sin\psi\sin\theta((-C_{12} + C_{13})\sin^2\psi + \cos^2\psi(-2C_{44} + 2C_{66} + (-C_{11} + C_{13} + 2C_{44})\cos^2\theta + (-C_{31} + C_{33} - 2C_{44})\sin^2\theta))$$

$$\cos\psi\sin\psi(\sin^2\psi(-C_{11} + (C_{12} + 2C_{66})\cos^2\theta + (C_{13} + 2C_{44})\sin^2\theta) + \cos^2\psi(-(C_{21} + 2C_{66}) \cos^2\theta + C_{11}\cos^4\theta + \tfrac{1}{2}(C_{13} - C_{31} + C_{33} + (C_{13} + C_{31} - C_{33} + 4C_{44})\cos 2\theta)\sin^2\theta))$$

Column 3

$\cos^2\psi(C_{31}\cos^2\theta + C_{21}\sin^2\theta) + \sin^2\psi(C_{31}\cos^4\theta + (C_{11} + C_{33} - 4C_{44})\cos^2\theta\sin^2\theta + C_{13}\sin^4\theta)$

$\sin^2\psi(C_{31}\cos^2\theta + C_{21}\sin^2\theta) + \cos^2\psi(C_{31}\cos^4\theta + (C_{11} + C_{33} - 4C_{44})\cos^2\theta\sin^2\theta + C_{13}\sin^4\theta)$

$C_{33}\cos^4\theta + (C_{13} + C_{31} + 4C_{44})\cos^2\theta\sin^2\theta + C_{11}\sin^4\theta$

$\cos\psi\cos\theta\sin\theta((-C_{31} + C_{33} - 2C_{44})\cos^2\theta + (-C_{11} + C_{13} + 2C_{44})\sin^2\theta)$

$\cos\theta\sin\psi\sin\theta((-C_{31} + C_{33} - 2C_{44})\cos^2\theta + (-C_{11} + C_{13} + 2C_{44})\sin^2\theta)$

$\cos\psi\sin\psi\sin^2\theta(-C_{21} + (C_{11} - C_{31} + C_{33} - 4C_{44})\cos^2\theta + C_{13}\sin^2\theta)$

Column 4

$\cos\psi\cos\theta\sin\theta((-C_{21} + C_{31})\cos^2\psi + \sin^2\psi(-2C_{44} + 2C_{66} + (-C_{11} + C_{31} + 2C_{44})\cos^2\theta +$
$(-C_{13+C_33} - 2C_{44})\sin^2\theta))$

$\cos\psi\cos\theta\sin\theta((-C_{21} + C_{31} + 2C_{44} - 2C_{66})\sin^2\psi + \cos^2\psi((-C_{11} + C_{31} + 2C_{44})\cos^2\theta +$
$(-C_{13} + C_{33} - 2C_{44})\sin^2\theta))$

$\cos\psi\cos\theta\sin\theta(-C_{13} + C_{33} - 2C_{44})\cos^2\theta + (-C_{11} + C_{31} + 2C_{44})\sin^2\theta$

$\frac{1}{8}\cos^2\psi(C_{11} - C_{13} - C_{31} + C_{33} + 4C_{44} + (-C_{11} + C_{13} + C_{31} - C_{33} + 4C_{44})\cos 4\theta) + \sin^2\psi$
$(C_{44}\cos^2\theta + C_{66}\sin^2\theta)$

$\frac{1}{4}(C_{11} - C_{13} - C_{31} + C_{33} - 2(C_{44} + C_{66}) + (C_{11} - C_{13} - C_{31} + C_{33} - 4C_{44})\cos 2\theta)\sin 2\psi\sin^2\theta$

$\cos\theta\sin\psi\sin\theta((C_{44} - C_{66})\sin^2\psi + \cos^2\psi(C_{21} - C_{31} - C_{44} + C_{66} + (-C_{11} + C_{31} + 2C_{44})\cos^2\theta +$
$(-C_{13} + C_{33} - 2C_{44})\sin^2\theta))$

Column 5

$\cos\theta\sin\psi\sin\theta((-C_{21} + C_{31} + 2C_{44} - 2C_{66})\cos^2\psi + \sin^2\psi((-C_{11} + C_{31} + 2C_{44})\cos^2\theta +$
$(-C_{13} + C_{33} - 2C_{44})\sin^2\theta))$

$\cos\theta\sin\psi\sin\theta((-C_{21} + C_{31})\sin^2\psi + \cos^2\psi(-2C_{44} + 2C_{66} + (-C_{11} + C_{31} + 2C_{44})\cos^2\theta +$
$(-C_{13} + C_{33} - 2C_{44})\sin^2\theta))$

$\cos\theta\sin\psi\sin\theta((-C_{13} + C_{33} - 2C_{44})\cos^2\theta + (-C_{11} + C_{31} + 2C_{44})\sin^2\theta)$

$\frac{1}{4}(C_{11} - C_{13} - C_{31} + C_{33} - 2(C_{44} + C_{66}) + (C_{11} - C_{13} - C_{31} + C_{33} - 4C_{44})\cos 2\theta)\sin 2\psi\sin^2\theta$

$-\frac{1}{8}(-C_{11} + C_{13} + C_{31} - C_{33} - 4C_{44} + (C_{11} - C_{13} - C_{31} + C_{33} - 4C_{44})\cos 4\theta)\sin^2\psi + \cos^2\psi$
$(C_{44}\cos^2\theta + C_{66}\sin^2\theta)$

$\cos\psi\cos\theta\sin\theta(C_{44} - C_{66})\cos^2\psi + \sin^2\psi(C_{21} - C_{31} - C_{44} + C_{66} + (-C_{11} + C_{31} + 2C_{44}\cos^2\theta +$
$(-C_{13} + C_{33} - 2C_{44}\sin^2\theta)))$

Column 6

$$\begin{aligned}&\cos\psi\sin\psi(\cos^2\psi(-C_{11}+(C_{21}+2C_{66})\cos^2\theta+(C_{31}+2C_{44})\sin^2\theta)+\sin^2\psi(-(C_{12}+2C_{66})\\&\qquad\cos^2\theta+C_{11}\cos^4\theta+\tfrac{1}{2}(-C_{13}+C_{31}+C_{33}+(C_{13}+C_{31}-C_{33}+4C_{44})\cos 2\theta)\sin^2\theta))\end{aligned}$$

$$\begin{aligned}&\cos\psi\sin\psi(\sin^2\psi(-C_{11}+(C_{21}+2C_{66})\cos^2\theta+(C_{31}+2C_{44})\sin^2\theta)+\cos^2\psi(-(C_{12}+2C_{66})\\&\qquad\cos^2\theta+C_{11}\cos^4\theta+\tfrac{1}{2}(-C_{13}+C_{31}+C_{33}+(C_{13}+C_{31}-C_{33}+4C_{44})\cos 2\theta)\sin^2\theta))\end{aligned}$$

$$\cos\psi\sin\psi\sin^2\theta(-C_{11}+(C_{11}-C_{13}+C_{33}-4C_{44})\cos^2\theta+C_{31}\sin^2\theta)$$

$$\begin{aligned}&\cos\theta\sin\psi\sin\theta((C_{44}-C_{66})\sin^2\psi+\cos^2\psi(C_{12}-C_{13}-C_{44}+C_{66}+(-C_{11}+C_{13}+2C_{44})\\&\qquad\cos^2\theta+(-C_{31}+C_{33}-2C_{44})\sin^2\theta))\end{aligned}$$

$$\begin{aligned}&\cos\psi\cos\theta\sin\theta((C_{44}-C_{66})\cos^2\psi+\sin^2\psi(C_{12}-C_{13}-C_{44}+C_{66}+(-C_{11}+C_{13}+2C_{44})\\&\qquad\cos^2\theta+(-C_{31}+C_{33}-2C_{44})\sin^2\theta))\end{aligned}$$

$$\begin{aligned}&\tfrac{1}{32}(11C_{11}-4C_{12}-3C_{13}-4C_{21}-3C_{31}+3C_{33}-4C_{44}-8C_{66}+4(C_{11}-C_{12}+C_{13}-C_{21}+\\&\qquad C_{31}-C_{33}+2C_{44}-2C_{66}\cos 2\theta+(C_{11}-C_{13}-C_{31}+C_{33}-4C_{44})\cos 4\theta)\sin^2 2\psi+\\&\qquad\cos^4\psi(C_{66}\cos^2\theta+C_{44}\sin^2\theta)+\sin^4\psi(C_{66}\cos^2\theta+C_{44}\sin^2\theta))\end{aligned}$$

Appendix E: 3x3 Tensor for κ With 4MM Symmetry Rotated by Euler Angles θ and ϕ

Column 1

κ_{11}

0

0

Column 2

0

$\frac{1}{2}(\kappa_{11} + \kappa_{33} + (\kappa_{11} - \kappa_{33}) \cos 2\theta)$

$(-\kappa_{11} + \kappa_{33}) \cos\theta \sin\theta$

Column 3

0

$(-\kappa_{11} + \kappa_{33}) \cos\theta \sin\theta$

$\frac{1}{2}(\kappa_{11} + \kappa_{33} + (-\kappa_{11} + \kappa_{33}) \cos 2\theta)$

Appendix F: 3x3 Tensor for κ With 4MM Symmetry Rotated by Euler Angles θ and ψ

Column 1

$\kappa_{11}\cos^2\psi + \sin^2\psi(\kappa_{11}\cos^2\theta + \kappa_{33}\sin^2\theta)$

$-(\kappa_{11} - \kappa_{33})\cos\psi\sin\psi\sin^2\theta$

$(-\kappa_{11} + \kappa_{33})\cos\theta\sin\psi\sin\theta$

Column 2

$-(\kappa_{11} - \kappa_{33})\cos\psi\sin\psi\sin^2\theta$

$\kappa_{11}\sin^2\psi + \cos^2\psi(\kappa_{11}\cos^2\theta + \kappa_{33}\sin^2\theta)$

$(-\kappa_{11} + \kappa_{33})\cos\psi\cos\theta\sin\theta$

Column 3

$(-\kappa_{11} + \kappa_{33})\cos\theta\sin\psi\sin\theta$

$(-\kappa_{11} + \kappa_{33})\cos\psi\cos\theta\sin\theta$

$\kappa_{33}\cos^2\theta + \kappa_{11}\sin^2\theta$

Bibliography

Baborowski, J., 2004. Microfabrication of piezoelectric mems. Journal of Electroceramics 12, 33–51.

Berlincourt, D., Jaffe, H., 1958. Elastic and piezoelectric coefficients of single-crystal barium titanate. Physical Review B 111 (1), 143–148.

Bhattacharya, K., Ravichandran, G., 2003. Ferroelectric perovskites for electromechanical actuation. Acta Materialia 51, 5941–5960.

Brewer, R., July 2003. Quantitative biaxial texture analysis with reflection high-energy electron diffraction for ion beam-assisted deposition of mgo and heteroepitaxy of perovskite ferroelectrics. Ph.D. thesis, California Institute of Technology.

Brewer, R., Atwater, H., Groves, J., Arendt, P., 2003. Reflection high-energy electron diffraction experimental analysis of polycrystalline mgo films with grain size and orientation distributions. Journal of Applied Physics 93 (1), 205–210.

Brewer, R., Boyd, D., El-Naggar, M., Boland, S., Park, Y., Haile, S., Goodwin, D., Atwater, H., 2005. Growth of biaxially textured $Ba_xPb_{1-x}TiO_3$ ferroelectric thin films on amorphous Si_3N_4. Journal of Applied Physics 97 (3).

Bruel, M., 1995. Silicon on insulator material technology. Electronics Letters 31, 1201.

Burcsu, E., Ravichandran, G., Bhattacharya, K., 2000. Large strain electrostrictive actuation in barium titanate. Applied Physics Letters 77, 1698.

Damjanovic, D., 1998. Ferroelectric, dielectric and piezoelectric properties of ferroelectric thin films and ceramics. Reports on Progress in Physics 61, 1267–1324.

DeVoe, D., Pisano, A., 1997. Modeling and optimal design of piezoelectric cantilever microactuators. Journal of Microelectromechanical Systems 6 (3).

Dicken, M., Diest, K., Park, Y., Atwater, H., 2007. Growth and optical property characterization of textured barium titanate thin films for photonic applications. Journal of Crystal Growth (in press).

Du, X., Wang, Q., Belegundu, U., Bhalla, A., Uchino, K., 1999. Crystal orientation dependence of piezoelectric properties of single crystal barium titanate. Materials Letters 40, 109–113.

Dunn, M., Taya, M., 1993. An analysis of piezoelectric composite materials containing ellipsoidal inhomogeneities. Proceedings of the Royal Society of London A 443, 265–287.

El-Naggar, M., September 2006. Textured ferroelectric thin films: Synthesis, characterization, and influence of compositional grading on the dielectric behavior. Ph.D. thesis, California Institute of Technology.

Eom, C., Vandover, R., Phillips, J., Werder, D., Marshall, J., Chen, C., Cava, R., Fleming, R., Fork, D., 1993. Fabrication and properties of epitaxial ferroelectric heterostructures with $SrRuO_3$ isotropic metallic oxide electrodes. Applied Physics Letters 63, 2570–2572.

Fatuzzo, E., Merz, W., 1967. Ferroelectricity. North-Holland, Amsterdam, ND.

Gao, Y., Bai, G., Merkle, K., Chang, L., Lam, D., 1993. Effects of substrate orientation and cooling rate on microstructure of $PbTiO_3$ thin films grown by metal-organic chemical vapor deposition. Thin Solid Films 235, 86–95.

Harnagea, C., April 2001. Local piezoelectric response and domain structures in ferroelectric thin films investigated by voltage-modulated force microscopy. Ph.D. thesis, Martin-Luther-Universitt Halle Wittenberg.

Harnagea, C., Pignolet, A., Alexe, M., Hesse, D., 2002. Piezoresponse scanning force microscopy: What quantitative information can we really get out of piezoresponse measurements on ferroelectric thin films. Integrated Ferroelectrics 44, 113–124.

Jia, Q., Foltyn, S., Hawley, M., Wu, X., 1997. Pulsed laser deposition of conductive $SrRuO_3$ thin films. Journal of Vacuum Science Technology A 15, 1080–1083.

Jiang, J., Tian, W., Pan, X., Gan, Q., Eom, C., 1998. Effects of miscut of the $SrTiO_3$ substrate on microstructures of the epitaxial $SrRuO_3$ thin films. Materials Science and Engineering B - Solid 56, 152–157.

Jing, G., Duan, H., Sun, X., Zhang, Z., Xu, J., Li, Y., Wang, J., Yu, D., 2006. Surface effects on elastic properties of silver nanowires: Contact atomic-force microscopy. Physical Review B 73, 23409–1–6.

Jona, F., Shirane, G., 1962. Ferroelectric crystals. Per-gamon, New York, NY.

Krulevitch, P., Lee, A., Ramsey, P., Trevino, J., Hamilton, J., Northrup, M., 1996. Thin film shape memory alloy microactuators. Journal of Microelectromechanical Systems 5, 270–282.

Li, J., 2000. The effective electroelastic moduli of textured piezoelectric polycrystalline aggregates. Journal of the Mechanics and Physics of Solids 48, 529–552.

Li, J., Dunn, M., Ledbetter, H., 1999. Thermoelectroelastic moduli of textured piezoelectric polycrystals: Exact solutions and bounds for film textures. Journal of Applied Physics 86, 4626–4634.

Li, Z., Grimsditch, M., Foster, C. M., Chan, S.-K., 1996. Dielectric and elastic properties of ferroelectric materials at elevated temperature. Journal of Physics and Chemistry of Solids 57 (10), 1433–1438.

Lines, M., Glass, A., 1979. Principles and applications of ferro-electrics and related materials. Oxford University Press, Oxford, UK.

Madou, M., 1997. Fundamentals of Microfabrication. CRC Press, Boca Raton, FL.

Nye, J., 1957. Physical Properties of Crystals. Oxford University Press, Oxford, UK.

Park, J., Park, H., Kang, S., 2005. Fabrication and properties of pzt micro cantilevers using isotropic silicon dry etching process by XeF_2 gas for release process. Sensors and Actuators A 117, 1–7.

Park, Y., Ruglovsky, J., Atwater, H., 2004. Microstructure and properties of single crystal $BaTiO_3$ thin films synthesized by ion implantation-induced layer transfer. Journal of Applied Physics 85, 455–457.

Polla, D., Francis, L., 1998. Processing and characterization of piezoelectric materials and integration into microelectromechanical systems. Annual Review Materials Science 28, 563–597.

Rai-Choudhury, P., 1997. Handbook of Microlithography, Micromachining, and Microfabrication, vol. 2: Micromachining and Microfabrication. SPIE, Bellingham, WA.

Ruglovsky, J., Li, J., Bhattacharya, K., Atwater, H., 2006. The effect of biaxial texture on the effective electromechanical constants of polycrystalline barium titanate and lead titanate thin films. Acta Materialia 54, 3657–3663.

Ruglovsky, J., Park, Y., Ryan, C., Atwater, H., 2003. Wafer bonding and layer transfer for thin film ferroelectrics. Materials Research Society Symposium Proceesings 748.

Senturia, S., 2001. Microsystem design. Kluwer Publishers, Boston, MA.

Sharpe, W., 2001. Mechanical Properties of MEMs Materials, The MEMS Handbook. CRC Press, Boca Raton, FL.

Shirane, G., Hoshino, S., Suzuki, K., 1950. Crystal structures of lead titanate and of lead-barium titanate. Journal Physical Society Japan 5 (6), 453–455.

Shu, Y., 2000. Heterogeneous thin films of martensitic materials. Archive for Rational Mechanics and Analysis 153, 39–90.

Shu, Y.-C., Bhattacharya, K., 2001. Domain patterns and macroscopic behavior of ferroelectric materials. Philosophical Magazine B 81, 2021.

Spearing, S., 2000. Materials issues in microelectromechanical systems (mems). Acta Materiala 48, 179–196.

Tong, Q., Gosele, U., 1999. Semiconductor Wafer Bonding. John Wiley and Sons, New York, NY.

Uchino, K., 2000. Ferroelectric Devics. Marcel Dekker, Inc., New York, NY.

Zgonik, M., Bernasconi, P., Duelli, M., Schlesser, R., Gunter, P., Garrett, M., Rytz, D., Zhu, Y., Wu, X., 1994. Dielectric, elastic, piezoelectric, electro-optic, and elasto-optic tensors of $BaTiO_3$ crystals. Physical Review B. 50, 5941–5949.

Zhang, Q., Gross, S., Tadigadapa, S., Jackson, T., Djuth, F., Trolier-McKinstry, S., 2003. Lead zirconate titanate films for d_{33} mode cantilever actuators. Sensors and Actuators A 105, 91–97.

Zhang, R., June 2005. Mechanical characterization of thin films with application to ferroelectrics. Ph.D. thesis, California Institute of Technology.

Zhou, Y., Liu, J., Li, J., 2005. Effective electromechanical moduli of ferroelectric ceramics with fiber textures. Applied Physics Letters 86, 262909.